Multifunctional Materials for Organic and Perovskite Solar Cells

A dissertation submitted in partial fulfilment of requirements

for the degree of

Doctor of Philosophy

by

Rabindranath Garai

Roll No. 166122015

Department of Chemistry

Indian Institute of Technology Guwahati

Guwahati-781039, Assam, India

October 2021

Statement

I do hereby declare that the work incorporated in this thesis entitled, "**Multifunctional Materials for Organic and Perovskite Solar Cells**" is the result of investigations carried out by me under the guidance of Prof. Parameswar Krishnan Iyer, at the Department of Chemistry, Indian Institute of Technology Guwahati, Guwahati, Assam, India.

In keeping with the general practice of reporting scientific observations, due acknowledgements have been made wherever the work described is based on the findings of other investigators. I further declare that this work has not been submitted in part or full to any other university or institute for award of any degree or diploma.

Rabindranath Garai

IIT Guwahati — Rabindranath Garai

October 2021

Dr. Parameswar K. Iyer
Professor, Department of Chemistry and Center for Nanotechnology
Indian Institute of Technology Guwahati
Guwahati-781039, Assam, India
http://www.iitg.ac.in/chemistry/fac/pki/

Phone : +91-361-2582314
Fax : +91-361-2690762
:+91-361-2582349
E-mail : pki@iitg.ac.in

Certificate

This is to certify that the work included in this thesis entitled "**Multifunctional Materials for Organic and Perovskite Solar Cells**" by Mr. Rabindranath Garai, Department of Chemistry, Indian Institute of Technology Guwahati has been carried out under my supervision. I further certify that this work has not been submitted to any other University or Institution in part or full for the award of any degree or diploma.

IIT Guwahati
October 2021

Parameswar Krishnan Iyer
Thesis supervisor
Department of Chemistry
Indian Institute of Technology Guwahati
Guwahati – 781039, Assam, India

Dedicated to my family

Table of Contents

Acknowledgement

I am pleased to put across my heartfelt obligation and appreciation to everyone whoever have contributed in the completion of this thesis. Many individuals have supported me in this truly remarkable and amazing journey. I have tried to list everyone who have sincerely helped and guided me in the completion of this thesis. I thank each person from the bottom of my heart.

First of all, I am extremely beholden to my supervisor and mentor Prof. Parameswar Krishnan Iyer for providing me a precious opportunity to work in his group. His continuous support, valuable suggestions, scientific guidance, deep insights, and motivation have encouraged me to take up the tasks and introduced me to a field that I knew little about. I earnestly thank him for having trust in me and giving me total freedom in choosing the direction of my research. I feel fortunate to have him as my guide who has always motivated me with his hard work, dedication and optimism. He has been ever patient with me and was always available to provide his very useful opinion regarding my thesis work.

Besides my supervisor, I am highly indebted to my doctoral committee members, Prof. Mohammad Qureshi, Prof. Seenipandian Ravi, and Dr. Akshai Kumar A. S. for assessing my research work regularly. Their invaluable suggestions and crucial comments during all my seminars helped me broaden my research from various perspectives and improve my thesis.

I sincerely express my gratitude towards all my teachers especially Mr. Jayanta Kundu, Mr. Satyajit Roy, Mr. Sunil Kumar Bhunia, Mr. Ajit Kumar Jana, and all my teachers at Midnapore College as well as IIT (ISM) Dhanbad for imbibing good values and knowledge in me.

I am also thankful to all the research scholars and staff of the Department of Chemistry, IIT Guwahati for their kind cooperation and support. Further, I am grateful to Centre for Nanotechnology and Central Instrument Facility, IIT Guwahati for allowing me to access their facility for the various experimentations as and when required. I am indebted to the staff of Student Affairs, Academic Affairs and Finance sections of IIT Guwahati for being kind enough to advise and help in their respective roles. I also appreciate the efforts of Pathak Ji, Core 1 Xerox Centre, and his staff, Haloi Da and Gautam Da, for their endless help during my stay at IIT Guwahati.

I had the best of the times working with Ritesh and Adil Bhaiya who were my core solar team members. Both of them deserve the best and utmost respect for their hard work, diligence and indispensable input into the overall research work. Further, the research experience gathered along with Arvin Bhaiya, Suresh Bhaiya, Bhim Bhaiya, Ashish Bhaiya, Radha Bhaiya, Anwesha, Ramesh Bhaiya, Retwik, and Maimur Da is also worth mentioning.

I would also like to acknowledge all my other lab mates including Sameer Bhaiya, Priyanka Mam, Dip Bhaiya, Anamika Dey Di, Anamika Kalita Di, Gopi Bhaiya, Sayan Da, Rahul Bhaiya, Raman Bhaiya, Subrata Da, Nehal, Paromita, Biki, Raj, Priyam, Debika, Dibash, Tamal, Soumalya, Kavita, Mayur, Sushant, and Geetmani Da for their timely assistance and support. I also had a great learning experience with Sahu Sir, Priyanka, Amir, and Swapna while they completed their summer internship project with me. I would also like to thank each one of them for creating a pleasant and vibrant laboratory atmosphere and making my days memorable.

I was privileged to be part of the organizing team of ICANN2017 and ICANN2019 conferences. I had the opportunity to interact with the topmost scientists across the world and discuss my research work with them. I am extremely appreciative for the valuable inputs received from Prof. Han Young Woo, Korea University, Prof. Shyam Pandey, Kyushu Institute of Technology and Dr. Ankur Solanki, Pandit Deendayal Energy University.

I was also fortunate to be working in the Organic Electronics Laboratory of IIT Guwahati which houses all the sophisticated instruments. I have learnt a lot to keep these instruments in working conditions through proper maintenance. During all the maintenance activities, I have received ample support from various engineers. I would like to thank Mr. R. K. Tripathi, RVL Scientific & Engineering Pvt. Ltd., Mr. T. P. Kundu, IKA India Pvt. Ltd., and Mr. M. Nandan, Bat-Sol Equipments & Technology. They have extended all possible help as and when required. Further, I am also grateful to Dr. Prasad Gosavi and Mr. Rajkumar Somendrajit Singh, Anton Paar India Pvt. Ltd. for helping me with the GIWAX measurements in the organic solar cell work.

I extend my sincere thanks to my IIT Guwahati friends Nilanjan Da, Nirmal, Anwesha, Atanu, and Himangshu. All the discussions beyond work with all these friends helped me focus more on the research. Also, I would like to thank my friends Nilanjana, Sanjib,

Retwik, Ritesh, Tarak, Samar, Rahul, Sabyasachi, Saheb, Koushik, Papan, and Atanu from the bottom of my heart. Thank you, guys, for helping me right from the beginning of knowing each other and provide all the moral support and time.

Finally, I would like to express admiration towards my go to person, Nilanjana, who has always support me especially in the tough phases of my life. At the end, I want to thank my parents, younger brother, and my entire family for their prayers, sacrifice and struggle. It is because of them I am able to live my dream and complete my higher education from a prestigious institute. They have always given me the strength to chase my dreams which was immensely needed.

I express gratitude towards each individual for extending their support, encouragement and remembering me in their prayers.

Rabindranath Garai

[This page was intentionally left blank]

Thesis Abstract

The ever-increasing energy demand is a burning question for the modern world as the conventional energy sources are finishing exponentially. Furthermore, the depletion of fossil fuels leads to global warming and severe climate change. Therefore, it is imperative to explore cost-effective, clean, and efficient alternate energy sources. Solar energy is the most promising competitor of fossil fuels to overcome the present energy needs. Organic solar cells (OSCs) and perovskite solar cells (PSCs) have become one of the most important photovoltaic technologies in terms of efficiency. Additionally, both these solar cells offer ease of fabrication with highly abundant and low-cost materials confirming that they can be substantial contributors to commercial photovoltaic technology in the near future.

This thesis was focused on the material engineering of OSCs and PSCs. The first part of the thesis revealed the development of a new technique to synthesize materials for OSCs. The second part of the thesis demonstrated the effect of several multi-functional molecules as passivation additives for PSCs. The detailed investigation about crystallization process, grain growth of perovskite, trap states, ion migration as well as device stability was investigated thoroughly. In the first work, the microwave synthesis of a well-known conjugated polymer PTB7-Th with high molecular weight and low dispersity was performed to fabricate highly efficient OSCs. A thorough investigation of optoelectronic property and device performance was demonstrated with respect to the structure-property relationship of polymers. Highest power conversion efficiency (PCE) of 8.47 % was obtained with insignificant batch to batch variation for the microwave synthesized polymer. After that, all the other works were based on the improving device efficiency and stability of PSCs by applying suitable passivation molecules. Initially, the role of several multifunctional molecules on crystallization and grain growth of perovskite was investigate. Chelidamic acid (CA) revealed optimum trap passivation ability among all and the CA passivated film demonstrated improved film morphology and better crystallinity. As a result, a high PCE of 19.06% was attained along with enhanced thermal and long-term ambient stability. Afterward, a conjugated polyelectrolyte (PHIA) was used for perovskite passivation. A comprehensive analysis of perovskite films and devices was performed to explore the trap passivation mechanism. The expediency of this approach for large-scale commercialization was checked by fabricating large-area device. The PHIA passivated device disclosed outstanding stability in varied conditions. In the subsequent work, the effect of novel triple passivation technique was demonstrated on the perovskite passivation

as well as UV and ambient stabilization. The function of each passivation layer was studied carefully for a clear understanding. The triple passivation strategy revealed significant trap passivation leading to a high PCE of 20.46%. The triple passivated device exhibited outstanding UV and ambient stability. Finally, the fabrication of 2D-3D graded perovskite was demonstrated for improved efficiency and stability. A detailed analysis of the film morphology, trap passivation, device stability in the 2D-3D graded heterostructure was investigated meticulously. This 2D-3D graded perovskite resulted in a champion PCE of 21.18% with superior ambient stability.

The efforts demonstrated in this thesis disclose the strategy of synthesizing donor polymer for large-scale commercialization in a very quick time. It also displays various methods to acquire high-quality perovskite films with more surface coverage, large grains, fewer grain boundaries, and diminished trap states. This thesis provides significant insights into the future commercialization of OSCs and PSCs.

List of Figures

List of Tables

[This page was intentionally left blank]

CHAPTER 1

Introduction

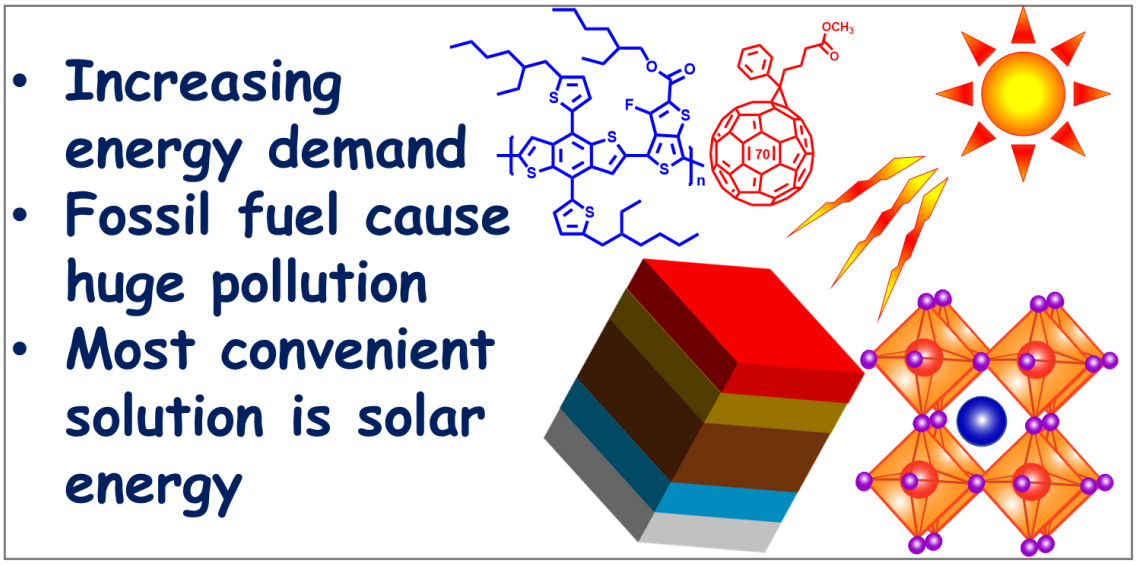

[This page was intentionally left blank]

Abstract

Modern era has witnessed an exponential increase in the global energy demand compared to the available resources resulting in huge energy crisis. Energy is required everywhere from our daily use such as cooking food, lighting, improve our living standard, etc. to power industrial equipment and in transportation. The energy demand is enhancing continuously across the globe including India due to the ever-increasing population, as well as industrial and economic growth. The energy consumption is a measure of the development for a country. Developing countries consume more energy in activities such as manufacturing, transport for the industrial and economic growth. Opportunely, a huge number of energy sources such as coal, natural gas, and fossil fuels are available in nature. But they are running out very rapidly and also leads to critical environmental problems like global warming and climate change. Considering harmful effect of these conventional energy sources, several renewable and clean energy sources, such as solar, wind, and tidal are discovered and widely studied. Among all these, solar energy is the most promising renewal energy source for future because of its enormous availability. This chapter discusses the necessity for the development of the clean and renewable technology to produce energy, particularly solar energy. The different generations of solar cells and their utilities have been briefly discussed along with some important parameters to define a solar cell. After that a comprehensive discussion on the organic and perovskite solar cells has been incorporated which includes the history, components of the devices, device architecture, working principle of the devices, and material engineering to modify device performance. Finally, the chapter concluded with a synopsis of this thesis.

1.1 Overview

The global energy demand is exponentially expanding day by day because of increasing world population, industrial & economic growth of the developing countries, and widespread use of electrical & electronics equipment and gadgets. Substantial extent of this energy requirement is achieved from easily accessible conventional energy sources i.e. the depletion of fossil fuels which are running out rapidly. Furthermore, the conventional energy sources effectively enhance carbon dioxide emission which leads to global warming and climate change.[1-3] Acknowledging the adverse ecological effect of fossil fuels, the development of cost-effective, clean, and efficient alternate energy sources has become the prime importance of present-day. There are several renewable clean energy sources such as wind, biomass, hydropower, solar, and geothermal energy. Among all these, solar technology is the most significant energy alternative because sun is the infinite source of energy to earth. It is said that if 0.1% of the earth's surface can be covered with only 10 % efficiency solar cells that can satisfy the present energy needs.[4] Hence, solar power is the most promising technology for future generations to fulfil the gradually increasing energy demands. Solar cells are generally named after the active layer semiconducting materials. Depending on the active layer materials as well as the level of commercialization of the technology, solar cells can be classified into three categories: first, second and third generation cells. The active layer materials for the first-generation solar cells are monocrystalline and polycrystalline silicon. These are also known as traditional, conventional, or wafer-based cells. Second generation solar cells are generally thin film-based cells where the active layer materials are amorphous silicon, cadmium telluride (CdTe), and copper indium gallium selenide (CIGS). Till date all the commercially available solar cell technologies are based on these two generations. However, their fabrication is very expensive and highly energy consuming. Additionally, rare and toxic materials are frequently utilized for their fabrication. Therefore, the third generations of solar cells are developed which involves low cost film fabrication technologies. The active layers of these solar cells are made of organic compounds, sometimes organometallic materials and inorganic constituents. Although most of the third-generation cells are not commercialized yet, an extensive research is taking place in all the fields. All the solar cell components of this generation are easily tuneable which facilitates a huge opportunity to improve device stability and efficiency. Third generation cells are also known as emerging photovoltaics. Some well-known third generation solar cells are dye sensitized solar cells

(DSSCs), organic solar cells (OSCs), perovskite solar cells (PSCs), quantum dot solar cell, etc. Recently OSCs and PSCs have attracted significant research interest because of certain advantages like easy fabrication, low production cost, multi-colour options, transparency, light weight, flexibility, short energy payback time, etc.[5-16] Recently, the expediency of OSCs and PSCs for space application also has been extensively investigated.[17-20] These are the two technologies most likely to be commercialized in near future due to their rapid development.

1.2 Parameters to define solar cells

1.2.1 Current density-voltage (*J*-*V*) analysis

The *J*-*V* analysis is the most important characterization for any solar cell from which PCE of the device can be computed. The *J*−*V* characteristic curves were measured by illuminating the device with AM 1.5G, 100 mW-cm^{-2} (1 sun illumination) under a solar simulator. A typical *J*−*V* curve is presented in **Figure 1.1a** and the following parameters can be estimated from that:

Short circuit current density (J_{SC})

J_{SC} is the flow of current per unit area through the external circuit at short circuited state that is when the voltage across the photovoltaic device is zero. J_{SC} is the highest current density obtained from a solar cell device (**Figure 1.1a**). Optical properties of the photovoltaic devices such as absorption of solar irradiation in the photoactive layer and reflection strongly regulates the J_{SC}.

Open circuit voltage (V_{OC})

V_{OC} is voltage obtained at open circuit state that is when there will be no current flow in the external circuit. V_{OC} is the highest voltage attained from a solar cell device (**Figure 1.1a, b**). This largely depends on the band alignment as well as the built-in potential (V_{bi}) of the photo active layer.

Fill factor (FF)

FF reveals the deviation of the actual device efficiency from the theoretically calculated value. FF is the squareness of the *J*−*V* curve can be computed from the ratio between the maximum power (P_{max}) obtained from the device and the produce of $J_{SC\ and}$ $V_{OC,}$ as shown in equation 1.1:

$$FF = \frac{P_{max}}{J_{sc}V_{oc}} = \frac{J_{mpp}V_{mpp}}{J_{sc}V_{oc}} \qquad \text{Equation 1.1}$$

P_{max} is the product of current density and voltage at maximum power point (mpp) that is the particular point of *J*–*V* characteristic where the power output is highest for the photovoltaic device (**Figure 1.1a, b**). High FF signifies better quality photovoltaic devices.

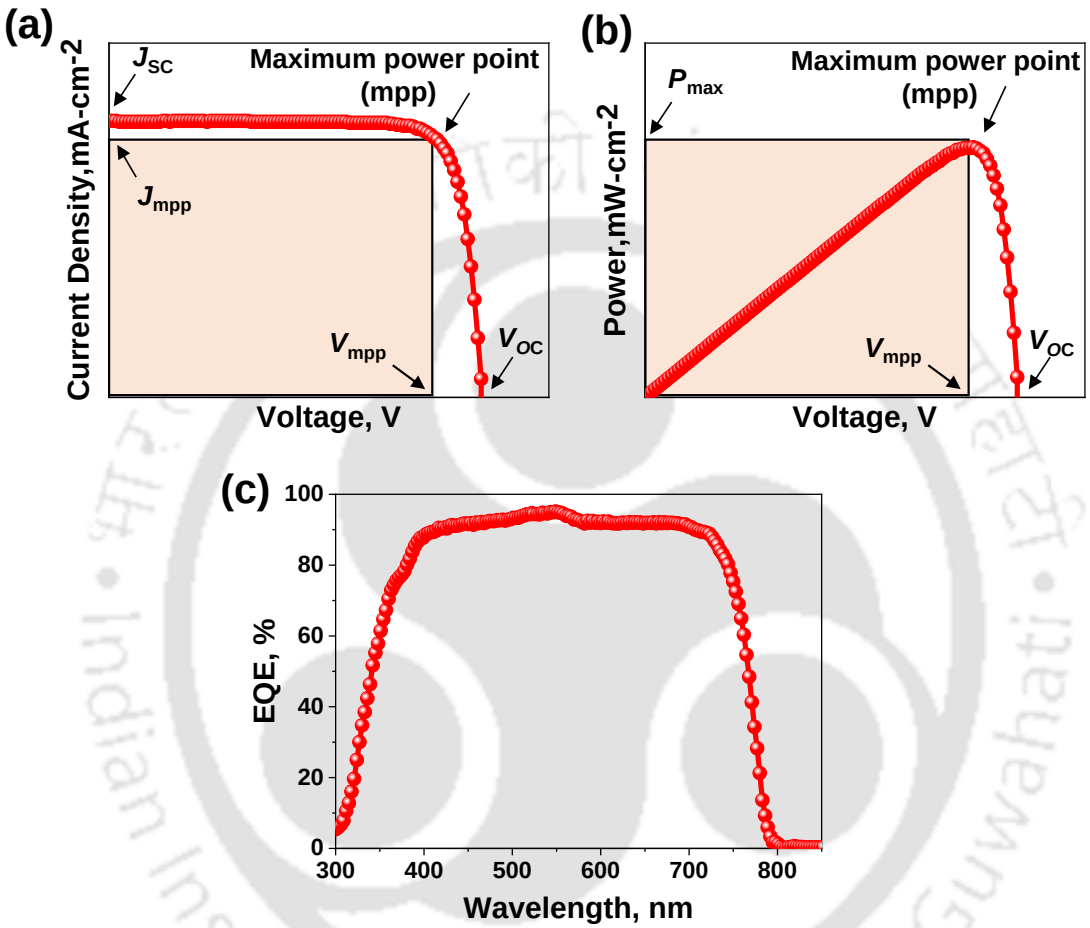

Figure 1.1 A typical example of (a) *J*-*V* plot, (b) power output versus voltage plot recorded under light illumination, and (c) A typical EQE spectrum of a perovskite solar cell.

Power conversion efficiency (PCE)

The overall PCE of any photovoltaic devices can be computed from the ratio between P_{max} and power of incident light (P_{in}), as shown in equation 1.2:

$$PCE = \frac{P_{max}}{P_{in}} = \frac{J_{sc}V_{oc}FF}{P_{in}} \qquad \text{Equation 1.2}$$

The *J*-*V* curve of solar cell strongly depends on the direction of scan (forward and reverse scan) which results in hysteresis behaviour of the devices.[21] Hysteresis index (HI) can be calculated using the following equation 1.3:

$$HI = \frac{PCE_{Forword} - PCE_{Reverse}}{PCE_{Forword}} \qquad \text{Equation 1.3}$$

1.2.2 External quantum efficiency (EQE)

EQE of any photovoltaic devices is a measure of how effectively the photogenerated charge carriers are produced from the incident photons. EQE spectrum is recorded from the response of device photocurrent upon illumination of a monochromatic light with consistently changing wavelength of the excitation light (**Figure 1.1c**). Integrated J_{SC} can also be attained from the EQE spectra which validates the results obtained from the *J-V* analysis. EQE is the ratio between the number of charge carriers extracted from a solar cell ($n_{electrons}$) and number of photons irradiated on the device (n_{photon}), as expressed in equation 1.4:

$$EQE = \frac{n_{electrone}(\lambda)}{n_{photon}(\lambda)} = \frac{J_{SC}(\lambda)/q}{P_{in}/hf} = \frac{h\nu}{q\lambda} \times \frac{J_{SC}(\lambda)}{P_{in}} = \frac{1240}{\lambda} \times \frac{J_{SC}(\lambda)}{P_{in}} \qquad \text{Equation 1.4}$$

Where, $J_{SC}(\lambda)$ is the integrated J_{SC}, q is the elementary charge, P_{in} signifies the power of illuminated light, h stands for Planck's constant, f represents light frequency under vacuum, λ is the wavelength of incident light.

1.3 History of organic and perovskite solar cells

1.3.1 Organic solar cells

The first footstep towards organic electronics was moved forward in 1977 when Alan J. Heeger, Alan MacDiarmid and Hideki Shirakawa reported high electrical conductivity in oxidized iodine-doped polyacetylene.[22] For this invention, they were awarded the 2000 Nobel Prize in Chemistry "*for the discovery and development of conductive polymers*".[23] In the year 1986, the conductive polymers were utilized as photovoltaic materials for the first time in a bi-layer device to achieve a PCE ~1%.[24] The major breakthrough in this field came when the concept of bulk heterojunction (BHJ) in solar cells was discovered where donor and acceptor materials were blended together to attain a PCE.[25] After this, BHJ OSCs have attracted incredible research attention and various novel donor as well as acceptor materials have been designed and developed over the years.[6, 26, 27] Recently, OSCs have achieved a PCE beyond 18% due to efficient molecular innovation and proper device optimization.[28]

1.3.2 Perovskite solar cells

The word "perovskite", indicates a group of materials which have similar crystal of $CaTiO_3$, named after the famous Russian mineralogist L. A. Perovski.[29] This structure can be found largely in nature in the form of $MgSiO_3$. General chemical formula of a perovskite can be written as ABX_3. These materials can be classified into two categories: first one is inorganic oxide perovskite and the second one is halide perovskite. Again, the halide perovskites can also be divided into two types: organo-metal halide perovskite and alkali halide perovskite. In case of inorganic oxide perovskite, A will be a divalent ion, such as Sr^{2+}, Mg^{2+}, Ba^{2+}, Ca^{2+}, Pb^{2+}, etc., B will be tetravalence metal ions like Si^{4+}, Ti^{4+}, Sn^{4+}, etc., X signifies O. In alkali halide perovskite, univalent alkali metals, e.g. as Na^+, Li^+, Rb^+, K^+, Cs^+, etc. will be A, and B are bivalent ions as well as X signifies halogen anions, such as I^-, Br^-, Cl^-. Organo-metal halide perovskite has quite similar composition to that of the alkali halide perovskite but the only difference is that here A will be organic cations, e.g. formamidinium (FA+), methylammonium (MA+), etc. **Figure 1.2** represents the crystal structure of perovskite materials, where B and X will produce a regular octahedron, BX_6, with B in the centre and A present in the cube-octahedral void.

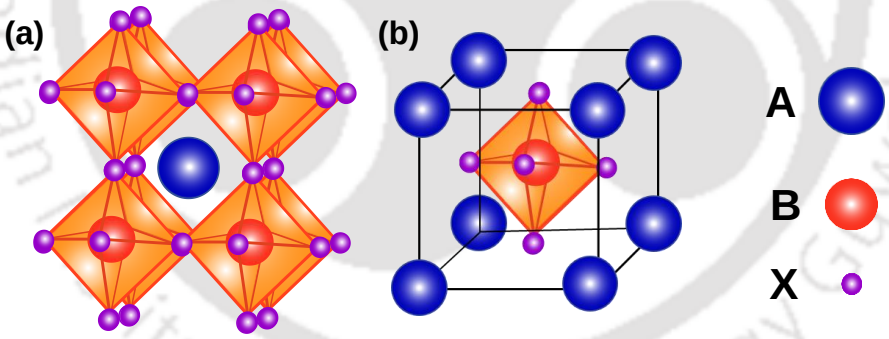

Figure 1.2 Schematic illustration of perovskite crystal unit cell (a) A-cation cantered and (b) B-cation cantered.

The structure and stability of the perovskite materials can be determined by the tolerance factor (t), which can be described by the ratio of A-X distance to the distance of B-X, as shown in following equation 1.5:[30]

$$t = \frac{(r_A + r_X)}{\sqrt{2}(r_B + r_X)} \qquad \text{Equation 1.5}$$

where r_A, r_B and r_X are the atomic radius of A, B and X respectively. The stability and the distortion of the perovskite materials can be determined by the tolerance factor. When t= 1, ideal perovskite structure usually formed with a cubic geometry. The size of the ions is

very important for the formation of this three-dimensional (3D) perovskite structures. Little disorder in the lattice can diminish the crystal symmetry. This can drastically change the photophysical and opto-electronics properties of the perovskite.

Methylammonium metal halides ($MABX_3$) were first reported in 1978 and later on in 1994 these materials were utilized in field effect devices due to their outstanding charge transport property.[31, 32] In 2009, Miyasaka and co-workers first incorporated methylammonium lead halide ($MAPbI_3$ and $MAPbBr_3$) as sensitizers in liquid DSSC.[12] But the liquid electrolytes corrode the perovskite active layer and resulted in lower PCE of only 3.81%. Later, on incorporating spiro-OMeTAD by replacing the liquid electrolytes, the device efficiency and stability were enhanced surprisingly.[33] Subsequently, an extensive research has been carried out in this field through materials as well as device engineering and the PCE crossed >25%.[34]

1.4 Components of organic and perovskite solar cells

Typical OSCs and PSCs both involve six components: transparent conducting oxide (TCO), hole transporting layer (HTL), photoactive layer, electron transporting layer (ETL), cathode Interfacial layer (CIL), and counter electrode (generally metal).

1.4.1 Transparent conducting oxide (TCO)

Commonly, photovoltaic devices are fabricated over the TCOs which can be used as a working electrode. TCOs, such as fluorene doped tin oxide (FTO), indium doped tin oxide (ITO), etc., are generally coated on a glass or plastic substrate to afford electrical conductivity. The sunlight can easily reach to the active layer by passing through the TCO coated substrate due to its transparency. In this thesis the OSCs are fabricated with ITO substrates, whereas, FTO substrates are utilized for the PSCs due to its low cost. Both the substrates have low reflection, high absorption resistance, and high transparency.

1.4.2 Hole transporting layer (HTL)

In solar cell devices HTLs are utilized for the collection of holes from the photoactive layer and its transportation to the anode. It can also act as an electron blocking layer and block the electrons from the active layer to recombine with the holes of the anode. HTLs should exhibit high charge carrier mobility (> 10^{-3} $cm^2V^{-1}s^{-1}$). For fabrication of OSCs, 3,4-

ethylenedioxythiophene): poly(styrene sulfonic) acid (PEDOT: PSS) has been used as HTL.[35] However, PEDOT: PSS has certain disadvantages, like, high sensitivity towards humidity, and can degrade the active layer due to its high acidic nature. Thus, for the fabrication of PSCs, Nickel oxide (NiO) has been utilized as HTL which is also cost effective.

1.4.3 Photoactive layer

The key component of any photovoltaic devices is the photoactive layer where charge carriers are generated through the absorption of sunlight. For the active layer of OSCs organic donor (D) and acceptor (A) materials, having well-matched band gap, are blended together. The device efficiency can be improved by fine tuning of opto-electronic properties of the blend film through molecular ae well as device engineering. Perovskite materials are used as photoactive layers for PSCs. For the enhancement of device performance, perovskite film quality can be improved through surface and bulk passivation with multifunctional additives. A comprehensive understanding about material designing and its engineering is discussed in **section 1.6**.

1.4.4 Electron transporting layer (ETL)

The key features of ETLs are the collection and transport of photo-generated electrons from the active layer to the cathode. It can also act as a hole blocking layer and block the holes from the active layer to recombine with the electrons of the cathode. In this thesis, for fabrication of OSCs, no ETL has been used whereas, for PSCs phenyl-C61-butyric acid methyl ester (PCBM) has been utilized as ETL.

1.4.5 Cathode Interfacial layer (CIL)

The CIL is used in between metal cathode and ETL or active layer which plays a critical role in improving device performance. It generally influences the work function of the cathode and enhances the electron extraction as well as facilitates better charge transport. For the OSCs fabricated in this thesis, calcium (Ca) metal is used as CIL, while for the PSCs Rhodamine 101 is applied.

1.4.6 Counter electrode

Counter electrode is the components which accomplish the internal circuit of the photovoltaic device. It is also known as back contact and used for the completion of the external circuit to allow the charge flow. Commonly, high work function metals, such as aluminium (Al), Silver (Ag), gold (Au), etc. are used as the counter electrode of solar cell devices and deposited the layer through thermal evaporation in high vacuum.

1.5 Device architecture and working principle

1.5.1 Organic solar cells

Generally, two kinds of device architecture are possible for polymer solar cells: one is conventional and the other is inverted architecture (**Figure 1.3a, b**). In conventional solar cells TCO is used as anode and metal counter electrode is used as cathode whereas, these are exactly opposite for the inverted one.

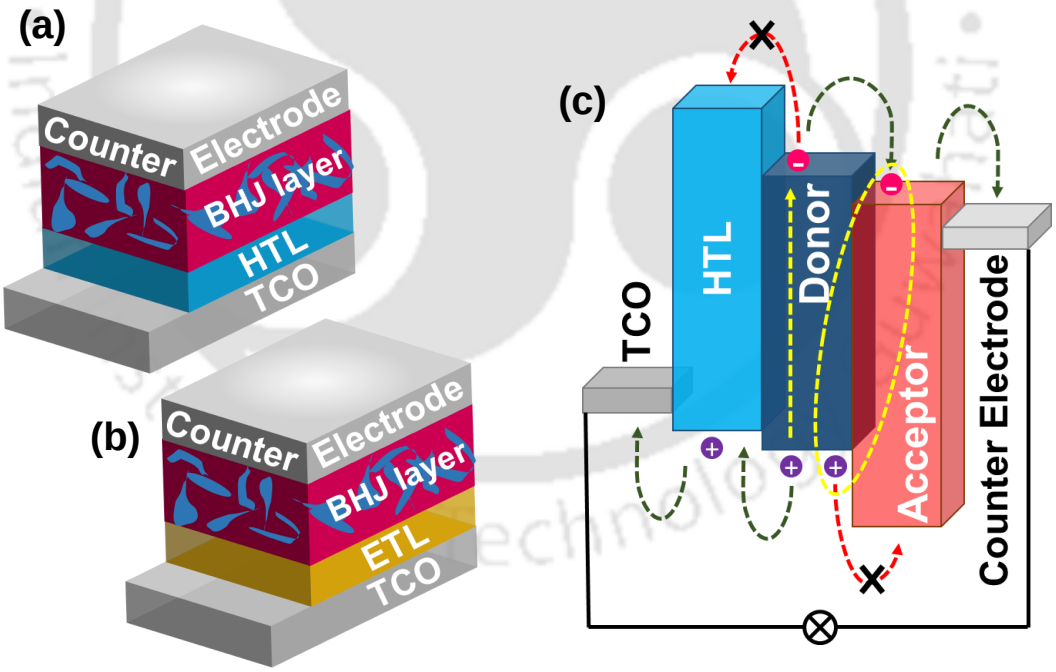

Figure 1.3 (a) conventional device architectures of organic solar cells, (b) inverted device architectures of organic solar cells, and (c) Schematic representation of working principle.

The working principle for both the architecture follows the similar charge transport mechanism (**Figure 1.3c**).[36] At first, exciton is generated in the donor upon solar energy irradiation on the photoactive layer of solar cell. Exciton is a bounded pair of hole and

electron. Then the exciton diffuses to the donor acceptor interface. After that, charge separation takes place due to suitable energy barrier between the LUMO of donor and acceptor. Finally, separated charge is transported to the respective electrodes through HTL and ETL.

1.5.2 Perovskite solar cells

The device architecture of PSCs is of two types: mesoporous and planar heterostructure (**Figure 1.4a, b, c**). In mesoporous structure a mesoporous metal oxide layer is integrated in the device.[37] However, planar configuration is developed to acquire the benefit of the ambipolar behaviour of perovskite materials. The planar device can also be of two kinds: regular (n-i-p) planar and inverted (p-i-n) planar.[38, 39] This classification is carried out by considering the respective contacts (n-type or p-type) utilized towards TCO.

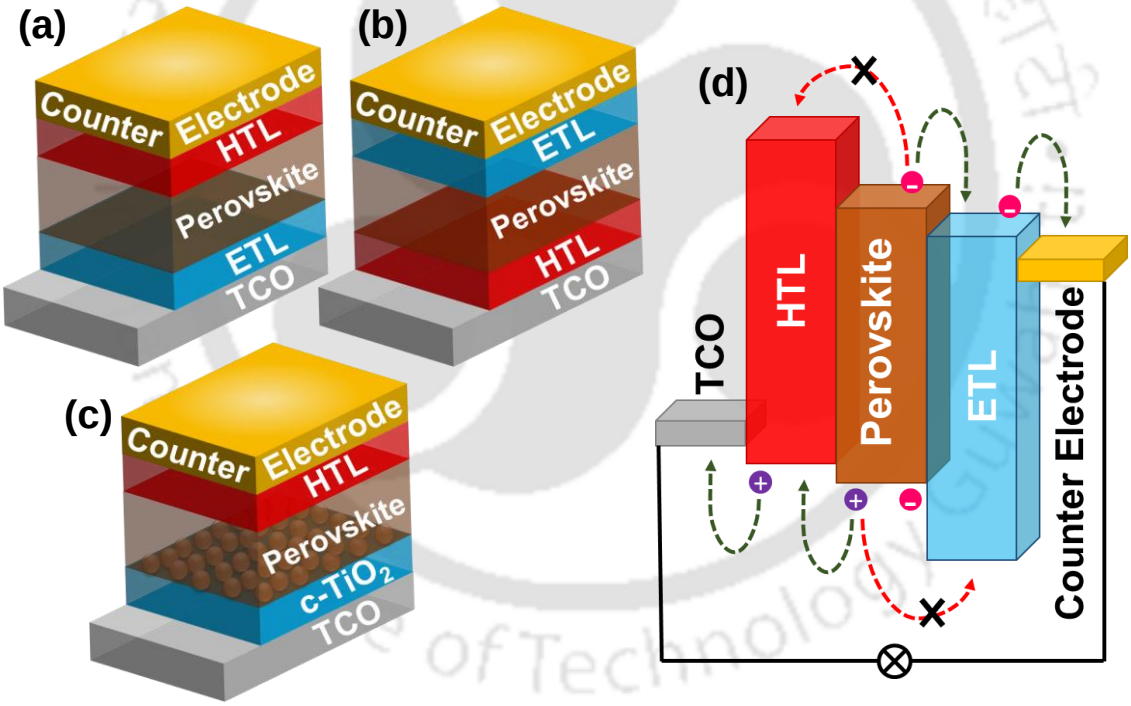

Figure 1.4 Device architectures of perovskite solar cells (a) planar (n–i–p) and (b) planar (p–i–n), (c) mesoporous (n-i-p). (d) Schematic representation of working principle.

The working mechanism of mesoporous as well as planar PSCs follow similar charge transport pathway like the OSCs (**Figure 1.4d**) though, there is a conflict among the scientists regarding the exciton formation in PSCs. When sunlight falls upon perovskite, holes and electrons are produced firstly due to photoexcitation of the active layer. Then the photogenerated holes will be injected into the HOMO level or valance band of the HTL as

well as the electrons will be transported to the LUMO level or conduction band of the ETL. Finally, these charges are transferred to the respective electrodes. However, considerable carrier recombination occurs at the grain boundaries of perovskite as well as at the interface of HTL and ETL. Thus, more efficient interfacial contacts and larger grains are needed for mitigated charge carrier recombination.

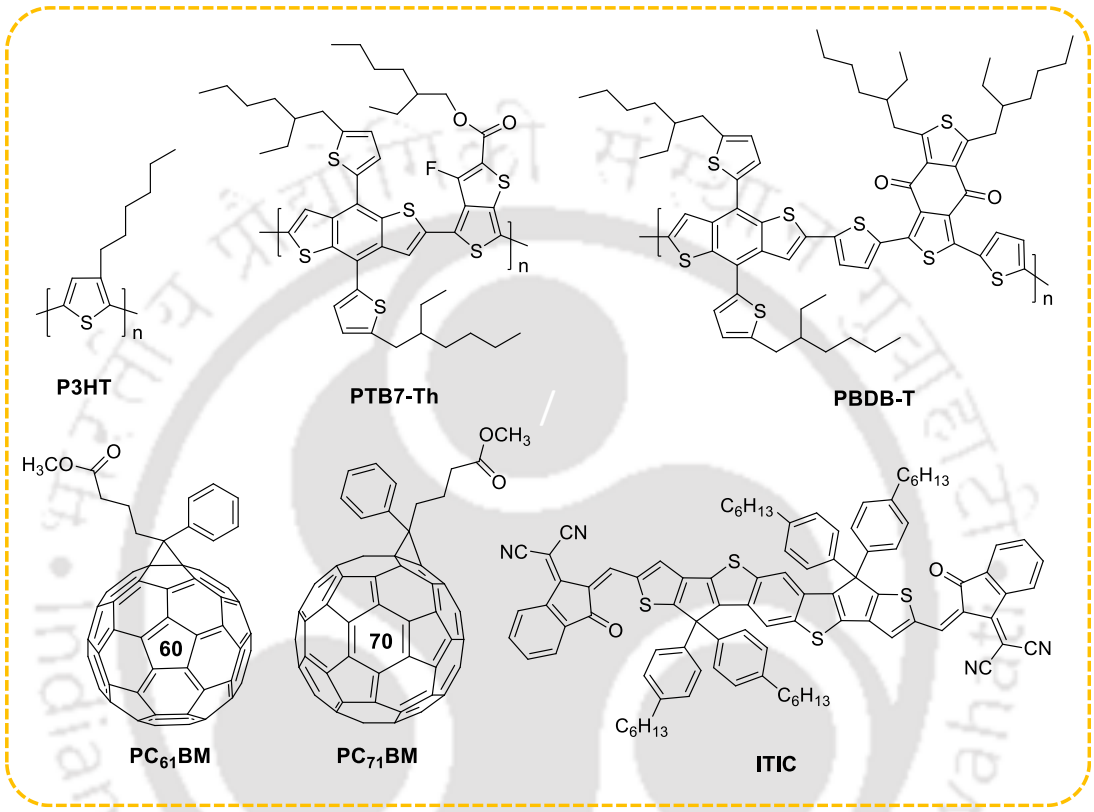

Figure 1.5 Chemical structures of some well-known donor and acceptor materials.

1.6 Engineering of organic and perovskite solar cells

1.6.1 Organic solar cells

BHJ OSCs consist of donor and acceptor materials of well-matched bandgap and complementary absorption. Generally, donor materials such as P3HT, PTB7-Th, PBDB-T, etc. are blended together with the fullerene ($PC_{61}BM$ and $PC_{71}BM$) and non-fullerene acceptors (ITIC, IDIC, etc.) for the active layer of BHJ devices. **Figure 1.5** reveals the chemical structures of some well-known donor and acceptors materials utilized in BJH OSCs. Several molecular and device engineering strategies have been applied to enhance the device efficiency and stability. The molecular weight (Mw) and polydispersity index (Đ) of the donor polymer typically regulates the molecular orientation as well as

optoelectronic properties, crystallinity, film morphology, hole mobility, and device performance.[40-46] Commonly, polymers with higher molecular weights give better device performance because of superior film morphology and better carrier mobility.[40, 41, 47] However, polymers with very high molecular weight exhibit solubility issue and demonstrate poor intermixed morphology as well as reduced device performance. Furthermore, when the Đ values of the polymer enhances it results in lower device results.[48] Thus, polymers with optimal Mw and lower Đ is required for improved device performances.

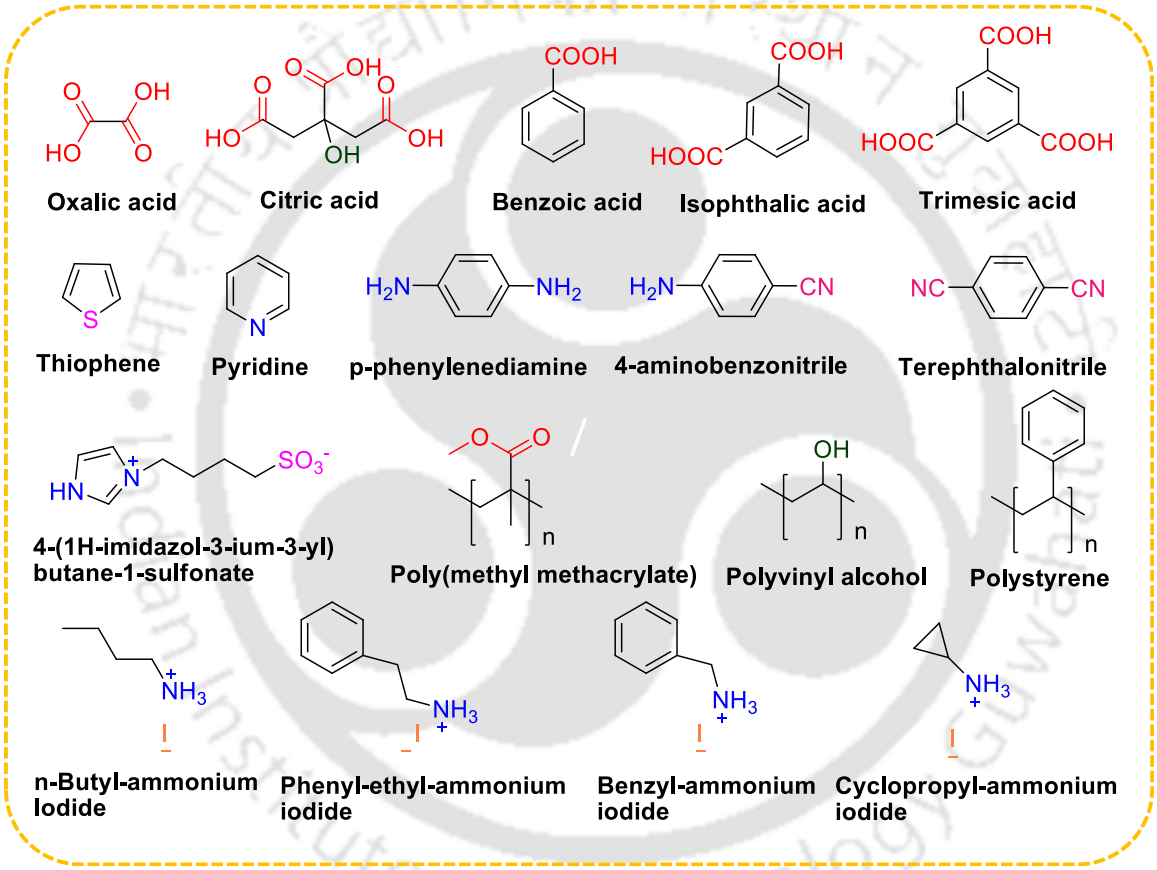

Figure 1.6 Chemical structures of some well-known passivation molecules.

1.6.2 Perovskite solar cells

PSCs have demonstrated a record PCE improvement within a very rapid time due to excellent optoelectronic properties of the perovskite materials such as band gap tunability, higher absorption coefficient, ambient semiconductor, improved charge carrier lifetime, etc.[12, 13, 49] Inspite of such remarkable optoelectronic properties and high PCEs, PSCs suffers from substantial instability under ultraviolet (UV) irradiation and humid condition which limits its practical application.[50-55] This instability mainly originates from the trap

states present in perovskite films. To attain improved stability, superior quality perovskite films are required with lower trap states and high crystallinity. Several strategies have been established to acquire improved perovskite films such as composition engineering, anti-solvent treatment, solvent engineering, thermal or solvent annealing, vapor-assisted solution deposition, vacuum flash treatment, and hot-casting of substrate.[56-68]

However, the crystallization process of perovskite is very inconsistent and often results in poor film morphology in terms of film coverage, grain size, crystallinity, and trap states.[69-71] Such films display significant defects (e.g., non-coordinated and under coordinated ions mainly generated because of ion migration) at surface and grain boundaries which can act as recombination centres and decreases the carrier life time as well as the device performances. At the same time, corrosive moisture and oxygen in atmosphere can simply interact with these defect states and damage the perovskite.[72, 73] The most expedient technique to effectively passivate these defect states is to utilize multifunctional chemical additives with varied anchoring groups (e.g., -COOH, –OH,–NH_2, –CN, etc.).[74, 75] These multifunctional molecules are generally added into the perovskite precursor solution or a separate layer has been coated over the perovskite for passivation. When these molecules are added in the precursor solution, the functional groups not only interact with traps but also can participate in the nucleation of perovskite and regulate the grain growth. These additives restrict the moisture penetration into the perovskite and enhance the device stability.

Multifunctional additives can reduce the trap states through varied interactions such as, Lewis acid-base interactions, hydrogen bonding, etc. For example, oxalic acid, citric acid, benzoic acid, and several other carboxylic acids were utilized to regulate the grain growth of perovskite.[76-78] These molecules tightly bound with the under coordinated lead ions through Lewis acid-base interaction to passivate the defects that results in improved device efficiency as well as stability. Further, electron rich molecules such as thiophene, pyridine, and several π-conjugated small molecules provide electron density to various positively charged defects to minimize charge carrier recombination.[79-84] Again, some Lewis base kind of defects of perovskite can be annihilated with the acceptor molecules such as $PC_{61}BM$, ITIC, IDIC, etc.[85, 86] The defect states of perovskite can also be effectively reduced with the ionic small molecule and ionic liquids such as 1,3-dimethyl-3-imidazolium hexafluorophosphate, 4-(1H-imidazol-3-ium-3-yl)butane-1-sulfonate.[87, 88] All these passivation strategies not only enhance the device efficiency but also considerably

improves the device stability. In contrast to small molecular additives, polymers can significantly enhance the hydrophobicity of the perovskite layer. Additionally, polymers exhibit a benefit of preferential orientation along the grain boundaries of perovskite because of their larger size whereas the small molecules may be combined with the perovskite lattice.[89] Several conjugated and non-conjugated polymers such as PTB7-Th, PBDB-T, PVA, PMMA, PS, etc. have been utilized as passivating agents for perovskite.[90] Recently, polyelectrolytes are also being used for the passivation of perovskite.[91] Another well-known approach to enhance the device stability is to incorporate a layer of organic ammonium halide salt which leads to formation of thin two-dimensional (2D) perovskite over the three-dimensional (3D) structure. Currently, this 2D-3D graded heterostructures have received incredible research attention as it integrates the benefits of high light absorption and enhanced charge transport of 3D perovskite with the augmented stability of 2D capped perovskite. Along with the stability improvement, the capping layer also passivates the defect states and heals the halide vacancies. To study the effect of 2D-3D graded heterostructures on the device efficiency and stability several ammonium halide salt, such as n- butylammonium iodide, iso-butylammonium iodide, phenyl-ethyl-ammoniumiodide, benzyl-ammoniumiodide, and cyclopropyl-ammonium iodide have been investigated.[92-94] The chemical structures of some well-known passivation molecules are presented in **Figure 1.6**. A proper optimization of the passivation molecules can be an effective strategy to fabricate highly efficient and stable devices for future commercialization.

1.7 Thesis Synopsis

Considering the severe climate change and energy crisis, the motivation of this thesis is to attain sustainable and clean energy generation through the development of organic and perovskite solar cells for improved device performance and stability. The first part, comparatively a smaller portion, of the thesis deals with the development of a new technique to synthesize materials for organic solar cells. The second part, relatively a larger portion, is based on the effect of several multi-functional molecules as passivation additives for perovskite solar cells. The detailed investigation about crystallization process, grain growth of perovskite, trap states, ion migration as well as device stability have been performed. The results achieved throughout these investigations are independently

composed into five chapters. Lastly, a summary and future prospect is presented. A brief outline of all these chapters is given below

Chapter 2 aims to the synthesize of a well-known conjugated polymer PTB7-Th with low dispersity and high molecular weight. The large-scale commercial synthesis of conjugated polymers for BHJ OSCs is very challenging as well as energy and time consuming. For the improved reproducibility of the OSC devices, a convenient synthetic technique is required to obtain high quality conjugated polymers with less batch to batch variation in polydispersity index and molecular weight. Organic reactions in closed microwave reactor is known to be more meticulous and consumes lesser energy. Here, the polymerization method has been optimized in a closed microwave reactor by varying the reaction time to achieve optimal polydispersity index and molecular weight. The effect of polymer molecular weight on the conventional OSC devices with $PC_{71}BM$ acceptor was investigated to derive a systematic structure-property relationship. The results obtained from the microwave synthesized polymer were also compared with the polymer synthesized via conventional thermal route where the newer method outperform the old one with a comparable PCE and lesser batch to batch variation. Thus, this study has revealed that the closed microwave reaction protocol can be very beneficial in quick, energy efficient and large-scale synthesis of conjugated polymers for OSCs.

Chapter 3 deals with the effect of multifunctional molecules on the crystallization, grain growth, and trap passivation of perovskite. Three different multifunctional additives namely 5-aminoisophthalic acid (AIA), 5-hydroxyisophthalic acid (HIA) and chelidamic acid (CA) have been strategically chosen. CA molecule, with its higher dipolar electron density distribution, displays better passivation capacity among all. In comparison to the pristine, the passivated films illustrated better morphology with larger grains and lesser pin holes. CA passivated device revealed a high PCE of 19.06% over the pristine device of 13.60%. Moreover, the passivated device discloses outstanding ambient and thermal stability as compared to the pristine one because of lesser trap states and minimized ion migration. Therefore, this approach, to use multifunctional molecules for regulating crystallization and reducing defect states, will extend the knowledge of selecting chemical additives to for perovskite passivation.

Chapter 4 demonstrates about the trap passivation of perovskite with a conjugated polyelectrolyte, PHIA, through comprehensive film and device analysis. The PHIA polymer effectively reduces the defect states of perovskite and results in mitigated carrier

recombination, improved charge transport, and very low accumulation of charges at the interface. Consequently, PHIA modified device reveals a high PCE of 20.17% with lower hysteresis. Moreover, PHIA passivation improves the long-term device stability by enhancing the hydrophobicity of the perovskite layer. The passivated also reveals improved thermal and photo-stability. Furthermore, large area device has also been fabricated to validate the practicality of this method for future commercialization. Therefore, this facile trap passivation strategy provides significant insight in the direction of fabricating efficient and stable PSCs for future commercialization.

Chapter 5 describes about an advanced triple passivation technique utilizing 2-benzoylpyridine (BP) as a passivation molecule to laminate perovskite for the stabilization of PSCs. Double layers of BP were coated above and below the perovskite layer, and the molecule was also incorporated in the precursor solution. The layers on either side of perovskite provide UV as well as moisture resistance, and the one in precursor solution passivates the trap states in bulk. This strategy significantly improves the perovskite crystallinity and film quality, provides lower recombination and better carrier transport in the device. The triple passivated device exhibits a high PCE of 20.46% with almost negligible hysteresis. Additionally, triple passivated large-area device has been fabricated that demonstrates a PCE of 18.61%. Moreover, the triple passivation approach discloses impressive UV and ambient stability because it can effectively shield the perovskite layer from UV illumination and moisture. Thus, this approach provides an efficient strategy for concurrent enhancement of UV and ambient stability of PSCs as well as a facile route towards commercial fabrication in large-scale.

Chapter 6 focuses to simultaneously improve perovskite film morphology and stability. Organic ammonium halide salts are broadly applied for surface passivation as a corresponding 2D top layer over a 3D perovskite film. This 2D-3D graded heterostructure reveals high quality film with lower trap states and the top 2D layer increases film stability by significantly improving the hydrophobicity of the layer. In this work, 4-(aminomethyl)benzoic acid hydrogen bromide (ABHB) has been utilized for surface passivation of perovskite to fabricate 2D-3D perovskite. Carboxylic acid functionalization can effectively improve the passivation capability and bromide ion can fill the halide vacancies in the perovskite lattice. Consequently, ABHB treated device exhibits a high efficiency of 21.18%. The modified device reveals substantially lower hysteresis because of minimized ion migration. Furthermore, the ambient stability of the modified device

considerably improves as compared to the pristine device. This work provides very useful insights into the passivation group incorporation as well as halide engineering effect of organic ammonium halide salt forming a 2D-3D graded perovskite.

Chapter 7 discusses conclusions and future prospects of the thesis. A brief summary of the all the research works is presented along with the future road map towards commercialization of perovskite solar cells.

References

1. M. Hoel and S. Kverndokk, *Resour Energy Econ.*, 1996, **18**, 115-136.
2. N. Armaroli and V. Balzani, *Angew. Chem., Int. Ed.*, 2007, **46**, 52-66.
3. L. Chiari and A. Zecca, *Energy Policy*, 2011, **39**, 5026-5034.
4. M. Grätzel, *Nature*, 2001, **414**, 338-344.
5. A. J. Heeger, *Adv. Mater.*, 2014, **26**, 10-28.
6. L. Lu, T. Zheng, Q. Wu, A. M. Schneider, D. Zhao and L. Yu, *Chem. Rev.*, 2015, **115**, 12666-12731.
7. F. C. Krebs, S. A. Gevorgyan and J. Alstrup, *J. Mater. Chem.*, 2009, **19**, 5442-5451.
8. Y. Li, *Acc. Chem. Res.*, 2012, **45**, 723-733.
9. H. Kang, G. Kim, J. Kim, S. Kwon, H. Kim and K. Lee, *Adv. Mater.*, 2016, **28**, 7821-7861.
10. A. Polman, M. Knight, E. C. Garnett, B. Ehrler and W. C. Sinke, *Science*, 2016, **352**, aad4424.
11. C.-C. Chen, L. Dou, R. Zhu, C.-H. Chung, T.-B. Song, Y. B. Zheng, S. Hawks, G. Li, P. S. Weiss and Y. Yang, *ACS Nano*, 2012, **6**, 7185-7190.
12. A. Kojima, K. Teshima, Y. Shirai and T. Miyasaka, *J. Am. Chem. Soc.*, 2009, **131**, 6050-6051.
13. S. D. Stranks, G. E. Eperon, G. Grancini, C. Menelaou, M. J. P. Alcocer, T. Leijtens, L. M. Herz, A. Petrozza and H. J. Snaith, *Science*, 2013, **342**, 341-344.
14. J. Zhang, W. Zhang, H.-M. Cheng and S. R. P. Silva, *Mater. Today*, 2020, **39**, 66-88.
15. J. Chung, S. S. Shin, K. Hwang, G. Kim, K. W. Kim, D. S. Lee, W. Kim, B. S. Ma, Y.-K. Kim, T.-S. Kim and J. Seo, *Energy Environ. Sci.*, 2020, **13**, 4854-4861.
16. N. Li, X. Niu, Q. Chen and H. Zhou, *Chem. Soc. Rev.*, 2020, **49**, 8235-8286.
17. Y. Tu, J. Wu, G. Xu, X. Yang, R. Cai, Q. Gong, R. Zhu and W. Huang, *Adv. Mater.*, 2021, **33**, 2006545.
18. I. Cardinaletti, T. Vangerven, S. Nagels, R. Cornelissen, D. Schreurs, J. Hruby, J. Vodnik, D. Devisscher, J. Kesters, J. D'Haen, A. Franquet, V. Spampinato, T. Conard, W. Maes, W. Deferme and J. V. Manca, *Sol. Energy Mater. Sol. Cells.*, 2018, **182**, 121-127.
19. L. K. Reb, M. Böhmer, B. Predeschly, S. Grott, C. L. Weindl, G. I. Ivandekic, R. Guo, C. Dreißigacker, R. Gernhäuser, A. Meyer and P. Müller-Buschbaum, *Joule*, 2020, **4**, 1880-1892.
20. J. Yang, Q. Bao, L. Shen and L. Ding, *Nano Energy*, 2020, **76**, 105019.

21. E. L. Unger, E. T. Hoke, C. D. Bailie, W. H. Nguyen, A. R. Bowring, T. Heumüller, M. G. Christoforo and M. D. McGehee, *Energy Environ. Sci.*, 2014, **7**, 3690-3698.
22. H. Shirakawa, E. J. Louis, A. G. MacDiarmid, C. K. Chiang and A. J. Heeger, *J. Chem. Soc., Chem. Commun.*, 1977, DOI: 10.1039/C39770000578, 578-580.
23. A. Heeger, A. MacDiarmid and H. Shirakawa, The Nobel Prize in Chemistry 2000, https://www.nobelprize.org/prizes/chemistry/2000/summary/, 2000).
24. C. W. Tang, *Appl. Phys. Lett.*, 1986, **48**, 183-185.
25. G. Yu, J. Gao, J. C. Hummelen, F. Wudl and A. J. Heeger, *Science*, 1995, **270**, 1789.
26. L. Hong, H. Yao, Y. Cui, Z. Ge and J. Hou, *APL Materials*, 2020, **8**, 120901.
27. A. a. F. Eftaiha, J.-P. Sun, I. G. Hill and G. C. Welch, *J. Mater. Chem. A*, 2014, **2**, 1201-1213.
28. Q. Liu, Y. Jiang, K. Jin, J. Qin, J. Xu, W. Li, J. Xiong, J. Liu, Z. Xiao, K. Sun, S. Yang, X. Zhang and L. Ding, *Sci. Bull.*, 2020, **65**, 272-275.
29. Perovskite. Webmineral, http://webmineral.com/data/Perovskite.shtml#.YOApsugzbIV).
30. M. A. Peña and J. L. G. Fierro, *Chem. Rev.*, 2001, **101**, 1981-2018.
31. D. Weber, *Zeitschrift für Naturforschung B*, 1978, **33**, 1443-1445.
32. D. B. Mitzi, C. A. Feild, W. T. A. Harrison and A. M. Guloy, *Nature*, 1994, **369**, 467-469.
33. H.-S. Kim, C.-R. Lee, J.-H. Im, K.-B. Lee, T. Moehl, A. Marchioro, S.-J. Moon, R. Humphry-Baker, J.-H. Yum, J. E. Moser, M. Grätzel and N.-G. Park, *Sci. Rep.*, 2012, **2**, 591.
34. National Renewable Energy Laboratory, Best research-cell efficiencies chart, https://www.nrel.gov/pv/assets/pdfs/best-research-cell-efficiencies.20191106.pdf, (accessed 28.06.2021).
35. Z. H. Bakr, Q. Wali, A. Fakharuddin, L. Schmidt-Mende, T. M. Brown and R. Jose, *Nano Energy*, 2017, **34**, 271-305.
36. H. Yao, L. Ye, H. Zhang, S. Li, S. Zhang and J. Hou, *Chem. Rev.*, 2016, **116**, 7397-7457.
37. M. M. Lee, J. Teuscher, T. Miyasaka, T. N. Murakami and H. J. Snaith, *Science*, 2012, **338**, 643.
38. M. Liu, M. B. Johnston and H. J. Snaith, *Nature*, 2013, **501**, 395-398.
39. J.-Y. Jeng, Y.-F. Chiang, M.-H. Lee, S.-R. Peng, T.-F. Guo, P. Chen and T.-C. Wen, *Adv. Mater.*, 2013, **25**, 3727-3732.

40. S. F. Hoefler, T. Rath, N. Pastukhova, E. Pavlica, D. Scheunemann, S. Wilken, B. Kunert, R. Resel, M. Hobisch, S. Xiao, G. Bratina and G. Trimmel, *J. Mater. Chem. A*, 2018, **6**, 9506-9516.

41. C. Liu, K. Wang, X. Hu, Y. Yang, C.-H. Hsu, W. Zhang, S. Xiao, X. Gong and Y. Cao, *ACS Appl. Mater. Interfaces*, 2013, **5**, 12163-12167.

42. Z. Li, D. Yang, X. Zhao, T. Zhang, J. Zhang and X. Yang, *Adv. Funct. Mater.*, 2018, **28**, 1705257.

43. Y. Zhang, X. Xu, J. Lu and S. Zhang, *RSC Adv.*, 2019, **9**, 14657-14661.

44. W. Li, L. Yang, J. R. Tumbleston, L. Yan, H. Ade and W. You, *Adv. Mater.*, 2014, **26**, 4456-4462.

45. I. Osaka, M. Saito, H. Mori, T. Koganezawa and K. Takimiya, *Adv. Mater.*, 2012, **24**, 425-430.

46. N. P. Holmes, S. Ulum, P. Sista, K. B. Burke, M. G. Wilson, M. C. Stefan, X. Zhou, P. C. Dastoor and W. J. Belcher, *Sol. Energy Mater. Sol. Cells.*, 2014, **128**, 369-377.

47. H. Kang, M. A. Uddin, C. Lee, K.-H. Kim, T. L. Nguyen, W. Lee, Y. Li, C. Wang, H. Y. Woo and B. J. Kim, *J. Am. Chem. Soc.*, 2015, **137**, 2359-2365.

48. L. Lu, T. Zheng, T. Xu, D. Zhao and L. Yu, *Chem. Mater.*, 2015, **27**, 537-543.

49. C. C. Boyd, R. Cheacharoen, T. Leijtens and M. D. McGehee, *Chem. Rev.*, 2019, **119**, 3418-3451.

50. M. Li, H. Li, J. Fu, T. Liang and W. Ma, *J. Phys. Chem. C*, 2020, **124**, 27251-27266.

51. L. Meng, J. You and Y. Yang, *Nat. Commun.*, 2018, **9**, 5265.

52. Q. Wali, F. J. Iftikhar, M. E. Khan, A. Ullah, Y. Iqbal and R. Jose, *Org. Electron.*, 2020, **78**, 105590.

53. G. Niu, X. Guo and L. Wang, *J. Mater. Chem. A*, 2015, **3**, 8970-8980.

54. Z. Yuxiong, H. Jinghua, W. Yuxia, Q. Rongbang, Z. Chengming, X. Xiaoying and J. Minlin, *J. Photonics Energy*, 2019, **9**, 1-20.

55. H.-S. Kim, J.-Y. Seo and N.-G. Park, *ChemSusChem*, 2016, **9**, 2528-2540.

56. N. J. Jeon, J. H. Noh, W. S. Yang, Y. C. Kim, S. Ryu, J. Seo and S. I. Seok, *Nature*, 2015, **517**, 476-480.

57. I. Kopacic, B. Friesenbichler, S. F. Hoefler, B. Kunert, H. Plank, T. Rath and G. Trimmel, *ACS Appl. Energy Mater.*, 2018, **1**, 343-347.

58. T. Matsui, T. Yamamoto, T. Nishihara, R. Morisawa, T. Yokoyama, T. Sekiguchi and T. Negami, *Adv. Mater.*, 2019, **31**, 1806823.

59. Q. Chen, H. Zhou, Z. Hong, S. Luo, H.-S. Duan, H.-H. Wang, Y. Liu, G. Li and Y. Yang, *J. Am. Chem. Soc.*, 2014, **136**, 622-625.

60. X. Li, D. Bi, C. Yi, J.-D. Décoppet, J. Luo, S. M. Zakeeruddin, A. Hagfeldt and M. Grätzel, *Science*, 2016, **353**, 58-62.

61. M. A. Afroz, R. K. Gupta, R. Garai, M. Hossain, S. P. Tripathi and P. K. Iyer, *Org. Electron.*, 2019, **74**, 172-178.

62. S. Paek, P. Schouwink, E. N. Athanasopoulou, K. T. Cho, G. Grancini, Y. Lee, Y. Zhang, F. Stellacci, M. K. Nazeeruddin and P. Gao, *Chem. Mater.*, 2017, **29**, 3490-3498.

63. R. Sedighi, F. Tajabadi, S. Shahbazi, S. Gholipour and N. Taghavinia, *ChemPhysChem*, 2016, **17**, 2382-2388.

64. Z. Xiao, Q. Dong, C. Bi, Y. Shao, Y. Yuan and J. Huang, *Adv. Mater.*, 2014, **26**, 6503-6509.

65. M. Xiao, F. Huang, W. Huang, Y. Dkhissi, Y. Zhu, J. Etheridge, A. Gray-Weale, U. Bach, Y.-B. Cheng and L. Spiccia, *Angew. Chem., Int. Ed.*, 2014, **53**, 9898-9903.

66. B. Chen, M. Yang, X. Zheng, C. Wu, W. Li, Y. Yan, J. Bisquert, G. Garcia-Belmonte, K. Zhu and S. Priya, *The Journal of Physical Chemistry Letters*, 2015, **6**, 4693-4700.

67. F. X. Xie, D. Zhang, H. Su, X. Ren, K. S. Wong, M. Grätzel and W. C. H. Choy, *ACS Nano*, 2015, **9**, 639-646.

68. M. Kim, S. G. Motti, R. Sorrentino and A. Petrozza, *Energy Environ. Sci.*, 2018, **11**, 2609-2619.

69. N. J. Jeon, J. H. Noh, Y. C. Kim, W. S. Yang, S. Ryu and S. I. Seok, *Nat. Mater.*, 2014, **13**, 897-903.

70. Y. Shao, Y. Fang, T. Li, Q. Wang, Q. Dong, Y. Deng, Y. Yuan, H. Wei, M. Wang, A. Gruverman, J. Shield and J. Huang, *Energy Environ. Sci.*, 2016, **9**, 1752-1759.

71. B. Jeong, S. M. Cho, S. H. Cho, J. H. Lee, I. Hwang, S. K. Hwang, J. Cho, T.-W. Lee and C. Park, *Phys. Status Solidi RRL*, 2016, **10**, 381-387.

72. Y. Yue, N. Salim, Y. Wu, X. Yang, A. Islam, W. Chen, J. Liu, E. Bi, F. Xie, M. Cai and L. Han, *Adv. Mater.*, 2016, **28**, 10738-10743.

73. K. J. Xu, R. T. Wang, A. F. Xu, J. Y. Chen and G. Xu, *ACS Appl. Mater. Interfaces*, 2020, **12**, 48882-48889.

74. P. Zhao, B. J. Kim and H. S. Jung, *Mater. Today Energy*, 2018, **7**, 267-286.

75. Z. Zhang, J. Wu, S. Li, S. Liu, Q. Wang, A. Mei, Y. Rong, H. Han and Y. Hu, *Solar RRL*, 2020, **4**, 1900248.

76. M. Adil Afroz, N. Ghimire, K. M. Reza, B. Bahrami, R. S. Bobba, A. Gurung, A. H. Chowdhury, P. K. Iyer and Q. Qiao, *ACS Appl. Energy Mater.*, 2020, **3**, 2432-2439.

77. L. Guan, N. Jiao and Y. Guo, *J. Phys. Chem. C*, 2019, **123**, 14223-14228.

78. Y. Guo, W. Sato, K. Shoyama, H. Halim, Y. Itabashi, R. Shang and E. Nakamura, *J. Am. Chem. Soc.*, 2017, **139**, 9598-9604.

79. L. Zhang, F. Yu, L. Chen and J. Li, *Appl. Surf. Sci.*, 2018, **443**, 176-183.

80. Y. Zhang, Q. Wang, K. Duan, L. Wang, L. Tao, J. Zhang, H. Wang and Z. Huo, *J Solid State Electrochem.*, 2021, **25**, 1531-1540.

81. N. K. Noel, A. Abate, S. D. Stranks, E. S. Parrott, V. M. Burlakov, A. Goriely and H. J. Snaith, *ACS Nano*, 2014, **8**, 9815-9821.

82. K. Wang, J. Liu, J. Yin, E. Aydin, G. T. Harrison, W. Liu, S. Chen, O. F. Mohammed and S. De Wolf, *Adv. Funct. Mater.*, 2020, **30**, 2002861.

83. K. Cao, Y. Huang, M. Ge, F. Huang, W. Shi, Y. Wu, Y. Cheng, J. Qian, L. Liu and S. Chen, *ACS Appl. Mater. Interfaces*, 2021, **13**, 26013-26022.

84. D. Xin, S. Tie, R. Yuan, X. Zheng, J. Zhu and W.-H. Zhang, *ACS Appl. Mater. Interfaces*, 2019, **11**, 44233-44240.

85. T. Niu, J. Lu, R. Munir, J. Li, D. Barrit, X. Zhang, H. Hu, Z. Yang, A. Amassian, K. Zhao and S. Liu, *Adv. Mater.*, 2018, **30**, 1706576.

86. Y. Lin, L. Shen, J. Dai, Y. Deng, Y. Wu, Y. Bai, X. Zheng, J. Wang, Y. Fang, H. Wei, W. Ma, X. C. Zeng, X. Zhan and J. Huang, *Adv. Mater.*, 2017, **29**, 1604545.

87. W. Zhou, D. Li, Z. Xiao, Z. Wen, M. Zhang, W. Hu, X. Wu, M. Wang, W.-H. Zhang, Y. Lu, S. Yang and S. Yang, *Adv. Funct. Mater.*, 2019, **29**, 1901026.

88. X. Zhu, M. Du, J. Feng, H. Wang, Z. Xu, L. Wang, S. Zuo, C. Wang, Z. Wang, C. Zhang, X. Ren, S. Priya, D. Yang and S. Liu, *Angew. Chem., Int. Ed.*, 2021, **60**, 4238-4244.

89. L. Zuo, H. Guo, D. W. deQuilettes, S. Jariwala, N. De Marco, S. Dong, R. DeBlock, D. S. Ginger, B. Dunn, M. Wang and Y. Yang, *Sci. Adv.*, 2017, **3**, e1700106.

90. S. Wang, Z. Zhang, Z. Tang, C. Su, W. Huang, Y. Li and G. Xing, *Nano Energy*, 2021, **82**, 105712.

91. H. Wang, J. Wu, J. Song, J. Qu, J. Lian, P.-C. Qian and W.-Y. Wong, *Chem. Eng. J.*, 2021, **417**, 128068.

92. A. Krishna, S. Gottis, M. K. Nazeeruddin and F. Sauvage, *Adv. Funct. Mater.*, 2019, **29**, 1806482.

93. E.-B. Kim, M. S. Akhtar, H.-S. Shin, S. Ameen and M. K. Nazeeruddin, *J. Photochem. Photobiol. C*, 2021, **48**, 100405.

94. M. A. Mahmud, T. Duong, J. Peng, Y. Wu, H. Shen, D. Walter, H. T. Nguyen, N. Mozaffari, G. D. Tabi, K. R. Catchpole, K. J. Weber and T. P. White, *Adv. Funct. Mater.*, 2021, **n/a**, 2009164.

CHAPTER 2

Microwave Synthesis for High-Performance Ambient-Condition-Processed Organic Solar Cells

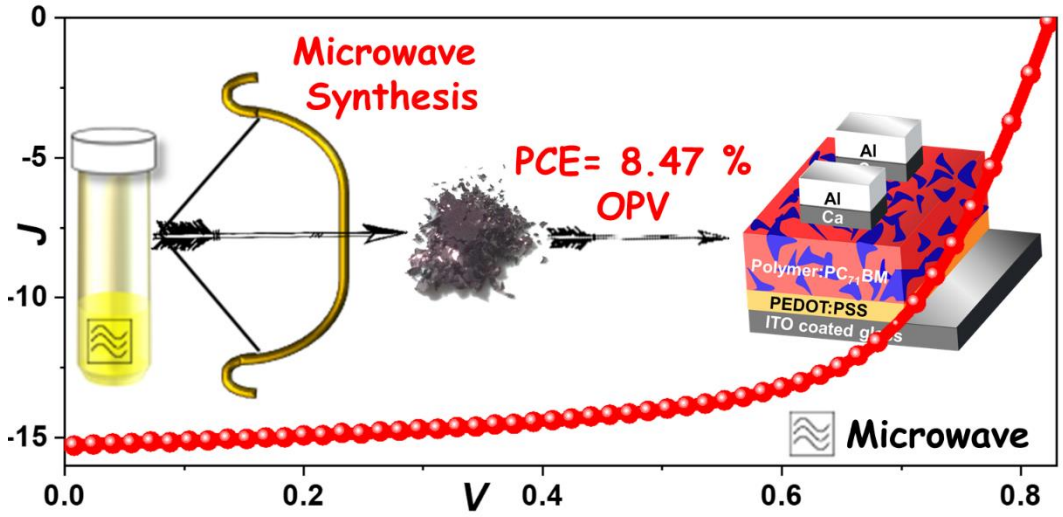

Manuscript: Rabindranath Garai, Mohammad Adil Afroz, Ritesh Kant Gupta, Anwesha Choudhury, Parameswar Krishnan Iyer, "Quick and Energy Efficient Synthesis of PTB7-Th through Closed Microwave Reactor for High-performance Polymer Solar Cells." *ACS Omega*, 2020, **5**, 2747-2754.

Patent: Parameswar Krishnan Iyer, **Rabindranath Garai**, Mohammad Adil Afroz, Ritesh Kant Gupta, "PTB7-Th donor polymer-based Donor- acceptor (D-A) conducting polymer (CPs) suitable for polymer solar cells (PSC) and devices thereof", Ref. No. 201931020744, Appl. No. TEMP/E-1/21812/2019-KOL.

[This page was intentionally left blank]

Abstract

The large-scale commercial synthesis of bulk heterojunction (BHJ) solar cell materials is very challenging, time and energy consuming. Synthesis of π-conjugated polymers with uniform batch to batch molecular weight and low dispersity is a key requirement for better reproducibility of high efficiency polymer solar cell. Herein, the conjugated polymer (CP) PTB7-Th, well-known for its high performance, has been synthesized in high molecular weight and low dispersity through closed microwave reactor. The microwave reaction procedure is known to be more controlled and consumes lesser energy. The precursors were strategically reacted for different reaction time durations to obtain optimum molecular weight. All the different CPs were well characterized using ^{1}H NMR, GPC, UV-vis, Photoluminescence (PL), ESR and Raman spectroscopy whereas the film morphology was extensively studied via atomic force microscopy (AFM) and Grazing Incidence X-ray Diffraction (GIXRD) techniques. The effect of molecular weight on the conventional BHJ solar cell with $PC_{71}BM$ acceptor was investigated to derive a systematic structure-property relationship. The ambient conditions processed BHJ device, fabricated with the CP obtained after 35 minutes reaction time, provided the best performance with power conversion efficiency (PCE) of 8.09%. This result is quite similar to the results of CPs synthesized via thermal route. Enhanced PCE of 8.47% was obtained for the optimized polymer (35 minutes microwave reaction product) when device fabrication was carried out inside the glove box.

2.1 Overview

Polymer/Organic solar cells (OSCs) have gained great attention recently as one of the leading fields within photovoltaic research because of its unique advantages such as light weight, flexibility, easy fabrication, low-cost, quick energy payback time and ease of device fabrication scaleup.[1-8] The most established and widely studied device concept among all OSCs is the bulk-heterojunction (BHJ) system, where an acceptor and a donor molecule having complementary optical absorption behaviour and well matched energy levels are blended together to provide a distinct active layer. Power conversion efficiency (PCE) of >13% has been reported by designing and developing new molecules and applying different device engineering.[9-12]

Quite a few molecular designing strategies have been established over the past few years to optimize the optical properties and band gap of donor materials.[13] The donor (D)-acceptor (A) co-polymerized CPs with low band gap are widely used as the most successful donors in the active layer of BHJ for improved performance. The optoelectronic properties of the CPs can also be tuned by D-A structure variation, side chain modulation and modification of functional groups.[13, 14] Commonly, these π-conjugated copolymers are synthesized by $Pd(Ph_3)_4$ catalyzed Stille polycondensation.[15] For several D-A CPs, it has been reported that molecular weight (M_w) and polydispersity index (Đ) of the CPs largely affect the hole mobility, molecular orientation, crystallinity, optoelectronic properties, thin film morphology and device performance.[16-20] Generally, higher molecular weight CPs demonstrate better PCE due to enhanced charge carrier mobility, better optical absorption, and superior intermixed film morphology.[19-21] Yet, CPs with much higher M_w have solubility problems leading to poor BHJ morphology as well as lesser PCE. Recently, it has also been established that with increasing Đ values of the CPs, the PCE drops gradually.[22] Therefore, CPs with optimum M_w and lower Đ is needed for better device performances. However, the CPs synthesized from metal-catalyzed polycondensation reactions, lead to inconsistent device performances from one synthetic batch to another batch. This batch-to-batch variation is due to the differences in M_w, Đ and residual palladium contamination in various batches.[23-25] It is also challenging to synthesize these CPs on large scale for commercialization. Hence, various methodologies have been carefully investigated for the improvement of Stille coupling reaction protocol. A recent article has discussed the comparison between the CPs achieved from $Pd_2(dba)_3/P(o\text{-}tol)_3$ and $Pd(PPh_3)_4$-catalysed Stille polycondensation.[26] Another report disclosed almost

negligible batch to batch variations in OPV performance acquired from the stepwise heating in Stille coupling reaction.[27] Nowadays, microwave (MW) assisted Stille co-polymerization has also been used to synthesize higher Mw CPs with lesser Đ.[28, 29] The MW reactions in closed (pressurized) reactor is much more advantageous in terms of ultra-fast and homogeneous heating, lesser solvent use that decreases the side reactions and improves the reaction yields to provide a ultrahigh quality product. This MW process is also more energy-efficient than conventional heating as well as open vessel microwave reaction.[30, 31]

Herein, we present the strategic synthesis of a well-known high-performance donor CP (PTB7-Th) through Stille polycondensation in a closed MW reactor. PTB7-Th CPs with different molecular weight have been synthesized by varying the MW reaction time from 25 min to 45 min in single step heating. All the CPs have been characterized by ^{1}H NMR, GPC, UV-vis, PL, Raman, ESR spectroscopy, AFM and GIXRD to reveal the structural differences in terms of D-A ratios and backbone purity. The conventional BHJ devices were fabricated with these MW CPs in combination with $PC_{71}BM$ and the photovoltaic results are extensively correlated with the properties of CPs. Multistep heating reactions were also performed, but they resulted in poor device performance and stability.

2.2 Results and Discussions

The optical absorption of the microwave (MW) and thermally synthesized CPs is depicted in **Figure 2.1a**. All the CPs exhibit almost similar absorption behavior with a predominant absorption peak at ~705 nm along with an additional peak at ~635 nm. The lower wavelength shoulder peaks appear with equal intensity for MW25m, MW35m and Thermal CPs, while this is largely increased for MW45m CP. Moreover, absorption spectrum for MW45m becomes more broadened and shifted almost 6 nm as compared with the other CPs (**Table 2.1**). These absorption behaviours suggest that MW45m contains higher proportion of homo-coupled units such as BDTT-BDTT and FTT-FTT in the CP backbone.[22, 32] The optical absorption in the blend films (**Figure 2.1b**) revealed that the light harvesting property initially increases with increasing molecular weight but declines for very high molecular weight.

The backbone irregularities of the CPs were well examined by Raman spectroscopy (**Figure 2.1c**). The vibrational modes of thiophenes, existing in the CPs, are Raman active because of their prominent coupling with the delocalized π-electrons. All the CPs disclose

five significant Raman peaks.[28] Although Thermal, MW25m and MW35m exhibit similar spectra, MW45m shows a significant change in Raman vibrational modes. The coupled vibration of the stretching mode (C=C) of fused thiophenes (present in BDTT unit) to the un-fluorinated thiophenes of FTT unit (peak 3) and the coupled vibration of the stretching mode (C=C) of the un-fluorinated thiophene to quadrant stretching mode (peak 4) of MW45m illustrates a much broader and higher intensity spectrum. Also stretching modes (C=C) of the side chain thiophenes in BDTT unit (peak 1) of this CP is observed with higher intensity along with a shift of ~ 3 cm^{-1} to higher wavenumbers. This enhanced intensity of the vibrational modes in Raman spectrum is evident for the presence of homo-coupled units in the CP main chain. Hence thermal, MW25m and MW35m have a much lower quantity of defective units as compared to MW45m. These defective units in the CP backbone can act as deep traps in the photovoltaic devices and might hamper device performance.

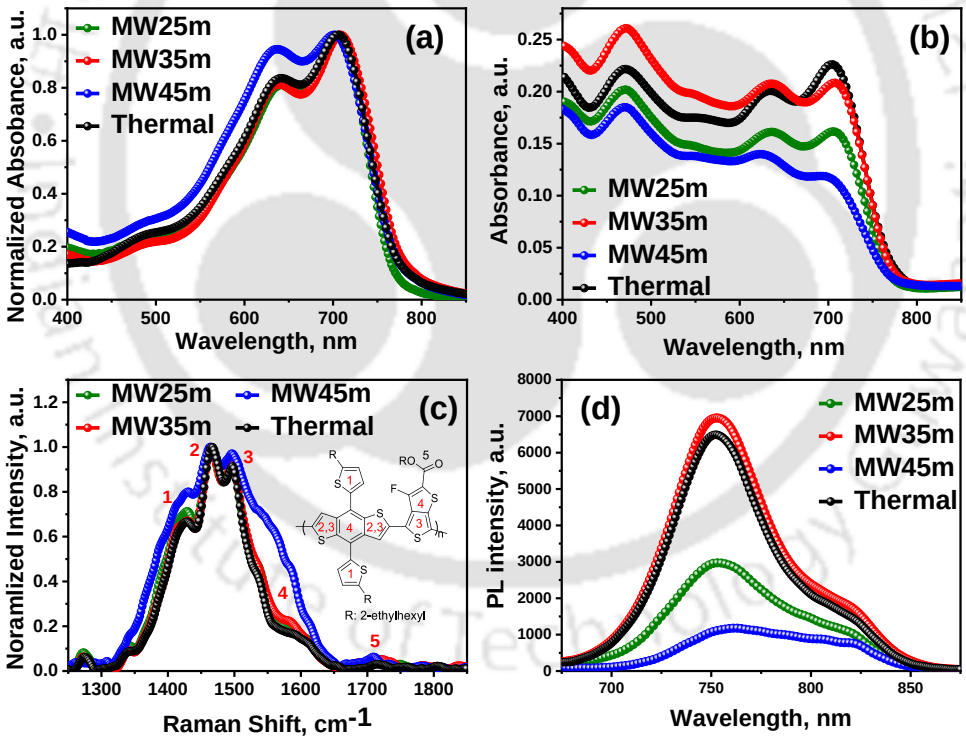

Figure 2.1 UV-vis absorption spectra of (a) CP thin films, (b) Polymer-$PC_{71}BM$ blend thin film, (c) Raman spectra under 514 nm excitation, and (d) PL spectra of CP thin films.

Photoluminescence (PL) study (**Figure 2.1d**) was performed to estimate the emission strength of the CPs having different molecular weights. MW35m has an improved emission than MW25m due to its higher molecular weight. Thermal CP has also revealed slightly lower emission in comparison to MW35m. However, MW45m shows a lower emission in

spite of having high molecular weight. This can be described by considering the structural defects hence self-quenching caused by photo induced charge transfer from the regular repeating units of the CP to the homo-coupled defect units.

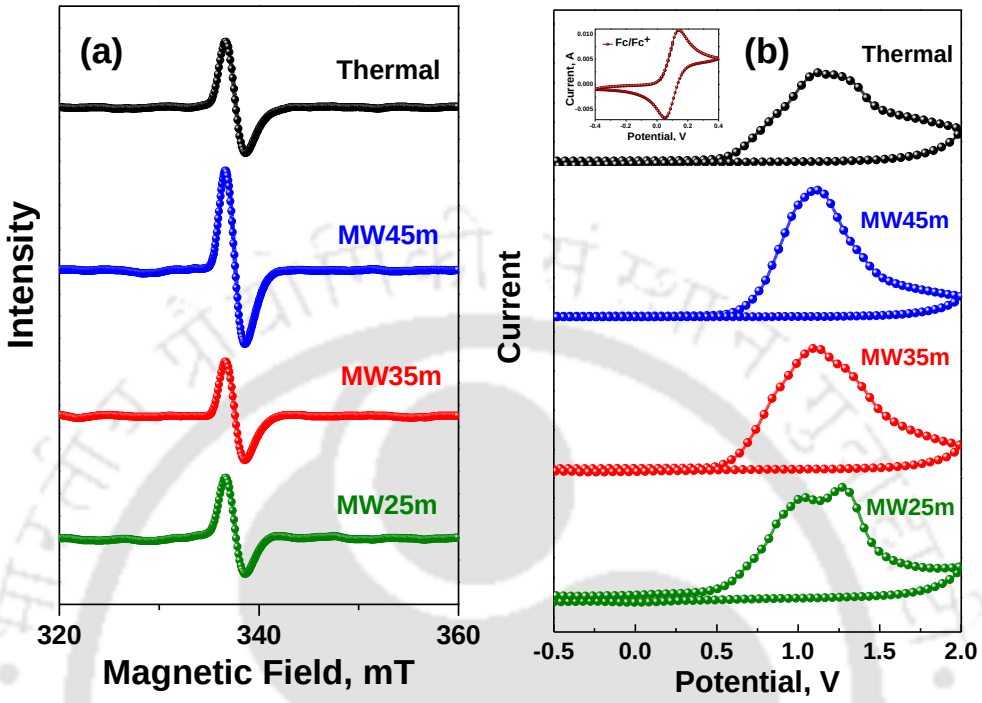

Figure 2.2 (a) X-band RT dark ESR spectra of MW25m, MW35m and MW45m powders, and (b) CV spectra of polymers.

Considering the information about the synthesis and the physical characteristics of the synthesized CPs, it can be assumed that the molecular framework of the CPs does not introduce any spin active species. Therefore, the ESR spectra of the studied CPs should not display any type of ESR signal. Nevertheless, it reveals a prominent ESR signal which evidences the existence of radical species (**Figure 2.2a**). It is believed that the presence of ESR signal is due to some structural defects of the CP backbone or some unpaired electrons coming from chemical impurities. These radical species may act as deep traps for mobile charge carriers and greatly affect the solar cell device performance of the CP.[33] ESR spectra of all the CPs showed similar polycrystalline pattern with g factor of 1.998±0.001. The signal intensity is proportionate to radical species concentration. MW25m and MW35m have demonstrated almost comparable signal intensity which leads to equivalent radical concentration. Thermal CP has shown higher signal intensity in comparison to MW35m. However, MW45m leads to much higher radical concentration as a result of its enhanced signal intensity. Hence MW45m exhibits more trap states than MW25m and MW35m which could hinder the charge transport in the solar cell device. From this result we can

expect that the MW45m CP will give less photocurrent (J_{sc}) and mobility. The electrochemical behaviour of the CPs was studied with cyclic voltammetry (**Figure 2.2b**). The highest occupied molecular orbital (HOMO) and the lowest unoccupied molecular orbital (LUMO) energy levels of all the CPs were also calculated (**Table 2.1**). MW45m exhibits a lower lying HOMO as compared to other CPs.

Table 2.1: Molecular weight, optical properties and electronic energy levels of the synthesized polymers.

Polymer	Mn (kDa)	Mw (kDa)	PDI	λ_{max}^{film} (nm)	λ_{edge}^{film} (nm)	$E_g^{Optical}$ (eV)	HOMO (eV)	LUMO (eV)
MW25m	27.6	64.1	2.32	706	772	1.60	-5.31	-3.71
MW35m	63.1	167.2	2.65	708	784	1.58	-5.32	-3.74
MW45m	66.9	202.3	3.02	701	779	1.59	-5.39	-3.80
Thermal	49.5	149.3	3.01	706	779	1.59	-5.29	-3.70

Table 2.2: Photovoltaic parameters of PSCs under standard AM1.5G illumination.

Device	J_{SC}, mA-cm^{-2}	V_{OC}, V	FF	PCE, % (Ave. PCE, %)
MW25m	11.97	0.819	0.61	5.97 (5.54 ± 0.33) [a]
MW35m	15.30	0.826	0.64	8.09 (7.53 ± 0.33) [b]
MW45m	7.24	0.858	0.50	3.12 (2.61 ± 0.34) [a]
Thermal	15.27	0.817	0.63	7.91 (7.27 ± 0.47) [a]

[a]Average PCE of 10 devices and [b] average PCE of 30 devices are listed.

OPV devices with conventional architecture were fabricated for the assessment of photovoltaic properties of the donor CP along with $PC_{71}BM$ as acceptor. During device fabrication the active layer was spin coated in ambient conditions (outside the glove box in presence of air). The current density–voltage (*J*–*V*) characteristics of the air processed devices for the four CPs are shown in **Figure 2.3a** (The data is summarized in **Table 2.2**). The data indicates that, with increasing molecular weight of the CPs (from 64.1 kDa to 167.2 kDa), PCE enhanced significantly from 5.97 % to 8.09 %. However, further increase in molecular weight results in a reduction of PCE. A comparable trend in the PCE with the molecular weight of thermally synthesized PTB7-Th along with non-fullerene acceptors has already been reported.[22] The maximum performance is achieved for MW35m with an

open circuit voltage (V_{oc}) of 0.826 V, fill factor (FF) of 64%, short-circuit current density (J_{sc}) of 15.30 mA cm^{-2}, and a PCE of 8.09% for best device. This is one of the highest efficiency reports for air processed OSCs with PTB7-Th as donor in conventional device configuration. A comparable PCE of 7.91 % is achieved with the Thermal CP. A high FF above 60% is witnessed for CP samples up to 167.2 kDa, while a drop in FF is seen almost up to 50% with further increasing the molecular weight. There are solubility issues, differences in intermixed film morphology and crystallinity for very high molecular weight CPs which reduces the FF. Yet MW45m shows relatively higher V_{oc} than the other two CPs mainly because of low lying HOMO. Therefore, an optimal molecular weight is essential for better solar cell performance.

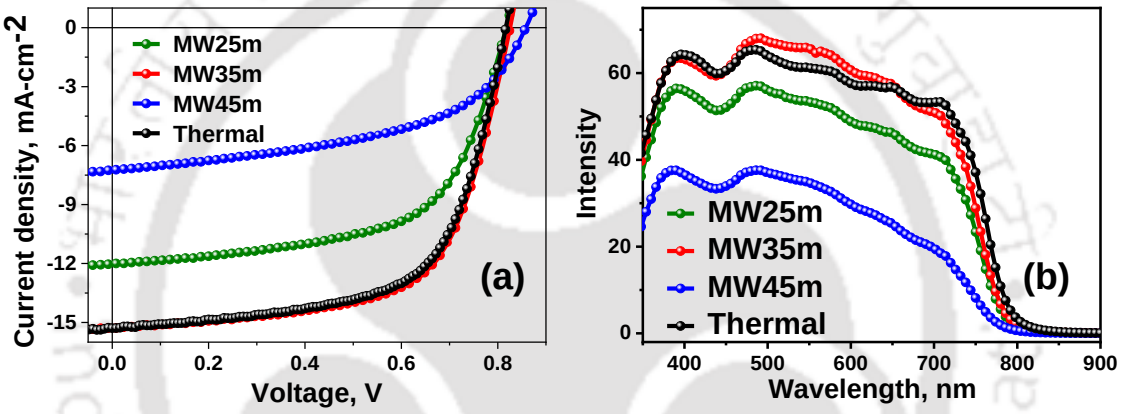

Figure 2.3 (a) *J-V* curve and (b) EQE curve.

External quantum efficiency (EQE) spectra of all the solar cell devices demonstrate a strong photo response in broad spectral region from 300−800 nm (**Figure 2.3b**). The considerable variations of the J_{sc} values, obtained from the *J-V* measurements, are well-reflected in their EQE spectra. The integrated J_{sc} values calculated from EQE spectra are 14.27, 11.81, 14.36 and 6.95 mA-cm^{-2} for Thermal, MW25m, MW35m and MW45m respectively with a discrepancy of ~7% compared to the Jsc obtained from *J-V* curve. This mismatch may be attributed to the different measurement conditions. The *J-V* characterizations were carried out inside a glove box under argon atmosphere, whereas the EQE measurements were executed outside the glove box. Moreover, the CPs synthesized from different batches of microwave reaction lead to outstanding reproducibility by suppressing the batch to batch variation in solar cell device performance (**Figure 2.4**).

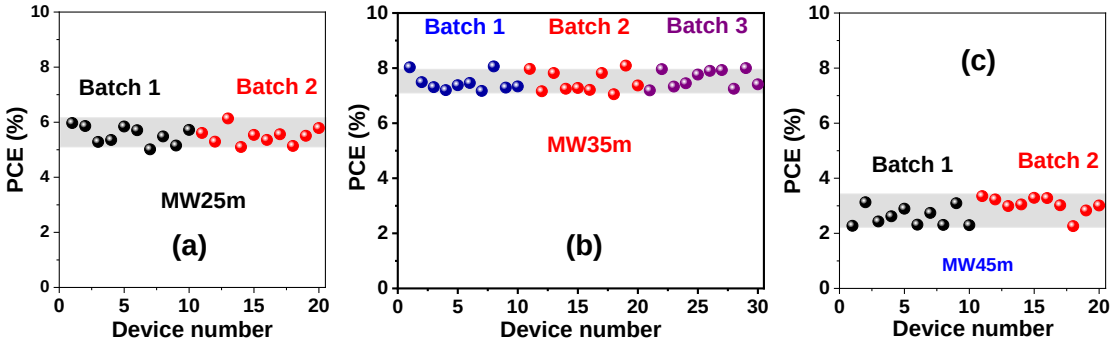

Figure 2.4 Efficiency variation of devices fabricated in different batches using (a) MW25m, (b) MW35m and (c) MW45m.

The blend films morphology was extensively studied by atomic force microscopy (AFM) to reveal the effect of molecular weight of the MW synthesized CPs (**Figure 2.5a-d**). The topographic images of the blend films did not display any difference in microstructures with a comparable *rms* roughness of ~1.4 nm for all the films. The morphology of the donor - acceptor blends were further evaluated through the Grazing Incidence X-ray study (GIXRDs) to obtain a clear insight into the crystallinity and molecular packing of different films. **Figure 2.5e-h** shows the 2D q-plot of the blend films of the three samples. All four blends showed unique characteristics of concentric circles in their films. No prominent concentric circles are found in any of the samples. But looking at the 2D q-plot it can be confirmed that film of MW35m blend is the most crystalline having one discrete circle and film of MW45m blend is found to be the most amorphous having diffused circles in the 2D q-plot. The crystallinity of the film of Thermal and MW25m blend is in between the MW35m and MW45m samples. The lamellar peaks (100) are observed in the in-plane profile at q_{xy} = 2.78 nm^{-1}, 2.71 nm^{-1}, 2.86 nm^{-1} and 2.64 nm^{-1} and calculated lamellar spacing are 2.26, 2.32 nm, 2.20 nm and 2.38 nm for blend of Thermal, MW25m, MW35m and MW45m respectively (**Figure 2.6** and **Table 2.3**). Hence, MW45m exhibits highest lamellar spacing among all and hence transport of charge becomes difficult. Similarly, the π-π stacking peaks have been calculated from 1D line cut obtained at q_z = 13.31 nm^{-1}, 13.31 nm^{-1}, 13.31 nm^{-1} and 13.46 nm^{-1} for blend of thermal, MW25m, MW35m and MW45m respectively and the calculated π-π spacing to be ~0.47. The lamellar peak intensity of MW35m is much higher in comparison to other CPs in the in-plane and as well as the out-of-plane directions. Similar trend is also observed for the π-π stacking peak intensity. This data indicates that MW35m exhibits a more preferential face-on orientation than other CPs. The face-on orientation in donor acceptor blend is favourable for better vertical charge

transport which improves OSCs performance. This result can be well compared with the device result as the MW35m blend displaying highest PCE (also J_{sc}) and MW45m blend displaying the lowest PCE.

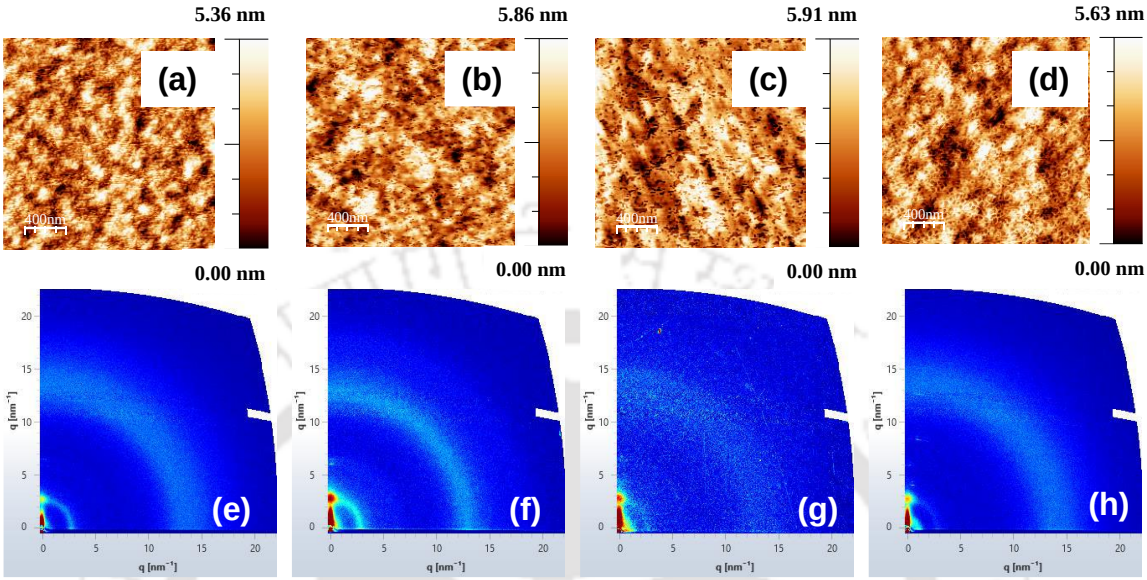

Figure 2.5 AFM images of donor-acceptor blend for (a) MW25m (b) MW35m (c) MW45m (d) Thermal; 2D GIWAX images of donor-acceptor blend for (e) MW25m (f) MW35m (g) MW45m (h) Thermal.

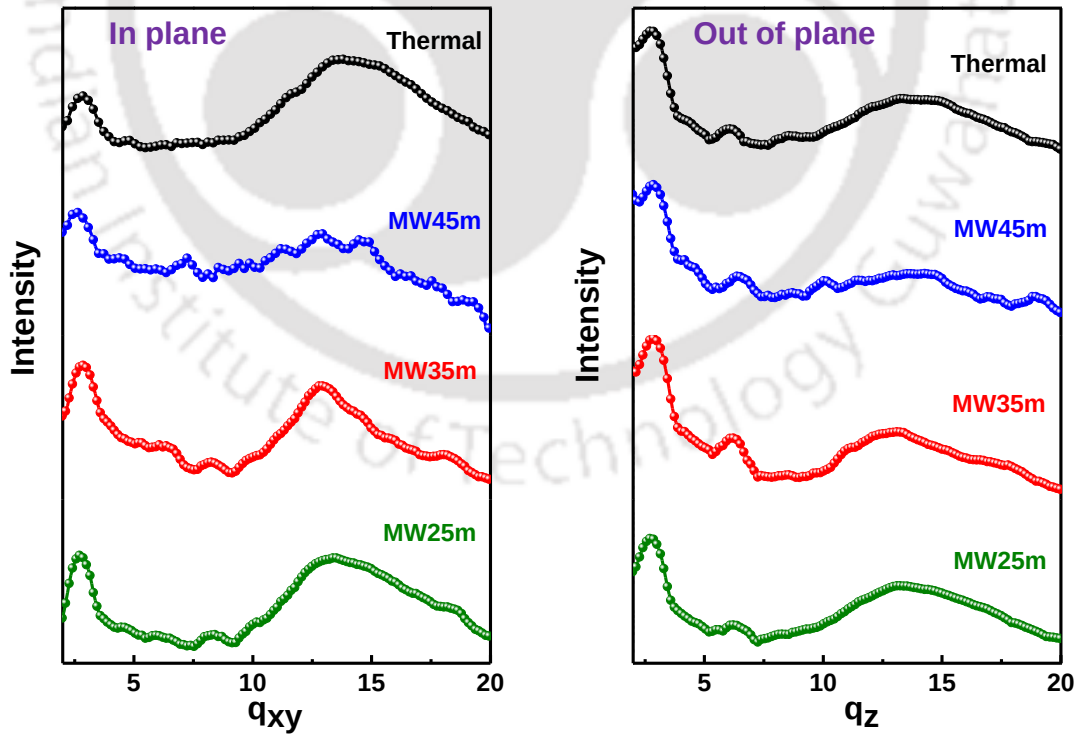

Figure 2.6 1D GIXRD profile of the polymer blends in plane (left) and out of plane (right).

Table 2.3: Crystallographic parameters derived from 1D GIXRD measurements.

Films	**Lamellar spacing (In-plane direction)**		**π-π stack distance (Out-of-plane direction)**	
	q_{xy} (nm^{-1})	**d-spacing (nm)**	**q_z (nm^{-1})**	**d-spacing (nm)**
MW25m:$PC_{71}BM$	2.71	2.32	13.31	0.47
MW35m:$PC_{71}BM$	2.86	2.20	13.31	0.47
MW45m:$PC_{71}BM$	2.64	2.38	13.46	0.47
Thermal:$PC_{71}BM$	2.78	2.26	13.31	0.47

However, to further increase the device performance of the optimized CP MW35m, the devices are fabricated inside glove box to observe an enhanced PCE of 8.47% (**Figure 2.7a**). Stability is a very important parameter for any type of solar cell for real life application. The thermal stability of the best device was studied for un-encapsulated device stored in argon atmosphere. For this study the device was heated at 70 °C and thermally synthesized PTB7-Th devices was taken as control. It could be clearly seen that the MW synthesized CP showed better thermal stability compared to the Thermal CP (**Figure 2.7b**). Both the CPs revealed a sharp decay in their PCE within first 250 minutes. After that the efficiency of MW35m entered into a stable zone and remained almost unchanged whereas for Thermal, the PCE kept on decreasing. After 1500 minutes of heating MW35m degraded up to 56% but the Thermal retained only 16% of its original PCE.

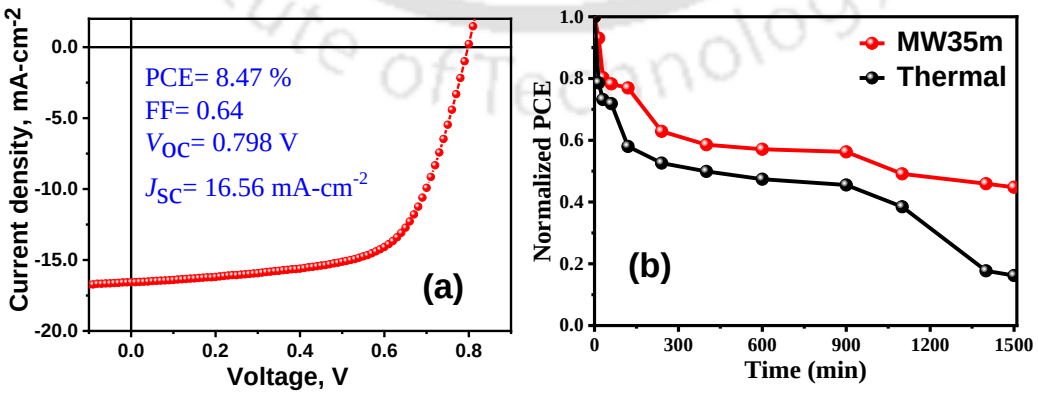

Figure 2.7 (a) *J-V* of the device fabricated in globe box, and (b) Thermal stability studies of MW35m and Thermal PTB7-Th CPs

2.3 Conclusions

In this work, the control synthesis of PTB7-Th via closed vessel microwave reactor has been successfully achieved. This reaction protocol is very convenient to synthesize CPs with higher M_w, and comparatively lower Đ consuming much lower energy. Importantly, this method offers much better-quality materials for devices with very less batch to batch variation, which is very important for large scale commercial synthesis of donor CPs through Stille polycondensation. As a remarkable development, the device fabrication was carried out at ambient conditions unlike most cases where strict inert atmosphere is followed. MW35m [with higher M_w of 167.2 kDa and lower Đ values (2.67)] shows efficiency of 8.09% with a FF of 64%, a V_{OC} of 0.826 V and a J_{sc} of 15.30 mA cm^{-2}, that is very consistent and better than the CP synthesized through thermal route, and which was further improved to ~8.5% PCE in devices fabricated inside the glove box. These PCE values are among the highest efficiency for PTB7-Th in air / ambient processed as well as inert condition devices.

2.4 Experimental Section

Materials and Methods: The monomers 2-ethylhexyl-4,6-dibromo-3-fluorothieno[3,4-b]thiophene-2-carboxylate [FTT] and (4,8-bis(5-(2-ethylhexyl)thiophen-2-yl)-benzo[1,2-b:4,5-b′]dithiophene-2,6-diyl)bis(trimethylstannane) [BDTT] were obtained from Derthon Optoelectronic Materials Science Technology Co. Ltd. and directly used. ITO substrates (15 Ω $□^{-1}$) and $PC_{71}BM$ (>99.5 %) were obtained from LUMTEC, PEDOT:PSS (PVP AI 4083) was obtained from Clevios. All other chemicals were used as received.

Synthesis and characterization of CPs: Monomers BDTT (100 mg, 0.11 mmol) along with FTT (52 mg, 0.11 mmol) were introduced into a microwave reactor vessel (closed). A solvent mixture of toluene-DMF (3:1, 2 mL) was added to it. After that argon was purged for 20 min and $Pd(PPh_3)_4$ catalyst was then added to the reaction mixture and again argon was purged for twenty min. Finally, the reactor vessel was refluxed at 150 °C under microwave conditions (microwave power 150 W and pressure 20 psi) for different time durations (25 min, 30 min, 35 min, 40 min, and 45 min) strategically to prepare CPs with varying molecular weight. After completion, the resulting CP solution was precipitated in 200 mL methanol. The precipitate was then further purified through soxhlet extraction sequentially with 300 mL each of methanol, hexane, acetone and chloroform. Again, the

solution was passed through celite bed. The CP was further precipitated in methanol and finally the pure CP was dried in vacuum. This CP was also synthesized by conventional heating method (thermal heating on a hot plate) according to literature process.[34] All the CPs were characterized via ^{1}H-NMR spectroscopy and GPC .

MW25m: (Yield 61 %) ^{1}H NMR (400 MHz, $CDCl_3$) δ (ppm): 7.20-7.71 (br, 5 H), 6.62-7.02 (br, 2 H), 4.00-4.52 (br, 2 H), 2.55-3.26 (br, 4 H), 0.71-1.98 (br, 46 H).

MW35m: (Yield 65 %) ^{1}H NMR (400 MHz, $CDCl_3$) δ (ppm): 7.21-7.89 (br, 5 H), 6.61-7.04 (br, 2 H), 3.97-4.56 (br, 2 H), 2.46-3.23 (br, 4H) 0.71-1.94 (br, 46 H).

MW45m: (Yield 56 %) ^{1}H NMR (400 MHz, $CDCl_3$) δ (ppm): 7.18-7.84 (br, 5 H), 6.56-6.99 (br, 2 H), 4.06-4.59 (br, 2 H), 2.63-3.29 (br, 4 H), 0.72-1.95 (br, 46 H).

Thermal: (Yield 54 %) ^{1}H NMR (400 MHz, $CDCl_3$) δ (ppm): 7.23-7.69 (br, 5 H), 6.69-7.04 (br, 2 H), 4.07-4.59 (br, 2 H), 2.65-3.27 (br, 4 H), 0.67-1.96(br, 46 H).

Device Fabrication: OSC devices were fabricated with the conventional architecture of ITO/PEDOT:PSS/Donor polymer:$PC_{71}BM$/Ca/Al. Each device had a cell area of 0.06 cm^2. The donor-acceptor blend solution (for active layer) was prepared, using chlorobenzene (CB) as a processing solvent in a concentration of 35 mg/mL (D/A ratio 1:1.5). Then it was kept at 50 °C and constantly stirred for 6 hours for proper dissolution, and small amount (3%, volume) of DIO was also added to it 15 minutes before spin coating. Patterned ITO glasses were cleaned sequentially using DI water, acetone and isopropanol. Then, it was dried using dry N_2 gas and UV ozone treatment was carried out for 20 mins. Next, PEDOT:PSS (AI4083) was spin-coated on the ITO substrate @ 4000 rpm and then annealed at 140 °C for 10 mins. After cooling, the blend solution was spin-coated @ 3000 rpm followed by methanol treatment for the removal of DIO.[38] Lastly, Calcium (~20 nm) and Aluminium (~100 nm) were thermally deposited (*ca.* 5×10^{-6} Pa) onto the MeOH treated active layer. Except metal deposition whole device was fabricated in ambient conditions.

References

1. A. J. Heeger, *Advanced Materials*, 2014, **26**, 10-28.
2. L. Lu, T. Zheng, Q. Wu, A. M. Schneider, D. Zhao and L. Yu, *Chemical Reviews*, 2015, **115**, 12666-12731.
3. F. C. Krebs, S. A. Gevorgyan and J. Alstrup, *Journal of Materials Chemistry*, 2009, **19**, 5442-5451.
4. Y. Li, *Accounts of Chemical Research*, 2012, **45**, 723-733.
5. H. Kang, G. Kim, J. Kim, S. Kwon, H. Kim and K. Lee, *Advanced Materials*, 2016, **28**, 7821-7861.
6. C.-C. Chen, L. Dou, R. Zhu, C.-H. Chung, T.-B. Song, Y. B. Zheng, S. Hawks, G. Li, P. S. Weiss and Y. Yang, *ACS Nano*, 2012, **6**, 7185-7190.
7. C. H. Peters, I. T. Sachs-Quintana, J. P. Kastrop, S. Beaupré, M. Leclerc and M. D. McGehee, *Advanced Energy Materials*, 2011, **1**, 491-494.
8. S. B. Darling and F. You, *RSC Advances*, 2013, **3**, 17633-17648.
9. W. Zhao, S. Li, H. Yao, S. Zhang, Y. Zhang, B. Yang and J. Hou, *Journal of the American Chemical Society*, 2017, **139**, 7148-7151.
10. W. Zhao, S. Li, S. Zhang, X. Liu and J. Hou, *Advanced Materials*, 2017, **29**, 1604059.
11. M. Li, K. Gao, X. Wan, Q. Zhang, B. Kan, R. Xia, F. Liu, X. Yang, H. Feng, W. Ni, Y. Wang, J. Peng, H. Zhang, Z. Liang, H.-L. Yip, X. Peng, Y. Cao and Y. Chen, *Nature Photonics*, 2017, **11**, 85-90.
12. Z.-G. Zhang, B. Qi, Z. Jin, D. Chi, Z. Qi, Y. Li and J. Wang, *Energy & Environmental Science*, 2014, **7**, 1966-1973.
13. H. Yao, L. Ye, H. Zhang, S. Li, S. Zhang and J. Hou, *Chemical Reviews*, 2016, **116**, 7397-7457.
14. R. Narasimhan Arunagirinathan, P. Gopikrishna, D. Das and P. K. Iyer, *ACS Applied Electronic Materials*, 2019, **1**, 600-607.
15. B. Carsten, F. He, H. J. Son, T. Xu and L. Yu, *Chemical Reviews*, 2011, **111**, 1493-1528.
16. I. Osaka, M. Saito, H. Mori, T. Koganezawa and K. Takimiya, *Advanced Materials*, 2012, **24**, 425-430.
17. W. Li, L. Yang, J. R. Tumbleston, L. Yan, H. Ade and W. You, *Advanced Materials*, 2014, **26**, 4456-4462.
18. Z. Li, D. Yang, X. Zhao, T. Zhang, J. Zhang and X. Yang, *Advanced Functional Materials*, 2018, **28**, 1705257.
19. C. Liu, K. Wang, X. Hu, Y. Yang, C.-H. Hsu, W. Zhang, S. Xiao, X. Gong and Y. Cao, *ACS Appl. Mater. Interfaces*, 2013, **5**, 12163-12167.
20. S. F. Hoefler, T. Rath, N. Pastukhova, E. Pavlica, D. Scheunemann, S. Wilken, B. Kunert, R. Resel, M. Hobisch, S. Xiao, G. Bratina and G. Trimmel, *Journal of Materials Chemistry A*, 2018, **6**, 9506-9516.

21. H. Kang, M. A. Uddin, C. Lee, K.-H. Kim, T. L. Nguyen, W. Lee, Y. Li, C. Wang, H. Y. Woo and B. J. Kim, *Journal of the American Chemical Society*, 2015, **137**, 2359-2365.

22. L. Lu, T. Zheng, T. Xu, D. Zhao and L. Yu, *Chemistry of Materials*, 2015, **27**, 537-543.

23. J. A. Bartelt, J. D. Douglas, W. R. Mateker, A. E. Labban, C. J. Tassone, M. F. Toney, J. M. J. Fréchet, P. M. Beaujuge and M. D. McGehee, *Advanced Energy Materials*, 2014, **4**, 1301733.

24. R. C. Hiorns, R. de Bettignies, J. Leroy, S. Bailly, M. Firon, C. Sentein, A. Khoukh, H. Preud'homme and C. Dagron-Lartigau, *Advanced Functional Materials*, 2006, **16**, 2263-2273.

25. M. P. Nikiforov, B. Lai, W. Chen, S. Chen, R. D. Schaller, J. Strzalka, J. Maser and S. B. Darling, *Energy & Environmental Science*, 2013, **6**, 1513-1520.

26. J. Gao, W. Wang, S. Zhang, S. Xiao, C. Zhan, M. Yang, X. Lu and W. You, *Journal of Materials Chemistry A*, 2018, **6**, 179-188.

27. S. M. Lee, K. H. Park, S. Jung, H. Park and C. Yang, *Nature Communications*, 2018, **9**, 1867.

28. M. R. Raj, M. Kim, H. I. Kim, G.-Y. Lee, C. W. Park and T. Park, *Journal of Materials Chemistry A*, 2017, **5**, 3330-3335.

29. R. C. Coffin, J. Peet, J. Rogers and G. C. Bazan, *Nature Chemistry*, 2009, **1**, 657-661.

30. R. Hoogenboom and U. S. Schubert, *Macromolecular Rapid Communications*, 2007, **28**, 368-386.

31. T. Razzaq and C. O. Kappe, *ChemSusChem*, 2008, **1**, 123-132.

32. L. Huo, S. Zhang, X. Guo, F. Xu, Y. Li and J. Hou, *Angewandte Chemie International Edition*, 2011, **50**, 9697-9702.

33. B. J. Tremolet de Villers, K. A. O'Hara, D. P. Ostrowski, P. H. Biddle, S. E. Shaheen, M. L. Chabinyc, D. C. Olson and N. Kopidakis, *Chemistry of Materials*, 2016, **28**, 876-884.

34. T. Vangerven, P. Verstappen, J. Drijkoningen, W. Dierckx, S. Himmelberger, A. Salleo, D. Vanderzande, W. Maes and J. V. Manca, *Chemistry of Materials*, 2015, **27**, 3726-3732.

CHAPTER 3

Efficient Trap Passivation of $MAPbI_3$ via Multifunctional Anchoring for Stable Perovskite Solar Cells

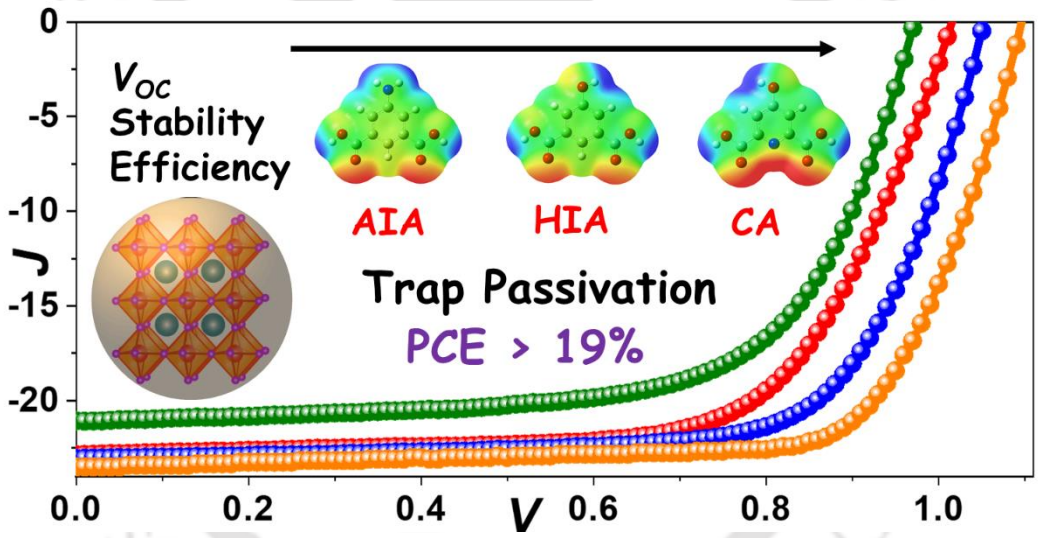

Manuscript: Rabindranath Garai, Mohammad Adil Afroz, Ritesh Kant Gupta, Parameswar Krishnan Iyer, "Efficient Trap Passivation of $MAPbI_3$ via Multifunctional Anchoring for High-Performance and Stable Perovskite Solar Cells." *Adv. Sustainable Syst.* 2020, **4**, 2000078.

[This page was intentionally left blank]

Abstract

Chemical passivation of ionic defects in perovskite materials (especially in the surface and grain boundaries) is an effective strategy to reduce charge recombination in perovskite solar cells (PSCs). Despite reports of several additives being used for this purpose, it is very difficult to elucidate the specific role for these additives since the passivation mechanisms of different functional groups remains very unclear. Herein, the effect of molecules possessing multiple functional anchoring has been systematically investigated. Three different multifunctional molecules namely 5-aminoisophthalic acid (AIA), 5-hydroxyisophthalic acid (HIA) and chelidamic acid (CA) have been strategically chosen. These molecules not only take part in crystallization process but also passivate the trap states effectively. CA molecule shows superior passivation capacity among all with its better dipolar electron density distribution. The passivated films revealed considerably improved morphology with lesser pin holes and larger grains in comparison to the pristine film. These passivation molecules, having multiple functional groups, have been shown to simultaneously passivate various kinds of defects of perovskite very efficiently. CA passivated p–i–n structured photovoltaic devices have demonstrated the best PCE of 19.06% with an impressive V_{OC} of 1.097 V, an improvement of 125 mV over the device without passivation that showed a PCE of 13.60% and V_{OC} of 0.972 V. Moreover, the devices reveal notable thermal and ambient stability in comparison to the pristine devices due to lower defect states and reduced ion migration.

3.1 Overview

Metal halide hybrid perovskite solar cells (PSCs) have received tremendous attention as one of the fastest emerging photovoltaic technologies because it largely drives down the cost of renewable and clean solar energy conversion with a very high power conversion efficiencies (PCEs).[1, 2] For the solution-processed PSCs, high PCEs of >25% has been achieved[3] because of the outstanding optoelectronic properties of the perovskite materials such as superior absorption coefficient, tunable band gap, better charge carrier lifetime, etc.[4-6] Yet, inconsistencies in the control of the perovskite crystallization process often leads to poor morphology in terms of grain size, film coverage, grain boundaries, and trap sites which deteriorates the device stability and efficiency.[7, 8] To obtain improved perovskite films several strategies have been developed such as solvent or composition engineering,[9, 10] vapor-assisted solution deposition,[11] hot-casting of substrate,[12] vacuum flash treatment,[13] anti-solvent treatment,[14-16] and thermal or solvent annealing.[17, 18] However, such films often exhibit considerable defects (e.g., under coordinated and non-coordinated ions produced due to ion migration[19]) at grain boundaries and surface which can act as traps and leads to non-radiative recombination and reduces the charge carrier life time as well as the device performances. Simultaneously, corrosive moisture and oxygen can easily interact with the defects and degrade the perovskite.[8, 20-22]

The most convenient technique to efficiently passivate these defects is to introduce additives with various functional groups (e.g., –OH, $–NH_2$, -COOH, –CN, etc.). These groups not only effectively neutralize or reduce the activity of ions (e.g., Pb^{2+}, MA^+ and I^-) present in the perovskites through different interactions such as, Lewis acid-base interactions, hydrogen bonding, etc. but also can take part in the perovskite nucleation and control the grain growth. For example, citric acid and other carboxylic acids were used to control the crystal growth of perovskite that also bound tightly with the under coordinated, Lewis acidic lead ions and successfully passivated the defects.[23-25] Electron-rich pyridine and thiophene molecules donate electron density to the under coordinated lead ion to form Lewis adducts and reduced the defects which enhanced the photoluminescence (PL) as well as device performances.[26-28] Furthermore, some Lewis base type electronic trap states on perovskite surface can be reduced by accepting electrons, using molecules such as phenyl-C61-butyric acid methyl ester ($PC_{61}BM$), ITIC, etc.[29, 30] Again, these surface defects can also be annihilated by ionic molecules such as 4-(1H-imidazol-3-ium-3-yl) butane-1-sulfonate (IMS), phenethylammonium.[31, 32] However, some strong Lewis base like 4-tert-

butyl pyridine (TBP), can corrode the perovskite active layer and affect the stability and reproducibility of the solar cells.[28, 33] Although several techniques have been applied for the defect passivation of perovskite at the surface and grain boundaries, it remains very crucial and challenging to select suitable additives which can effectively control perovskite crystallization and simultaneously passivate diverse type of electronic defects successfully.

Herein, the impact of multiple functional groups, present in a single passivation moiety (such as benzene ring) has been systematically studied. It is observed that a small passivation molecule with multiple functional groups can easily spread over the grain boundaries of hybrid perovskites, and effectively passivate the defects. Three different multifunctional molecules namely 5-aminoisophthalic acid (AIA), 5-hydroxyisophthalic acid (HIA) and chelidamic acid (CA) have been used strategically in this study. All the additives were independently studied by adding them separately in the perovskite precursor at various concentrations to find out the effect of passivation on the device performance. Through this study, we reveal a unique set of passivation molecules having multiple functional groups that can simultaneously passivate multiple kinds of defects (cationic and anionic) in perovskites very efficiently. As a proof of concept, we demonstrate that CA passivated p-i-n solar cell exhibits a prominent enhancement in the open circuit voltage (V_{OC}) of 125 mV compared to the pristine device (from 0.972 V for pristine to 1.097 V for CA modified device). Simultaneously, the device demonstrates remarkable thermal and ambient stability in comparison to the pristine device because of lower defect states and reduced ion migration.

3.2 Results and Discussions

To figure out the effect of multifunctional passivation, three molecules with multiple anchor groups- AIA (two –COOH group and one $–NH_2$ group), HIA (two –COOH group and one –OH group) and CA (two –COOH group, one –OH group and one Pyridinyl N donor group) have been strategically chosen in this work (**Figure 3.1a**). Previously reported mono or bi-functional additives often showed labile passivation effect due to weak anchoring and poor structural stability.[34] On the contrary, these multifunctional passivation molecules can strongly interact with Pb^{2+}, MA^{+}, labile I^{-} ions and perform dual task of controlling perovskite crystallization as well as passivation of grain boundaries (GBs) in perovskite films. After perovskite film formation, these molecules generally distribute

along the GBs to interact with the under co-ordinated Pb^{2+} ions and can cover the volatile components to reduce deep traps.

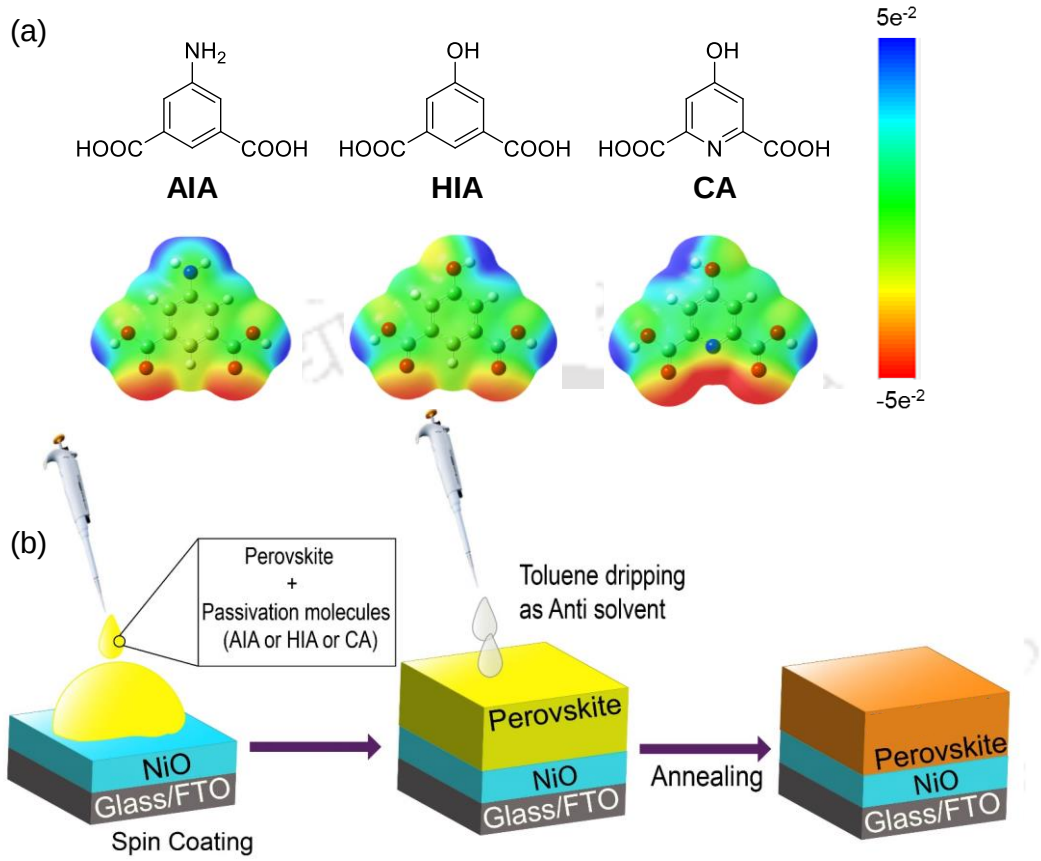

Figure 3.1 (a) Molecular structures and calculated ESP profiles of AIA, HIA and CA. (b) Schematic illustration of perovskite thin film passivation process.

Figure 3.1a represents the electrostatic potential (ESP) profiles calculated from DFT.[35, 36] Initially AIA and HIA were compared to observe the effect of $–NH_2$ and –OH groups in the presence of two –COOH groups, where $–NH_2$ and –OH groups are expected to interact with negatively charged defects and two –COOH groups are expected to combine with positively charged defects. Both the molecules exhibit almost comparable local electron density in the carbonyl groups of the –COOH functionality which can interact with positively charged defects for the two molecules similarly. However, the –OH functionality shows much higher local positive charge density in ESP profile compared to the $–NH_2$ functionality. Hence the passivation ability towards negatively charged defects is expected to be better for HIA than AIA. In order to further enhance the passivation ability, CA molecule with an additional N donor was introduced. The CA molecule has much improved local electron density in the region of N donor and carboxylic acid group in comparison to

the AIA and HIA molecules. Therefore, the passivation ability of CA should be higher than HIA. Passivation of the perovskite layer was attained by dissolving these multi-functional molecules into the perovskite precursor followed by spin coating through anti solvent dripping technique (**Figure 3.1b**). FTIR spectroscopy was carried out with the passivated perovskite films to verify the presence of passivation molecules in the film and their interaction with perovskite (**Figure 3.2 a-c**). For all the molecules there is a considerable shift of $\upsilon_{C=O}$ band which is due to the interaction between the lone pairs of carboxylic acid group and Pb ions of perovskite.[37] A schematic of probable interaction between additives and perovskite is presented in **Figure 3.2d**. The carbonyl group and Pyridinyl N group (for CA only) in the additives can interact strongly with the MA^+ ion, under coordinated Pb^{+2} and I^- vacancy. Whereas the $-NH_2$ and -OH group can be interacted with the halide ion and MA^+ vacancy.

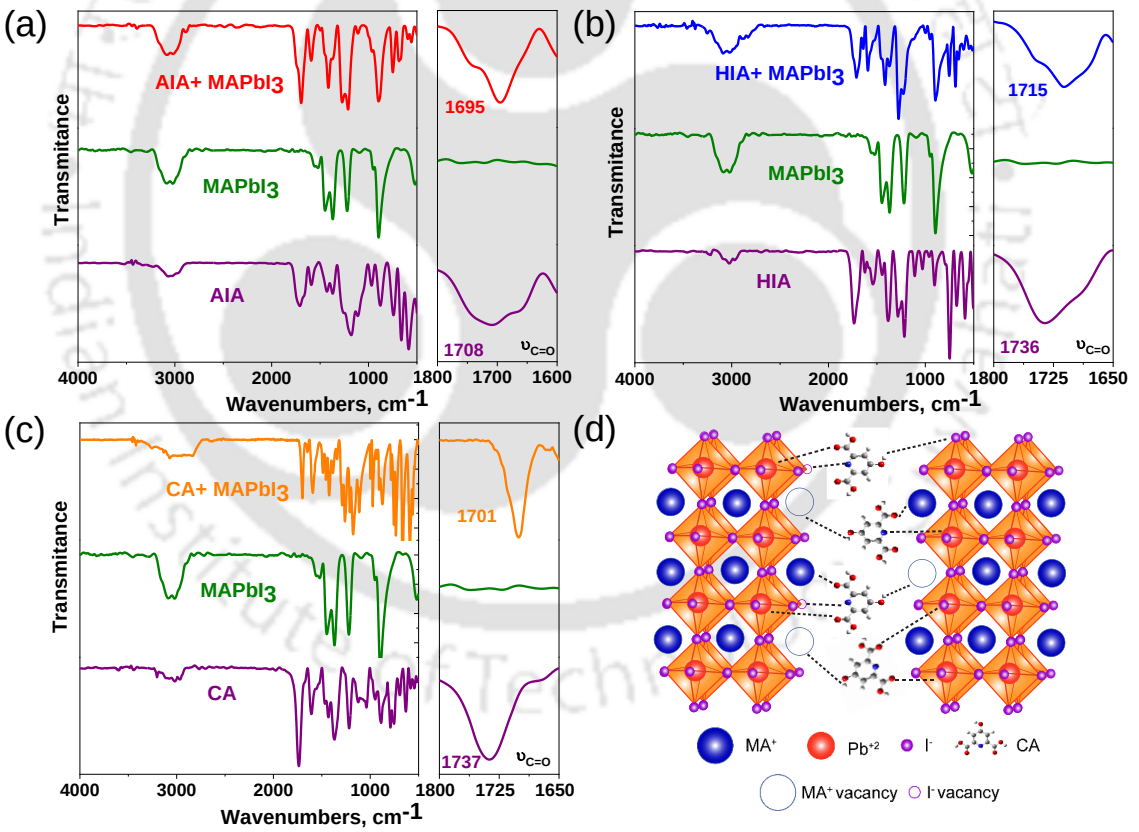

Figure 3.2 FTIR spectra of additive, $MAPbI_3$ film, and $MAPbI_3$ + additive film with its magnification spectra. (a) AIA, (b) HIA, (c) CA, and (d) Schematic illustration of the interaction between CA and perovskite.

The passivation effect of all the additives should extensively boost V_{OC} of the PSCs because of their improved carrier concentration under illumination which can increase the quasi-fermi level splitting.[38] To investigate this, p-i-n structured PSCs were fabricated with the

device architecture of FTO/NiOx/Perovskite/$PC_{61}BM$/Rhodamine 101/Ag. All the passivation molecules were added in different concentrations in the perovskite precursor solution to acquire optimized device results (**Table 3.1**).

Table 3.1: Photovoltaic parameters of PSCs with different concentration of additives.

Device	J_{SC}, mA-cm^{-2}	V_{OC}, mV	FF, %	PCE, Best (Average), %
Pristine	**21.06**	**972.1**	**66.4**	**13.60 (12.58 ± 0.64) [a]**
2.5 mg AIA	22.58	1011.7	65.4	14.93 (14.14 ± 0.94) [b]
5.0 mg AIA	**22.85**	**1015.8**	**67.6**	**15.70 (14.81 ± 0.66) [a]**
7.5 mg AIA	20.83	1025.6	67.5	14.44 (13.54 ± 0.58) [b]
2.5 mg HIA	21.94	1050.7	68.7	15.84 (15.20 ± 0.47) [b]
5.0 mg HIA	**23.05**	**1052.6**	**71.2**	**17.29 (16.62 ± 0.45) [a]**
7.5 mg HIA	20.79	1057.5	69.3	15.24 (14.77 ± 0.32) [b]
2.5 mg CA	22.88	1077.2	70.7	17.43 (16.68 ± 0.43) [b]
5.0 mg CA	**23.49**	**1096.5**	**74.0**	**19.06 (18.17 ± 0.36) [a]**
7.5 mg CA	20.85	1108.3	72.4	16.73 (15.83 ± 0.65) [b]

[a]Average of 40 devices, [a]Average of 10 devices

Best device results were obtained at 5 mg-ml^{-1} concentration for each additive. However, the device performance begins to decline at the higher concentration of the additives (over 5 mg-ml^{-1}) due to reduction of short-circuit current density (J_{SC}) that may be because of higher extent of insulating layer around GBs which deteriorates charge transport. The current density–voltage (*J*–*V*) curves for the champion devices are shown in **Figure 3.3a**. The pristine device reveals a PCE of 13.6 % with Voc of 972.1 mV, fill factor (FF) of 66.4 % and J_{SC} of 21.05 mA-cm^{-2}. PSCs after AIA passivation exhibits a better PCE of 15.70 % with an improved V_{OC} of 1015.8 mV and J_{SC} of 22.85 mA-cm^{-2} in comparison to the pristine device, whereas, HIA and CA doping leads to a superior device performance with better V_{OC} and FF because of enhanced passivation efficiency. Among all the three dopants, CA displayed highest solar cell performance of 19.06 % PCE with a V_{OC} of 1096.5 mV, FF of 74.0 % and J_{SC} of 23.49 mA-cm^{-2} for the champion cell.

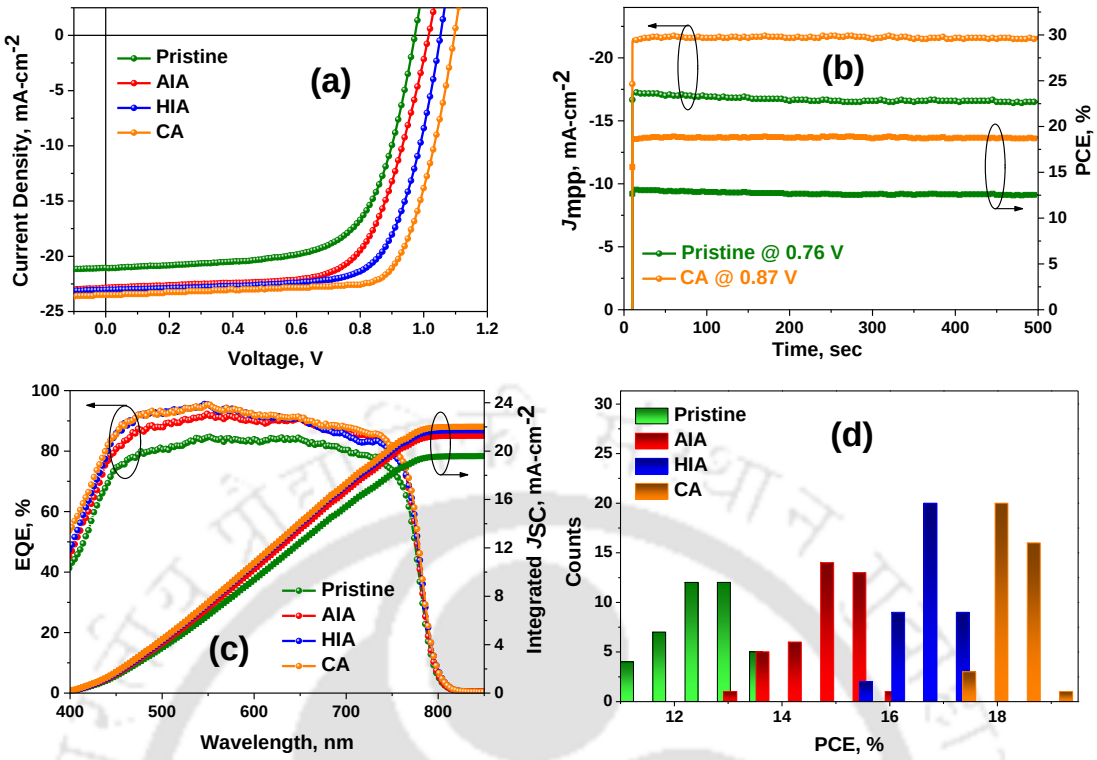

Figure 3.3 (a) *J-V* curves, (b) Steady state current measured at maximum power point for pristine and CA passivated PSCs, (c) EQE curves of devices without and with additives, and (d) Histogram of 40 cells.

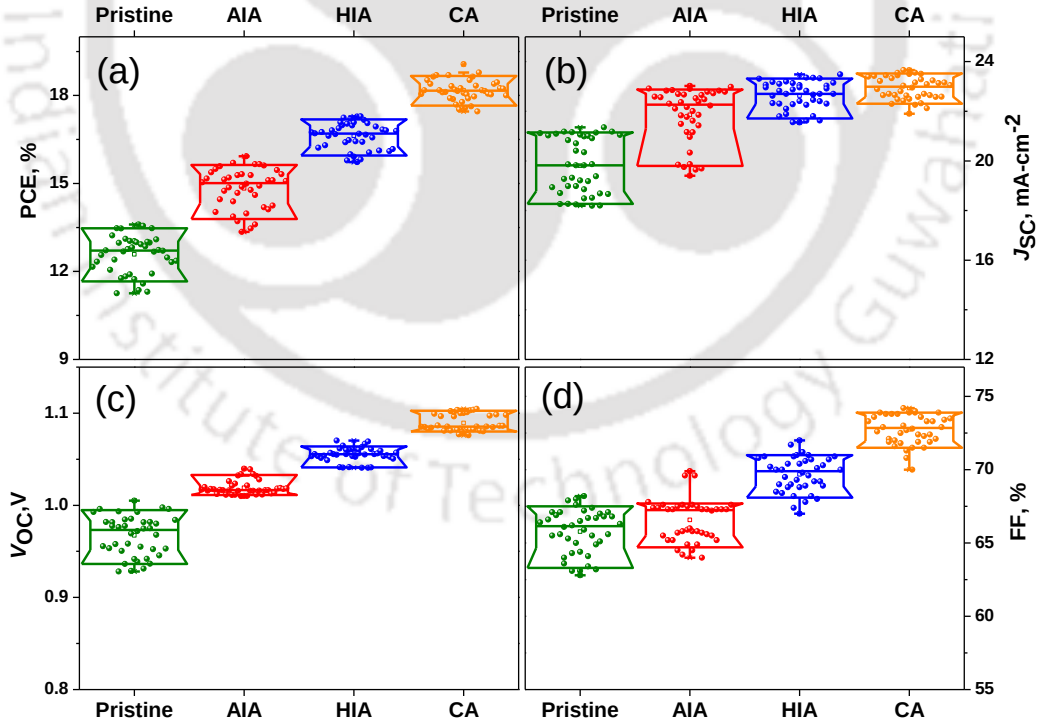

Figure 3.4 Box chart of 40 devices each of Pristine, AIA, HIA and CA: (a) PCE, (b) *Jsc*, (c) *Voc* and (d) fill factor.

To further confirm the results, the steady-state current measurements were carried out for the pristine and CA passivated devices at their maximum power point. As shown in **Figure**

3.3b, the device with CA exhibits a stable PCE of 18.70% up to 500 sec whereas a gradual decrement of PCE from 13.11% to 12.54% is observed for the pristine device. External quantum efficiency (EQE) spectra of the PSCs illustrate an intense photo response within spectral range of 400−800 nm (**Figure 3.3c**). The significant increment of the J_{SC} values from pristine to passivated device attained from the *J-V* measurements are well-reflected in their EQE spectra. The integrated *J*sc values calculated from EQE spectra are 22.02, 21.72, 21.28 and 19.59 mA-cm^{-2} for CA, HIA, AIA and pristine respectively. For the best concentration (5mg-mL^{-1}), 40 individual cells were prepared for all the additives and the resulted histogram and box chart reveals outstanding reproducibility (**Figure 3.3d, Figure 3.4**). CA passivation shows better average PCE and narrow distribution (18.17 ± 0.36%) than HIA & AIA passivation and the pristine devices (16.62 ± 0.45%, 14.81 ± 0.66% and 12.58 ± 0.64%, respectively).

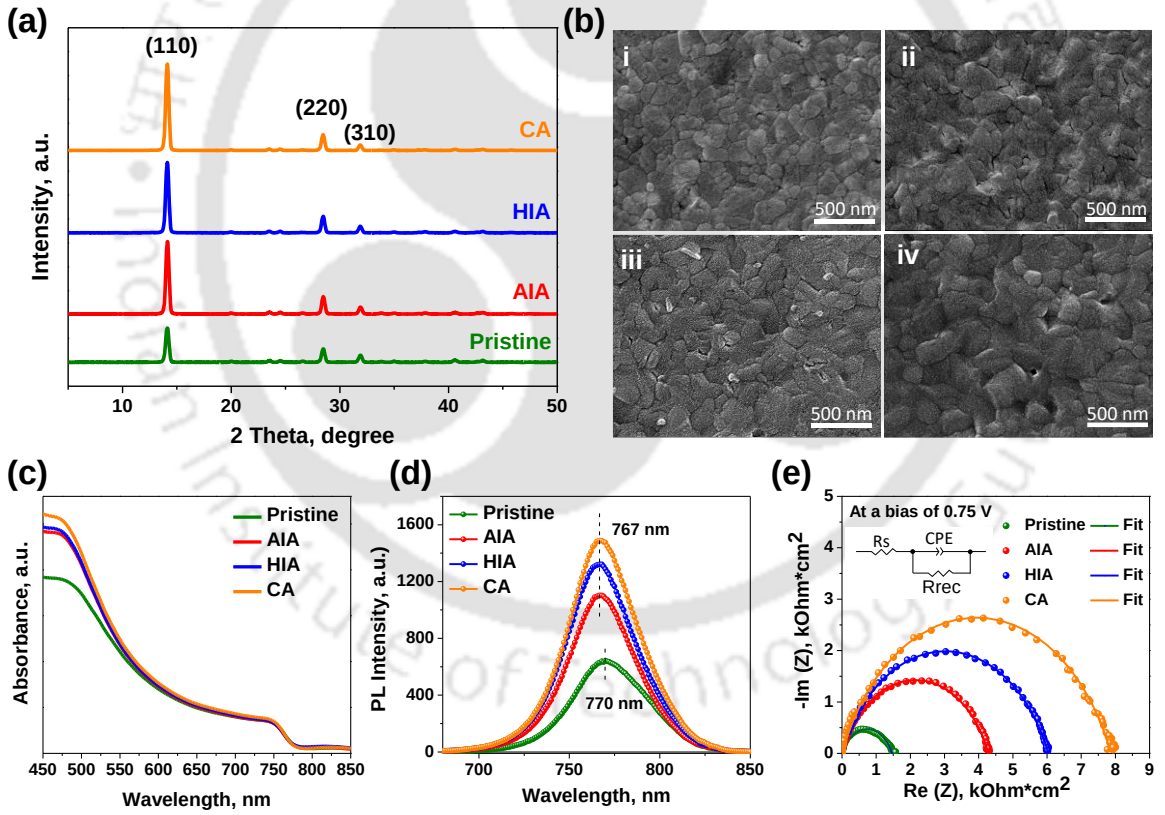

Figure 3.5 (a) XRD patterns of perovskite films with and without additives. (b) Surface FESEM images of perovskite films (i) Pristine, (ii) AIA, (iii) HIA and (iv) CA. (c) UV−vis absorption spectra of the films. (d) Steady state PL spectra of perovskite films with and without additives. (e) Nyquist plots of the pristine and passivated devices.

XRD measurements were performed to determine the effect of passivation molecules on the perovskite film. The XRD patterns of the pristine and passivated films are shown in

Figure 3.5a. All the films show peaks at 2θ value of 14.08˚, 28.44˚, 31.88˚ that correspond to (1 1 0), (2 2 0), & (3 1 0) diffraction planes of $MAPbI_3$. But the peak intensity gradually increases from pristine to CA passivation which indicates the crystallinity of the perovskite films improves simultaneously. FESEM analysis was then carried out to evaluate the effect of additive addition on the perovskite film formation. A high-quality perovskite film with bigger grains, reduced pinholes and lower grain boundaries is a crucial factor for highly efficient PSCs. **Figure 3.5b** shows the FESEM images of pristine and different additive passivated perovskite films. It is observed that the perovskite grains size increases from pristine to passivated films. Grain boundaries and pin holes are also reduced after passivation. CA passivation displays highest grain size among all with lower pin holes and grain boundaries. These results can be easily co-related with the XRD. To further comprehend the effect of passivation on absorption, the perovskite thin films were characterized via UV-vis spectroscopy. As demonstrated in **Figure 3.5c**, the absorbance improves in the passivation films in the range from 400 nm to 550 nm and the CA passivated film exhibited highest light harvesting property among all. This enhancement in absorption might be attributed to better film formation in presence of additives which leads to high quality perovskite films with lesser pinholes and minimum grain boundaries as confirmed from FESEM images. For a better understanding of charge-carrier dynamics in perovskite films before and after passivation, the PL spectroscopy was recorded for these films (**Figure 3.5d**). The PL intensity largely improves after passivation with AIA, HIA and CA which is attributed to the reduced non-radiative recombination resulting from lower defect density. Additionally, a minor blue shift in the PL peak was observed from 770 nm to 767 nm that indicates sufficient trap passivation.[38]

To further estimate the charge transfer kinetics including internal resistance, capacitance and trap state, electrochemical impedance spectroscopy (EIS) experiment was performed. The measurement was carried out under dark condition at different bias voltage (0.65-0.90 V) in the frequency range of 0.1 Hz – 1 MHz. The Nyquist plots at 0.75 V are presented in **Figure 3.5e**. The Nyquist data was fitted using an equivalent circuit diagram as illustrated in the inset of Figure 4e. The higher value of recombination resistance (*R*rec) for CA passivated device suggests lesser recombination which leads to better charge transport and higher V_{OC}. Moreover, the plot of *R*rec as a function of applied voltage and its linear fitting curves are presented in **Figure 3.6a** that shows an inverse proportionality of *R*rec with applied voltage. The result indicates efficient blocking of recombination in modified

devices confirming the defect passivation ability of additives. **Figure 3.6b** presents the semi-log plot of the capacitance (C) vs bias voltage. It can be noted that the value of C is lower for the passivated devices compared to the pristine one. Considering C as a measure of stored charge carriers at the trap state, its density of state (DOS) can be calculated from the data plotted in **Figure 3.6b**.[39] The DOS values obtained are shown in **Figure 3.6c** and reveals that the passivated devices have lower traps compared to the pristine device at all bias voltages. Hence the lower traps with narrow distribution in passivated films provided lower recombination and better charge transport in the devices which resulted in improved J_{SC} and V_{OC} values. The result obtained from this study regarding the passivation capability of the additives can be well correlated with ESP profile obtained from the DFT. Passivation effect was further confirmed from capacitance versus frequency curve. As shown in **Figure 3.6d** the PSC fabricated with additives have lower capacitance in the lower frequency region indicating the reduction of traps in the order of Pristine<AIA<HIA<CA.

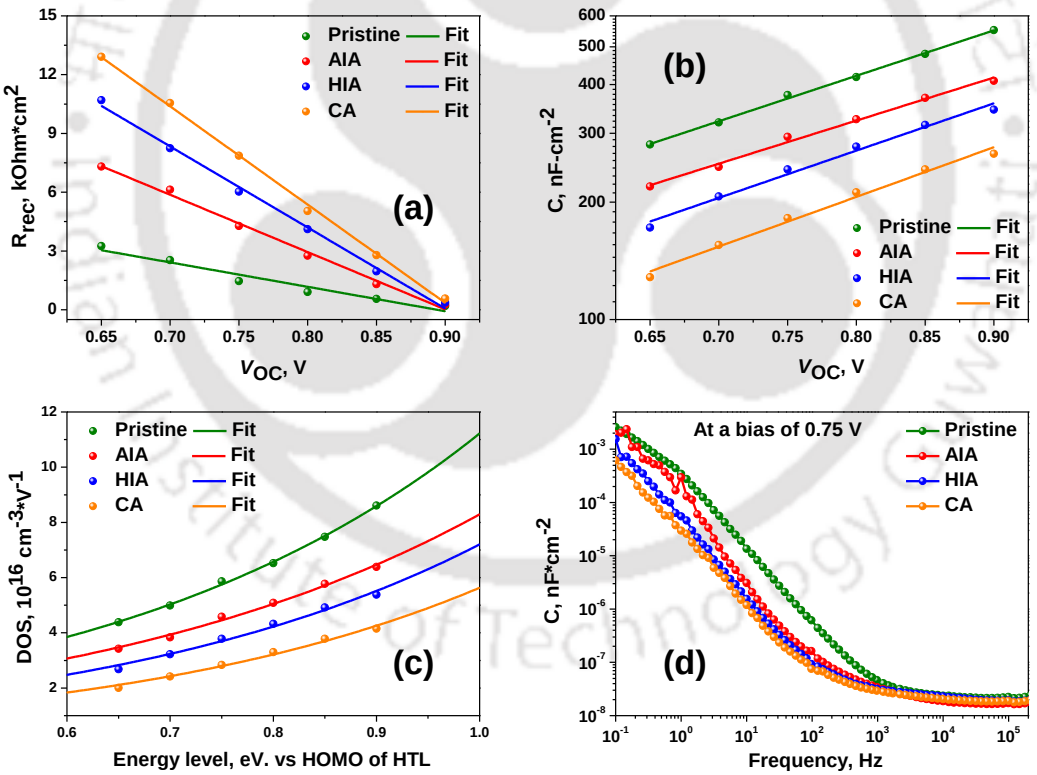

Figure 3.6 (a) Recombination resistance (*R*rec) and (b) Capacitance (C) with variable bias, (c) trap density of states (DOS) versus electron energy level for control and TA based devices. (d) Variation of C with frequency.

Discussions in the above sections reveal that the multifunctional CA molecules not only enhance the trap passivation, but also significantly inhibit the penetration of moisture (water molecules) into the perovskite layer. These passivation molecules can effectively

distribute along the grain boundaries and produce a hydrophobic coating over it, which repels the water molecules. Moreover, the interaction between passivation molecules and the ions in perovskite can lead to reduced ion migration and improve the long-term stability. Therefore, long term ambient stability of the pristine and CA passivated devices was studied by measuring the PCE variation of the two devices stored in a relative humidity of 30-40 % at room temperature without encapsulation. **Figure 3.7a** shows that the pristine device exhibits a gradual decrease in efficiency over time and degraded almost 90 % within seven-fifty hours, whereas the CA passivated device retains up to 80 % of its initial PCE after thousand hours. The long-term ambient stability of the respective films was also characterized through XRD study. The degradation of perovskite leads to formation of a new peak in XRD at 12.7°, which is the characteristic peak of PbI_2 phase. **Figure 3.7b** displays the XRD patterns of pristine and CA passivated films with aging time. The peak for PbI_2 phase starts to generate for the pristine film after five hundred hours only but the film with CA passivation reveals no degradation even after thousand hours.

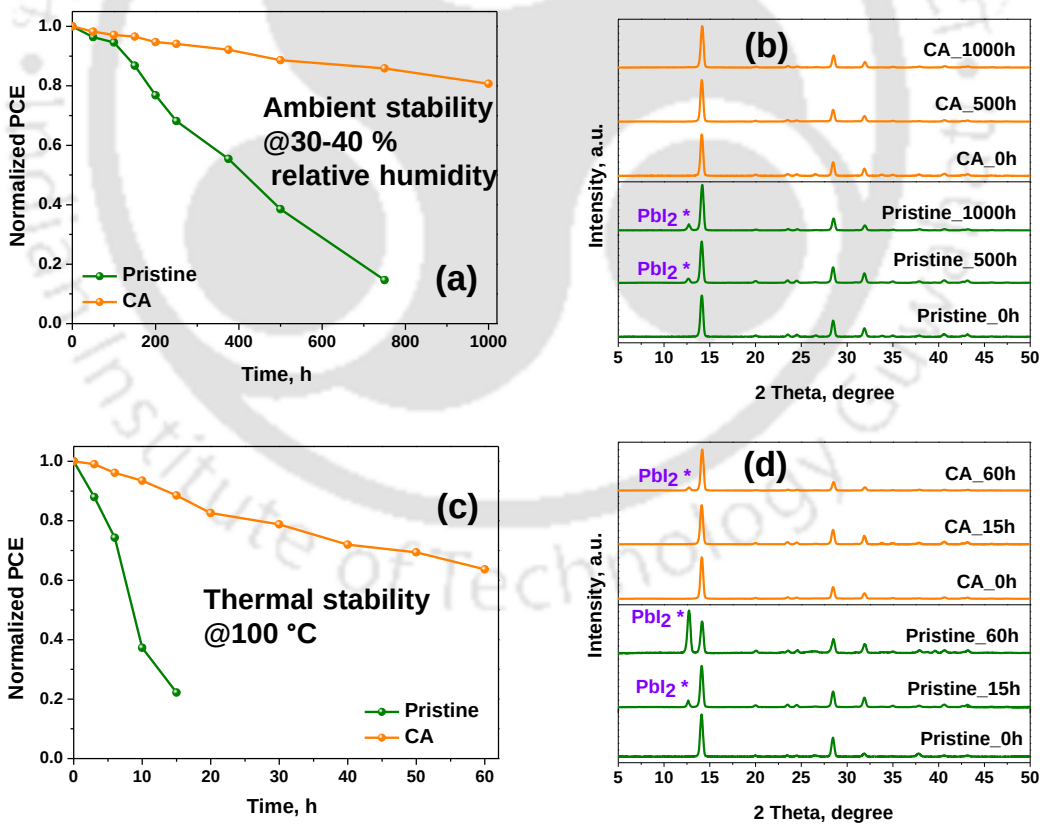

Figure 3.7 (a) Normalized PCE of Pristine and CA passivated devices stored at room temperature in a relative humidity of 30-40 %. (b) XRD patterns of perovskite films stored in a relative humidity of 30-40 %. (c) Normalized efficiency of Pristine and CA passivated device heated at 100 °C inside the glovebox. (d) XRD patterns of perovskite films heated at 100 °C for different time.

The thermal stability test for the devices was also performed inside the glove box by heating them on a hotplate at 100° C (**Figure 3.7c**). The pristine device exhibits a fast degradation and its efficiency reduced up to 22 % of its initial value within twenty hours, but the CA passivated device can retain 63 % PCE after sixty hours. Again, the results of the thermal stability study were further proved by XRD patterns of the corresponding films after different time of heating (**Figure 3.7d**). For the pristine film, the peak for PbI_2 starts to arise after 15 hours of heating and the film was almost degraded after 60 hours. However, the CA passivated film exhibits a small peak for PbI_2 after 60 hour of heating which signifies a slight degradation of the film. Therefore, it is obvious that the CA can effectively inhibit the decomposition of $MAPbI_3$ by improving trap passivation and reducing ion migration.

3.3 Conclusions

In summary, a highly efficient and facile trap passivation strategy of perovskite films has been demonstrated by fine tuning the functional groups in multifunctional molecules via modulating the electron density distribution. Due to the improved polar electron density distribution, CA molecule efficiently interacted with perovskite to regulate the crystallization kinetics and passivate the defects, which led to the formation of superior perovskite film with lesser trap states and improved photoelectric properties. The trap passivation capacity has been carefully investigated with PL and EIS measurements. As a consequence, CA passivated p–i–n structures have demonstrated a high PCE of 19.06% with an impressive V_{OC} of 1.097 V. Moreover, the ambient and thermal stability of the device also improved drastically with CA passivation confirming the retention of morphology in humid condition and elevated temperature. This effective and facile strategy of multifunctional anchoring-based trap passivation will provide very useful insights for improving perovskite film morphology, photoelectric quality and environmental stability in optoelectronic device applications.

3.4 Experimental Section

Materials: FTO glass substrates (13 Ω sq^{-1}), PbI_2 (99.8%), all solvents like DMF (anhydrous, 99.8%), DMDO (anhydrous, 99.8%), Toluene (anhydrous, 99.8%), Chlorobenzene were purchased from Sigma-Aldrich. MAI was purchased from Greatcell solar. Nickel nitrate hexahydrate ($Ni(NO_3)_2 \cdot 6H_2O$) was purchased from TCI. All other chemicals were used as received.

Preparation of NiO_x Film: NiO_x precursor solution was prepared by dissolving 1M Nickel nitrate hexahydrate and 1M Ethylenediamine in 1ml Ethylene Glycol. Then the NiO_x layer was coated as hole transporting layer on the cleaned FTO. The cleaning process was started with detergent and followed by deionized water, acetone, and isopropyl alcohol for 15 min for each solvent, then dried and treated with UV-ozone for half an hour. NiO_x precursor solution was spin coated onto the FTO substrates @3000 rpm for 40 sec. Afterward the substrates were post-annealed at 300 °C for 60 min in ambient air.

Device Fabrication: The $MAPbI_3$ precursor solution was prepared in a glovebox by dissolving MAI and PbI_2 (1:1 ratio) in a mixed solvent of gamma-Butyrolactone and DMSO (7:3, v/v) where the concentration of Pb^{2+} was 1.26. The solution was heated overnight and filtered with the 0.45 μm filter prior to spin coating. For the modified device different concentration of additives (AIA, HIA and CA) were added to the precursor solution. The filtered precursor solution was spin coated on the NiO_x coated FTO in a two-step spin coating process i.e. 750 rpm for 20 sec and 4000 rpm for 60 sec. In the second step 160 μL anhydrous Toluene was dripped after 20 sec as anti-solvent and after that the substrates were annealed @80° C for 10 min. Above the perovskite layer 12 mg/ml PCBM solution was coated @1200 rpm as ETL and again annealed @80° C for 5 min. After that a thin layer of Rhodamine 101 inner salt (0.5 mg-ml^{-1} in IPA) was spin coated @4000 rpm. Finally, Ag was thermally deposited by using a shadow mask to yield an active area of 0.12 cm^2.

Device Characterization: The perovskite films were characterized by UV-vis absorption spectroscopy (Perkin Elmer Lambda-35), IR spectroscopy (LabRam HR). The XRD patterns of the samples were recorded using a Rigaku Micromax-007HF diffractometer equipped with Cu Kα1 irradiation (λ = 1.54184 Å). The morphology of the samples was investigated by scanning electron microscopy (SEM, JEOL) and AFM (Oxford, Cypher). The current density−voltage (*J*−*V*) characteristic curves were measured using a Keithley 2400 source meter under argon atmosphere by illuminating the device with a solar simulator (AM 1.5G, 100 mW cm^{-2}, Oriel Sol 3A solar simulator, Newport). The incident photon-to-current efficiency (IPCE) was obtained by using an Oriel IQE-200 instrument under ambient condition. Electrochemical measurements were performed with a CH Instruments 760D.

References

1. Y. Zhao and K. Zhu, *Chem. Soc. Rev.*, 2016, **45**, 655-689.
2. C.-H. Chiang, M. K. Nazeeruddin, M. Grätzel and C.-G. Wu, *Energy Environ. Sci.*, 2017, **10**, 808-817.
3. National Renewable Energy Laboratory, Best research-cell efficiencies chart, https://www.nrel.gov/pv/assets/pdfs/best-research-cell-efficiencies.20200104.pdf, (accessed 24.04.2021).
4. A. Kojima, K. Teshima, Y. Shirai and T. Miyasaka, *J. Am. Chem. Soc.*, 2009, **131**, 6050-6051.
5. W. Nie, H. Tsai, R. Asadpour, J.-C. Blancon, A. J. Neukirch, G. Gupta, J. J. Crochet, M. Chhowalla, S. Tretiak, M. A. Alam, H.-L. Wang and A. D. Mohite, *Science*, 2015, **347**, 522.
6. S. D. Stranks, G. E. Eperon, G. Grancini, C. Menelaou, M. J. P. Alcocer, T. Leijtens, L. M. Herz, A. Petrozza and H. J. Snaith, *Science*, 2013, **342**, 341-344.
7. C. C. Boyd, R. Cheacharoen, T. Leijtens and M. D. McGehee, *Chem. Rev.*, 2019, **119**, 3418-3451.
8. Y. Shao, Y. Fang, T. Li, Q. Wang, Q. Dong, Y. Deng, Y. Yuan, H. Wei, M. Wang, A. Gruverman, J. Shield and J. Huang, *Energy Environ. Sci.*, 2016, **9**, 1752-1759.
9. N. J. Jeon, J. H. Noh, Y. C. Kim, W. S. Yang, S. Ryu and S. I. Seok, *Nat. Mater.*, 2014, **13**, 897-903.
10. N. J. Jeon, J. H. Noh, W. S. Yang, Y. C. Kim, S. Ryu, J. Seo and S. I. Seok, *Nature*, 2015, **517**, 476-480.
11. Q. Chen, H. Zhou, Z. Hong, S. Luo, H.-S. Duan, H.-H. Wang, Y. Liu, G. Li and Y. Yang, *J. Am. Chem. Soc.*, 2014, **136**, 622-625.
12. M. A. Afroz, R. K. Gupta, R. Garai, M. Hossain, S. P. Tripathi and P. K. Iyer, *Org. Electron.*, 2019, **74**, 172-178.
13. X. Li, D. Bi, C. Yi, J.-D. Décoppet, J. Luo, S. M. Zakeeruddin, A. Hagfeldt and M. Grätzel, *Science*, 2016, **353**, 58-62.
14. S. Paek, P. Schouwink, E. N. Athanasopoulou, K. T. Cho, G. Grancini, Y. Lee, Y. Zhang, F. Stellacci, M. K. Nazeeruddin and P. Gao, *Chem. Mater.*, 2017, **29**, 3490-3498.
15. M. Xiao, F. Huang, W. Huang, Y. Dkhissi, Y. Zhu, J. Etheridge, A. Gray-Weale, U. Bach, Y.-B. Cheng and L. Spiccia, *Angew. Chem., Int. Ed.*, 2014, **53**, 9898-9903.
16. R. Wang, J. Xue, L. Meng, J.-W. Lee, Z. Zhao, P. Sun, L. Cai, T. Huang, Z. Wang, Z.-K. Wang, Y. Duan, J. L. Yang, S. Tan, Y. Yuan, Y. Huang and Y. Yang, *Joule*, 2019, **3**, 1464-1477.
17. Z. Xiao, Q. Dong, C. Bi, Y. Shao, Y. Yuan and J. Huang, *Adv. Mater.*, 2014, **26**, 6503-6509.
18. F. X. Xie, D. Zhang, H. Su, X. Ren, K. S. Wong, M. Grätzel and W. C. H. Choy, *ACS Nano*, 2015, **9**, 639-646.

19. B. Chen, M. Yang, X. Zheng, C. Wu, W. Li, Y. Yan, J. Bisquert, G. Garcia-Belmonte, K. Zhu and S. Priya, *J. Phys. Chem. Lett.*, 2015, **6**, 4693-4700.

20. M. Kim, S. G. Motti, R. Sorrentino and A. Petrozza, *Energy Environ. Sci.*, 2018, **11**, 2609-2619.

21. H. Back, G. Kim, J. Kim, J. Kong, T. K. Kim, H. Kang, H. Kim, J. Lee, S. Lee and K. Lee, *Energy Environ. Sci.*, 2016, **9**, 1258-1263.

22. J. Kim, A. Ho-Baillie and S. Huang, *Solar RRL*, 2019, **3**, 1800302.

23. Y. Guo, W. Sato, K. Shoyama, H. Halim, Y. Itabashi, R. Shang and E. Nakamura, *J. Am. Chem. Soc.*, 2017, **139**, 9598-9604.

24. X. Hou, S. Huang, W. Ou-Yang, L. Pan, Z. Sun and X. Chen, *ACS Appl. Mater. Interfaces*, 2017, **9**, 35200-35208.

25. M. Adil Afroz, N. Ghimire, K. M. Reza, B. Bahrami, R. S. Bobba, A. Gurung, A. H. Chowdhury, P. K. Iyer and Q. Qiao, *ACS Appl. Energy Mater.*, 2020, **3**, 2432-2439.

26. N. K. Noel, A. Abate, S. D. Stranks, E. S. Parrott, V. M. Burlakov, A. Goriely and H. J. Snaith, *ACS Nano*, 2014, **8**, 9815-9821.

27. R. Fu, Y. Zhao, Q. Li, W. Zhou, D. Yu and Q. Zhao, *Chem. Commun.*, 2017, **53**, 1829-1831.

28. Y. Yue, N. Salim, Y. Wu, X. Yang, A. Islam, W. Chen, J. Liu, E. Bi, F. Xie, M. Cai and L. Han, *Adv. Mater.*, 2016, **28**, 10738-10743.

29. F. Zhang, D. Bi, N. Pellet, C. Xiao, Z. Li, J. J. Berry, S. M. Zakeeruddin, K. Zhu and M. Grätzel, *Energy Environ. Sci.*, 2018, **11**, 3480-3490.

30. J. Jiang, Z. Jin, J. Lei, Q. Wang, X. Zhang, J. Zhang, F. Gao and S. Liu, *J. Mater. Chem. A*, 2017, **5**, 9514-9522.

31. W. Zhou, D. Li, Z. Xiao, Z. Wen, M. Zhang, W. Hu, X. Wu, M. Wang, W.-H. Zhang, Y. Lu, S. Yang and S. Yang, *Adv. Funct. Mater.*, 2019, **29**, 1901026.

32. D. S. Lee, J. S. Yun, J. Kim, A. M. Soufiani, S. Chen, Y. Cho, X. Deng, J. Seidel, S. Lim, S. Huang and A. W. Y. Ho-Baillie, *ACS Energy Letters*, 2018, **3**, 647-654.

33. W. Li, H. Dong, L. Wang, N. Li, X. Guo, J. Li and Y. Qiu, *J. Mater. Chem. A*, 2014, **2**, 13587-13592.

34. D. W. deQuilettes, S. Koch, S. Burke, R. K. Paranji, A. J. Shropshire, M. E. Ziffer and D. S. Ginger, *ACS Energy Letters*, 2016, **1**, 438-444.

35. D. Xin, S. Tie, R. Yuan, X. Zheng, J. Zhu and W.-H. Zhang, *ACS Appl. Mater. Interfaces*, 2019, **11**, 44233-44240.

36. T. Wu, Y. Wang, X. Li, Y. Wu, X. Meng, D. Cui, X. Yang and L. Han, *Adv. Energy Mater.*, 2019, **9**, 1803766.

37. J. Zhang, Z. Hu, L. Huang, G. Yue, J. Liu, X. Lu, Z. Hu, M. Shang, L. Han and Y. Zhu, *Chem. Commun.*, 2015, **51**, 7047-7050.

38. S. Yang, J. Dai, Z. Yu, Y. Shao, Y. Zhou, X. Xiao, X. C. Zeng and J. Huang, *J. Am. Chem. Soc.*, 2019, **141**, 5781-5787.

39. L. Guan, N. Jiao and Y. Guo, *J. Phys. Chem. C*, 2019, **123**, 14223-14228.

[This page was intentionally left blank]

CHAPTER 4

Conjugated Polyelectrolyte Passivated Stable Perovskite Solar Cells for Efficiency Beyond 20%

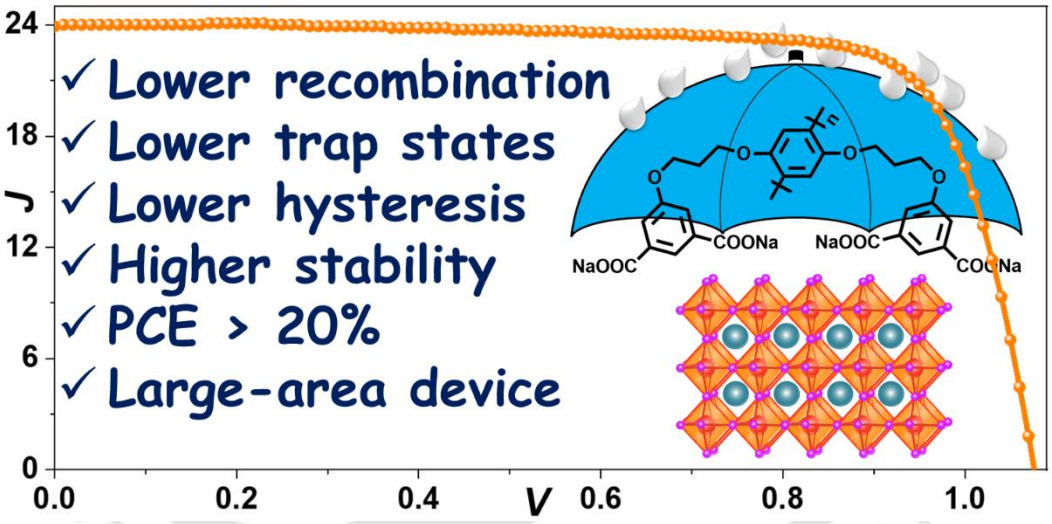

Manuscript: Rabindranath Garai, Ritesh Kant Gupta, Arvin Sain Tanwar, Maimur Hossain, Parameswar Krishnan Iyer, "Conjugated Poly-electrolyte Passivated Stable Perovskite Solar Cells for Efficiency Beyond 20%." *Chem. Mater.*, 2021, **33**, 5709–5717.

[This page was intentionally left blank]

Abstract

Developing large-scale perovskite solar cells (PSCs) requires high-quality defect-free perovskite films with improved surface coverage. One of the most convenient ways to achieve this is through the incorporation of appropriate passivation molecules in the perovskite films. Herein, the effect of a novel conjugated polyelectrolyte, PHIA, is investigated for perovskite passivation by comprehensive analysis of perovskite film and devices. The PHIA polymer significantly diminishes the trap states in perovskite films and the passivated device permits lesser recombination, very low accumulation of charges at the interface and lowers the traps which facilitated superior charge transport. As a result, high power conversion efficiency (PCE) of 20.17% has been achieved for PHIA modified device. Additionally, this passivation approach effectively enhanced the long-term device stability by improving the hydrophobicity of the perovskite layer. Further, large area device (2 cm^2) has also been fabricated to demonstrate the expediency of this approach for future commercialization.

4.1 Overview

In recent times, metal halide hybrid perovskites have witnessed immense focus for optoelectronic applications due to high absorption coefficient, long diffusion lengths for charge carriers and bandgap tunability.[1-3] In 2009, perovskite materials were first used for photovoltaic applications and from then onwards extensive research and rapid efforts have improved the power conversion efficiencies (PCEs) of perovskite solar cells (PSCs) to >25%.[4] However, several non-radiative recombination centres and defect states at the grain boundaries (GBs) and the surface of the perovskite layer can often limit the PCE, leading to poor device stability.[5-7] This hinders the scalable fabrication of PSCs as it requires high-quality, defect-free perovskite films.

The most effective technique to obtain defect-free, superior quality film with good surface coverage is the incorporation of suitable passivation additives in the perovskite layer which can reduce the trap states, minimize hysteresis and enhance device stability.[8, 9] Several small molecular additives, having numerous functional groups (such as -COOH, -NH_2, -OH, -SH, etc.), have been used for passivation that diminish the trap states and control crystallization process of the perovskite as well.[10-12] Again, ionic molecules can also suppress the electronic defect states in the perovskite and considerably enhance device efficiency and stability.[13-15] Conjugated and non-conjugated polymers have also been used as passivating agents and enhanced the device stability by significantly increasing the hydrophobicity of the perovskite layer.[16-21] Compared to small molecular additives, polymers have an advantage of preferential orientation along the GBs due to their bigger size. This results in crystalline, defect-free perovskite films with larger grain sizes, whereas the small molecules may be combined with the perovskite lattice.[7, 22] Although conjugated polyelectrolytes (CPEs) are being vastly used as a transport layer in PSCs,[23-25] its exploration as a passivation additives in perovskite devices is rather not common.

In this work, a novel poly(p-phenylene)-based conjugated polyelectrolyte PHIA has been designed and synthesized through free radical mechanism.[26] Further, the polymer is strategically functionalized on the side chains, such that it can be utilized in the efficient trap passivation of perovskites (**Figure 4.1**). This PHIA polymer facilitates multiple beneficial properties such as: (i) the anchoring groups can interact with various defects of perovskite and reduce the trap states, and (ii) the polymeric backbone induces hydrophobicity in the perovskite layer and enhances the ambient stability. Yet, PHIA

passivation reveals suppressed recombination and interfacial charge accumulation that enables enhanced carrier transport. This trap passivation strategy improves all the device parameters, i.e., short-circuit current density (J_{SC}), open-circuit voltage (V_{OC}) as well as fill factor (FF) and diminishes the hysteresis significantly. Therefore, the passivated device demonstrates a high PCE of 20.17% with an appreciable ambient stability. Lastly, large area devices have also been fabricated to determine the efficacy of this approach for commercial application.

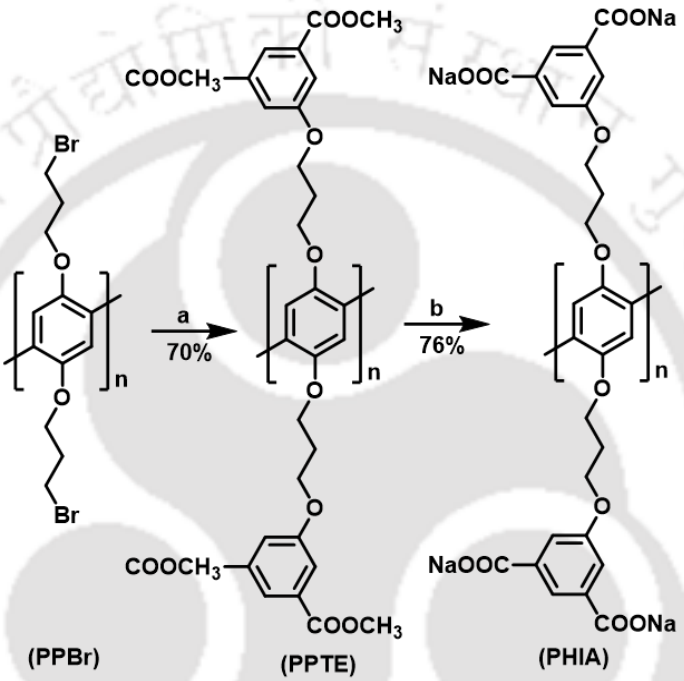

Figure 4.1 Synthesis of PHIA. (a) Dimethyl-5-hydroxyiso-phthalate, DMF, K_2CO_3, 80 °C, 24 h. (b) 30% NaOH, THF, 50 °C, 12 h.

4.2 Results and Discussions

The effect of conjugated polyelectrolyte PHIA, as an efficient additive for perovskite passivation, has been presented in this work. For the fabrication of the perovskite film, the precursor solution with and without PHIA was coated through well-known anti-solvent dripping technique and annealed for 10 minutes (**Figure 4.2a)**. **Figure 4.2b** illustrates the chemical structure of PHIA polymer which can passivate various defects of perovskite. The electrostatic potential (ESP) profile for the anionic counterpart was calculated from density functional theory (**Figure 4.2c**). ESP profile reveals that the anionic counterpart has a strong local electron density around the side chain carboxylate ions. This negatively charged part is expected to interact with the positively charged defects. It can be confirmed

from the Fourier transform infrared spectroscopy (FTIR) spectroscopy (**Figure 4.2d**), where the $\upsilon_{C=O}$ band of the carboxylate ion of PHIA experienced a considerable shift from 1705 to 1642 cm^{-1} indicating sufficient interaction between carboxylate ion and perovskite.[27]

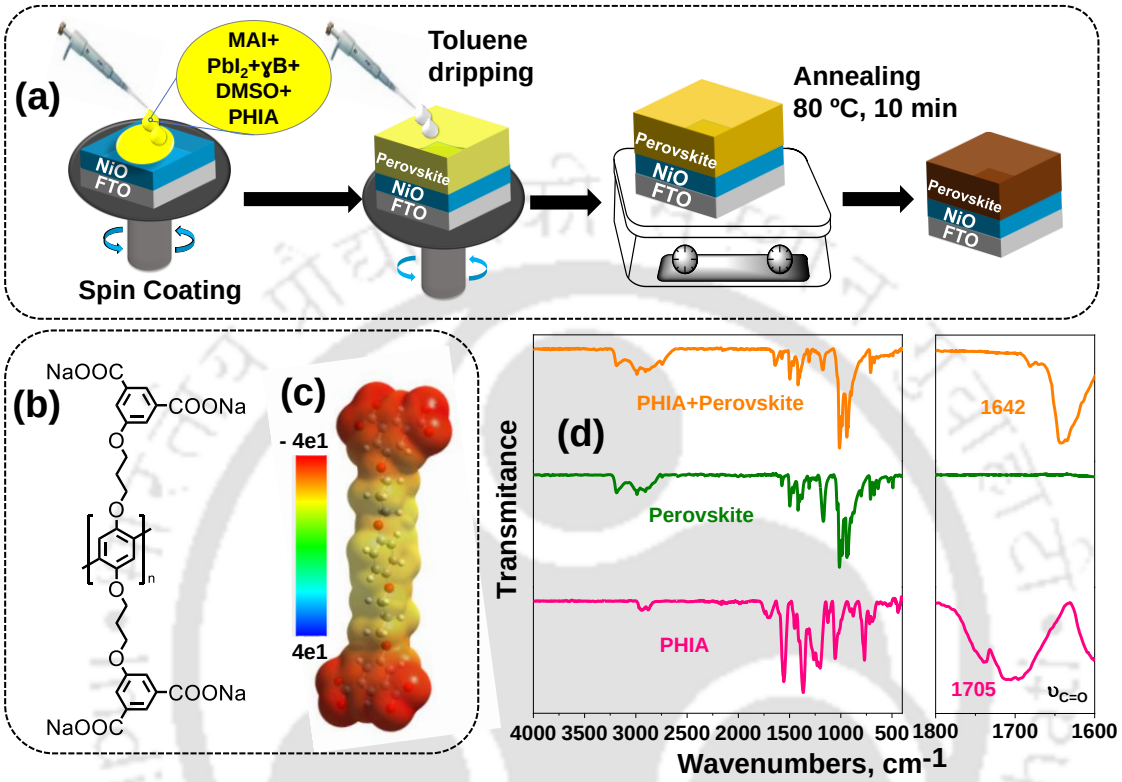

Figure 4.2 (a) Schematic representation of perovskite thin film coating process, (b) Molecular structure of PHIA, (c) ESP profile of anionic counterpart of the polymer, and (d) FTIR spectra of PHIA, $MAPbI_3$ film, and $MAPbI_3$ + PHIA film with its magnification spectra.

The UV-vis absorption spectra of perovskite thin-films with different concentrations of PHIA additive were carefully studied (**Figure 4.3a**). Initially, a considerable improvement in absorption spectra is observed with increasing PHIA concentration from 0 mg-mL^{-1} PHIA (pristine) to 0.50 mg-mL^{-1} PHIA (0.50_PHIA), whereas it weakens with higher PHIA concentration. All the films were coated with the same technique and exhibit similar thicknesses. Therefore, the increased absorption after PHIA passivation may be due to better quality perovskite film with higher crystallinity, which can enhance light harvesting properties. To check the effect of passivation on perovskite film crystallinity, X-ray diffraction (XRD) analysis was performed (**Figure 4.3b**). All the films demonstrate polycrystalline XRD peaks for $MAPbI_3$ perovskite at (110), (220), (310) and (224) lattice planes corresponding to a 2θ value of 14.12°, 28.48°, 31.90° and 40.64°, respectively. Interestingly, the peak intensities corresponding to (110), (220) and (310) lattice planes

gradually increase from pristine to 0.50_PHIA films and reduces thereafter (**Figure 4.3c**). This indicates that the film crystallinity initially improves up to 0.50 mg-mL^{-1} additive and reduces with further addition of PHIA. To further evaluate the passivation effect, film morphologies were recorded with field emission scanning electron microscope (FESEM). Compared to the pristine film, grain size gradually increases for passivated films up to certain concentrations of additive (**Figure 4.3d**). 0.50_PHIA reveals maximum grain size among all the films with least pinholes, more surface coverage and few grain boundaries which lead to reduction of surface trap states.

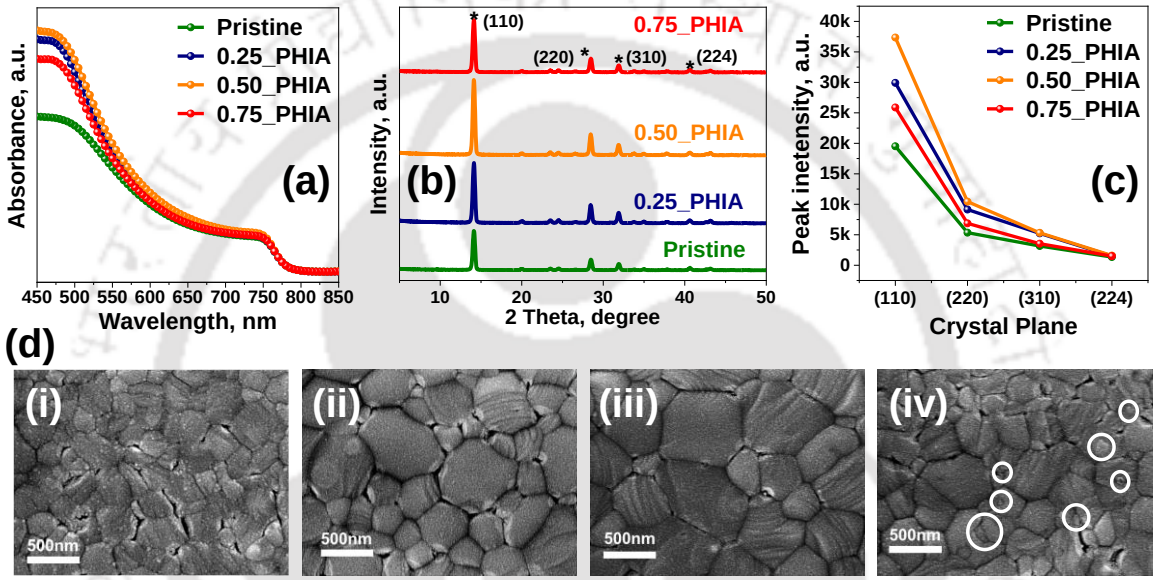

Figure 4.3 (a) UV–vis absorption spectra of the films without and with additive of varied concentration, (b) XRD patterns of perovskite films with various PHIA concentration. (c) XRD peak intensity of the (110), (220), (310), and (224) planes of perovskite films with varied concentrations of PHIA., and (d) Surface FESEM images of (i) Pristine, (ii) 0.25_PHIA, (iii) 0.50_PHIA & (iv) 0.75_PHIA perovskite films.

PHIA passivation leads to better quality perovskite films with lower trap states that would improve the PSC device performance. To investigate the passivation effect, p-i-n architecture, solar cell devices were fabricated with the device configuration of FTO/NiO_x/Perovskite layer/$PC_{61}BM$/Rhodamine 101/Ag (**Figure 4.4a**). The current density versus voltage (*J*–*V*) plot for pristine and various concentrations of PHIA passivated devices are presented in **Figure 4.4b** and the device parameters are summarized in **Table 4.1**. The pristine device discloses a PCE of 14.53% with J_{SC} of 21.01 mA-cm^{-2}, V_{OC} of 1006.2 mV and FF of 68.7%. With increasing PHIA quantity, all the device parameters improved up to 0.50 mg-mL^{-1} additive and reduces beyond this concentration, likely due to overcrowding of the additive at grain boundaries evidenced from the FESEM image (**Figure 4.3d, iv**).[12] The highest PCE of 20.17 % is achieved for the 0.5_PHIA

device with a J_{SC} of 23.92 mA-cm^{-2}, V_{OC} of 1076.2 mV and FF of 78.4%. **Figure 4.4c** displays the *J-V* curves measured for both forward (F) and reverse (R) directions. PHIA passivated device shows almost identical *J-V* curve in both the directions resulting in reduced hysteresis than the pristine. Hysteresis index (HI) is calculated using equation-4.1:[28]

$$HI = \frac{\mathrm{PCE}_F - \mathrm{PCE}_R}{\mathrm{PCE}_F} \qquad \text{Equation-4.1}$$

HI largely reduces from 9.8% to 3.3% after PHIA passivation due to reduced ion migration as the additive can strongly interact with the labile ions.

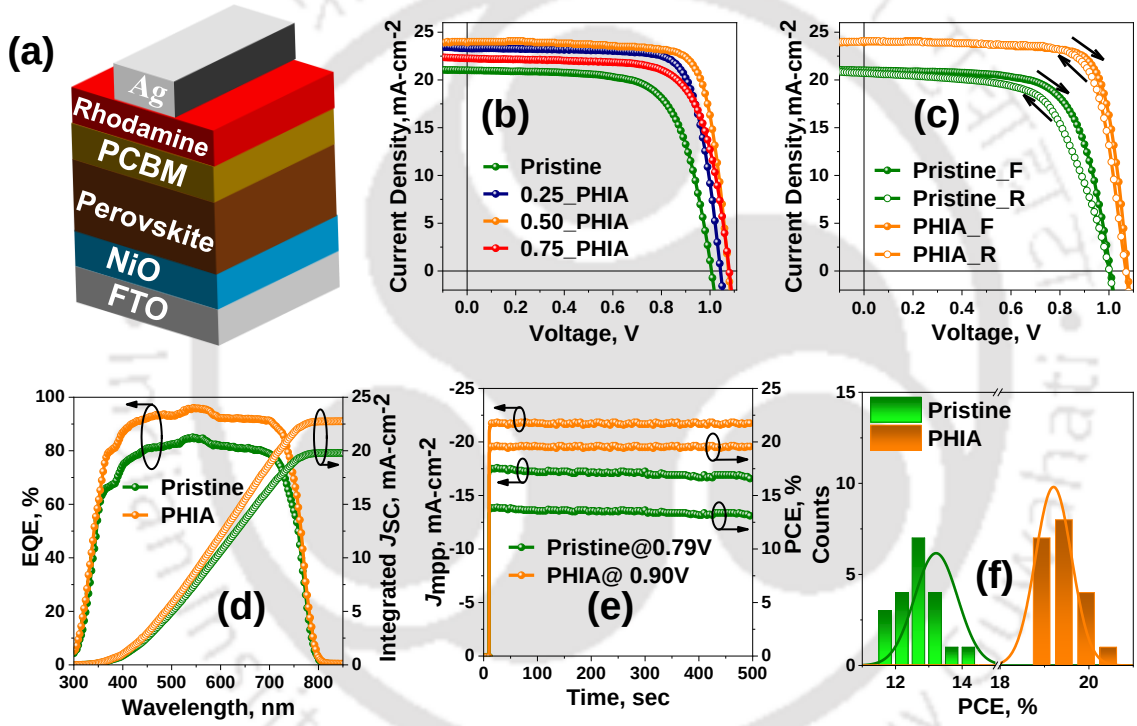

Figure 4.4 (a) Schematic illustration of device architecture, (b) *J–V* curves of the devices with various PHIA concentration, (c) *J–V* curves of pristine and PHIA passivated devices at different scan directions, (d) EQE curves of devices without and with PHIA additive, (e) Steady state current measured at maximum power point for pristine and PHIA passivated PSCs, and (f) Histogram of 20 cells of pristine and PHIA modified device.

External quantum efficiency (EQE) is also enhanced for the passivated device indicating better transport of the photogenerated charge carriers towards respective electrodes (**Figure 4.4d**). Integrated JSC values are in good agreement with the J_{SC} achieved from the *J-V* curve for both Pristine and PHIA modified devices. To validate the *J-V* results, steady-state measurements were conducted at maximum power point for both pristine and passivated devices (**Figure 4.4e**). PHIA passivated device demonstrates stable photo-response and a

PCE of 19.62% up to 500 sec while the PCE gradually declines for the device without PHIA.

Table 4.1: Photovoltaic parameters of PSCs with different concentration of additives.

Device	J_{SC}, mA-cm^{-2}	V_{OC}, mV	FF, %	PCE, Best (Average), %
Pristine	21.01	1006.2	68.7	14.53 (13.21±0.65) [a]
0.25_PHIA	23.31	1043.4	76.7	18.66 (17.58±0.53) [a]
0.50_PHIA	23.92	1076.2	78.4	20.17 (19.20±0.37) [a]
0.75_PHIA	22.26	1079.3	72.1	17.32 (16.28±0.61) [a]

[a]Average of 20 devices.

Furthermore, 0.5_PHIA device demonstrates significant reproducibility with an average PCE of 19.20±0.37% in comparison to the pristine device (PCE of 13.21±0.65%) as shown in the histogram plot (**Figure 4.4f**). The statistical data of 20 devices is displayed in the box chart with varied additive concentration confirms the reproducibility of all the device parameters (**Figure 4.5**).

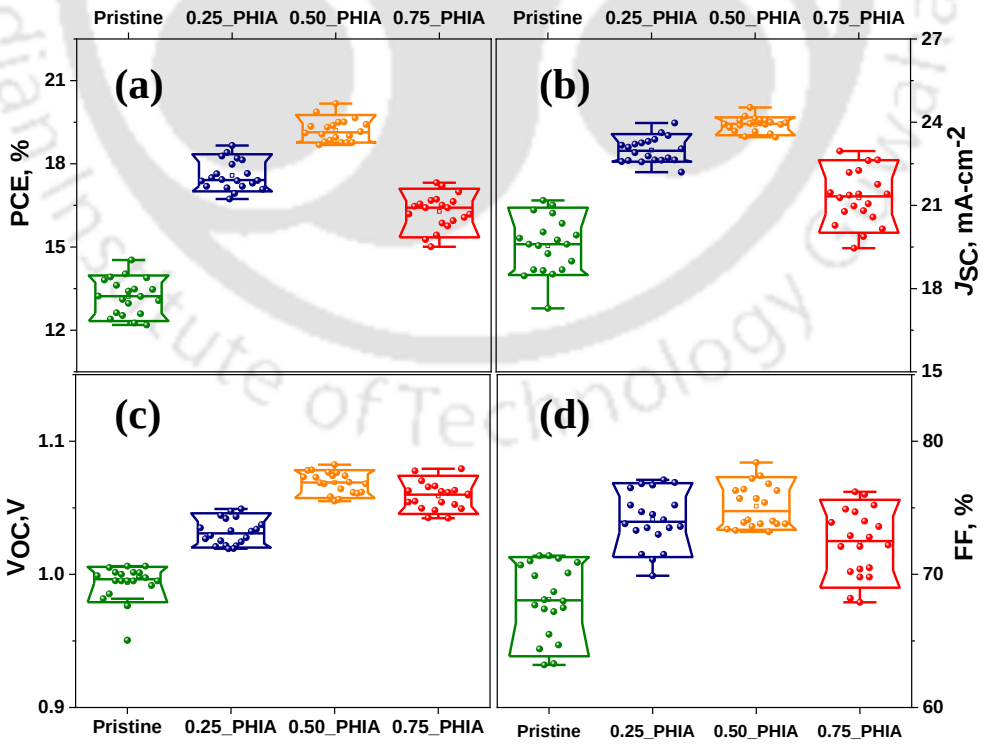

Figure 4.5 Box chart of pristine and different concentration of PHIA modified devices.

To investigate the trap passivation mechanism, several opto-electrical measurements were performed for the pristine and passivated films as well as devices. At first, Urbach energy (E_u) is determined from the absorption band edge of the perovskite films to study the trap states. E_u is associated with the defect states in the band edge region and can be calculated by using equation-4.2:[29]

$$\alpha = \alpha_0 \exp\left(\frac{E}{E_u}\right) \qquad \text{Equation-4.2}$$

where α is the absorption coefficient, α_0 is a constant and E (=hυ) is the energy of photon. **Figure 4.6a** discloses ln (α) versus photon energy plot. From the slope of this graph, E_u is estimated to be 53.8 meV for the pristine film, which decreases to 48.2 meV after passivation. This suggests that PHIA incorporation reduces the density of defect states and band edge energetic disorders. Hence, the passivation process results in lower trap assisted recombination, justifying appreciable V_{OC} improvement.

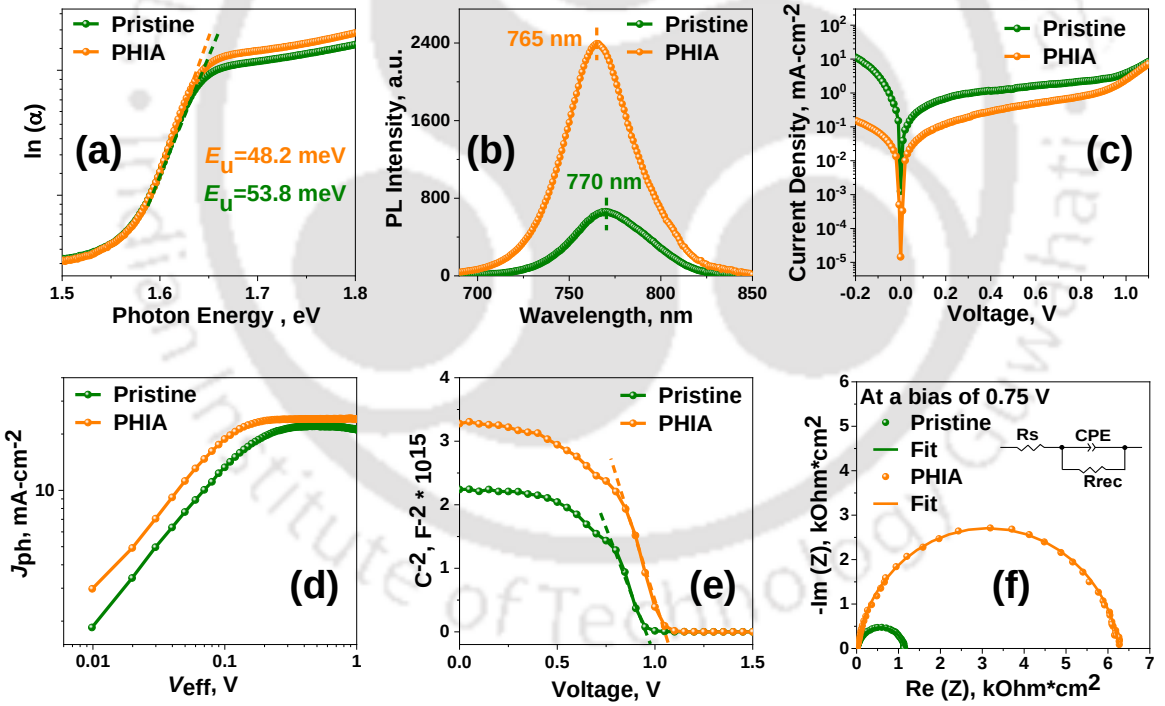

Figure 4.6 (a) Plot of ln(α) versus photon energy used to estimate Urbach energy, (b) Steady state PL spectra of perovskite films with and without additives, (c) Dark *J*–*V* characteristics of pristine and PHIA modified device, (d) J_{ph} versus V_{eff} characteristics with double-logarithmic axis for pristine and passivated device, (e) Mott−Schottky plots, and (f) Nyquist plots of the devices with and without PHIA.

This was proved by the steady-state photoluminescence (PL) measurement of the perovskite films (**Figure 4.6b**). PL intensity of the passivated film is increased by almost three folds in contrast to the pristine film due to the lesser non-radiative recombination

originating from lower defect density. Moreover, the pristine film showed a slight blue-shift from 770 to 765 nm after PHIA addition, signifying effective trap passivation.[12, 30] For obtaining more insights into the carrier recombination mechanism, dark $J-V$ measurements were carried out for the pristine and modified devices (**Figure 4.6c**). The reverse saturation current of the pristine device largely decreases after passivation signifying lower carrier recombination and better charge transport. **Figure 4.6d** demonstrates the dependency of photocurrent density (J_{ph}) on the effective voltage (V_{eff}) with and without PHIA passivation. Here $J_{ph} = J_{light} - J_{dark}$, where J_{light} & J_{dark} are the current densities under light and dark condition and $V_{eff} = V_0 - V$, where V is the applied bias and V_0 is the bias at which $J_{ph} = 0$.[31, 32] J_{ph} of the two devices linearly enhanced at low V_{eff} range (< 0.35 V) and gradually tends to a saturated photocurrent (J_{sat}) at higher V_{eff}. PHIA passivated device exhibits improved J_{sat} which leads to a higher generation rate (G_{max}). As G_{max} is the measure of the maximum number of photons absorbed, higher G_{max} of the passivated device indicates enhanced light absorption and harvesting property for the photoactive layer that is well supported by UV-vis absorption study. This justifies J_{SC} improvement of the passivated device in comparison to the pristine. On the other hand, at the lower V_{eff} range, there are large changes in J_{ph}-V_{eff} characteristics between the pristine and passivated device. Since J_{ph}/J_{sat} ratio at any V_{eff} is directly related to the carrier transport and efficiency of carrier collection, a higher ratio indicates better carrier transport as well as collection.[33] This ensures better FF and V_{OC} in the passivated device than the pristine. Again, the interfacial charge accumulation was studied through capacitance-voltage measurements from Mott-Schottky (MS) analysis (**Figure 4.6e**). Here the depletion layer capacitance (C) can be expressed as a function of the applied bias V as in equation-4.3: [34]

$$\frac{1}{C^2} = \frac{-2}{\varepsilon\varepsilon_0 q A^2 N}(V - V_{bi}) \qquad \text{Equation-4.3}$$

Where ε is the relative dielectric constant, ε_0 is the vacuum permittivity, A is the area of the device, N is residual charge density and V_{bi} is the built-in potential. Generally, V_{bi} can be estimated from the intercept of the X-axis of the straight line in the curve. PHIA passivated devices reveal higher V_{bi} of 1.05 V compared to the pristine device (0.96 V). This result justifies the V_{OC} increment for the passivated device. The improvement of V_{bi} in the PHIA modified device is due to lower trap assisted carrier recombination at the interface. The residual charge density was calculated from the slope of the linearly fitted M-S plot. The modified device displays a lower N value of 2.91×10^{16} cm^{-3} as compared to

the modified device (3.83×10^{16} cm^{-3}), indicating lower charge accumulation and recombination at the interface. Moreover, electrical impedance spectroscopy (EIS) measurements were performed to acquire an in-depth understanding of the carrier transport dynamics. **Figure 4.6f** shows the Nyquist plots of the pristine and passivated device at 0.75 V. By fitting the graphs, using an equivalent circuit presented in the inset of the Figure, recombination resistance (*R*rec) can be estimated. The *R*rec values increase with passivation reveals lower recombination and facilitates better charge transport.

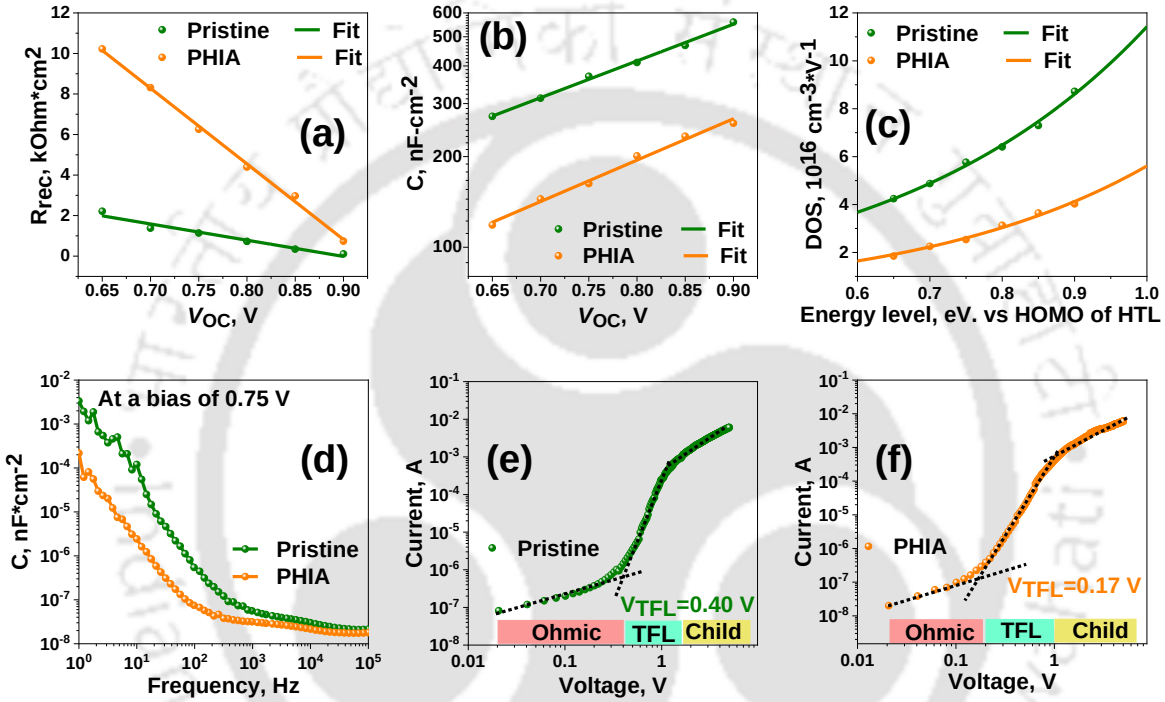

Figure 4.7 (a) *R*rec variation with different bias, (b) Variation of *C* with variable bias, c) Trap density of states (DOS) versus electron energy level, (d) Variation of *C* with frequency, and (e,f) Dark *J*–*V* characteristics from hole-only devices of pristine and PHIA modified device respectively.

For further analysis, EIS measurement at varied voltage was carried out. The linear fitted curve of *R*rec variation with applied voltage is shown in **Figure 4.7a**. For the pristine and passivated device, *R*rec displays an inverse relationship with applied voltage. However, the passivated device exhibits higher *R*rec at all applied voltages in comparison to the pristine, which specifies trap passivation restricts the carrier recombination effectively. This ensures better carrier transport towards respective electrodes and results in higher V_{OC} and J_{SC}. **Figure 4.7b** presents a linearly fitted semi-log curve of capacitance (*C*) versus applied voltage. It is observed that the value of *C* is lesser for the PHIA modified device in contrast to the pristine. '*C*' can be considered as the quantity of charge carrier accumulation at traps. Therefore, trap density of states (*t*-DOS) with applied voltage was estimated from '*C*'

versus applied voltage plot**.** As expected, the passivated device exhibits a lower *t*-DOS value and with narrower distribution than the pristine device in **Figure 4.7c**. This can be a possible reason for the reduced defect states of the passivated film as estimated from the E_u data in **Figure 4.6a**. These lower *t*-DOS values of the passivated device indicate smaller recombination along with improved carrier transport. The effect of passivation was further studied by C versus frequency plot (**Figure 4.7d**). Considering the trapping-detrapping process to be slow, the response for traps is expected to appear at low frequency range. For the passivated device *C* is lesser at low-frequency range which signifies considerable defect passivation. Furthermore, SCLC measurements were performed to evaluate the trap density (N_t) in the pristine and passivated devices (**Figure 4.7e, f**). The analysis was carried out with the hole-only devices having a configuration of FTO/NiO_x/Perovskite layer/MoO_3/Cu. The N_t was calculated from the trap-filled limited region with the following equation-4.4:[34]

$$N_t = \frac{2V_{TFL}\varepsilon\varepsilon_0}{qL^2} \qquad \text{Equation-4.4}$$

where V_{TFL} is the voltage onset in the trap-filled limited region, ε the relative dielectric constant, ε_0 is the vacuum permittivity, and L is the thickness. Pristine device exhibits a higher N_t of 9.7×10^{15} cm^{-3} in comparison to the passivated device (4.1×10^{15} cm^{-3}). Trap density largely reduces for the PHIA modified device indicates sufficient trap passivation.

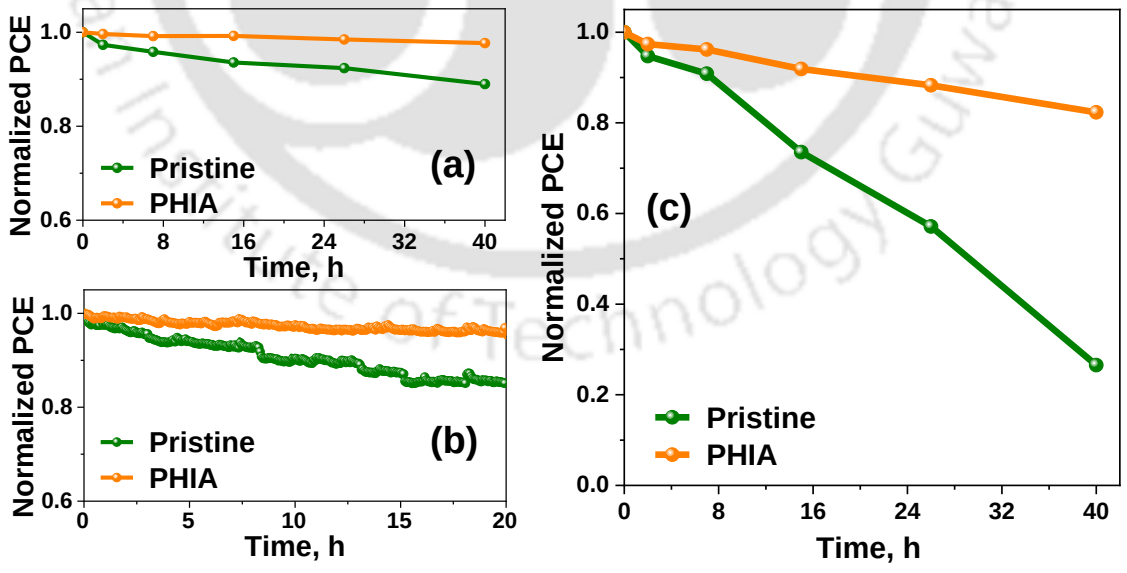

Figure 4.8 (a) Photostability study under continuous illumination, and (b) Operational stability study under continuous illumination and biasing condition through maximum power point tracking for the pristine and PHIA passivated device, and (c) Thermal stability test for the pristine and PHIA passivated device at 100° C.

PHIA polymer not only reduces the trap states in perovskite but noticeably enhances the stability of the device as well. At first, photo stability test of the pristine and PHIA modified devices were carried out by continuously illuminating both the devices under illumination. After 40 hours of light illumination, the pristine device retains ~90% of the initial PCE, whereas the PHIA passivated one reveals ~98% stability (**Figure 4.8a**). To further validate this result, the operational stability test was performed under illumination and biasing condition through maximum power point tracking (**Figure 4.8b**). After 20 hours of test run time, the pristine device retains ~84% of its initial PCE, while the passivated device maintains 95% of its original PCE. Thermal stability study was also conducted, where both the devices were heated at 100 °C. After 40 hours of heating, the passivated device retains ~82% of its original PCE whereas the pristine one degraded to ~26%. (**Figure 4.8c**). The reason for superior stability can be the minimized trap states as well as high quality perovskite film with larger grains and reduced grain boundaries.[30, 35]

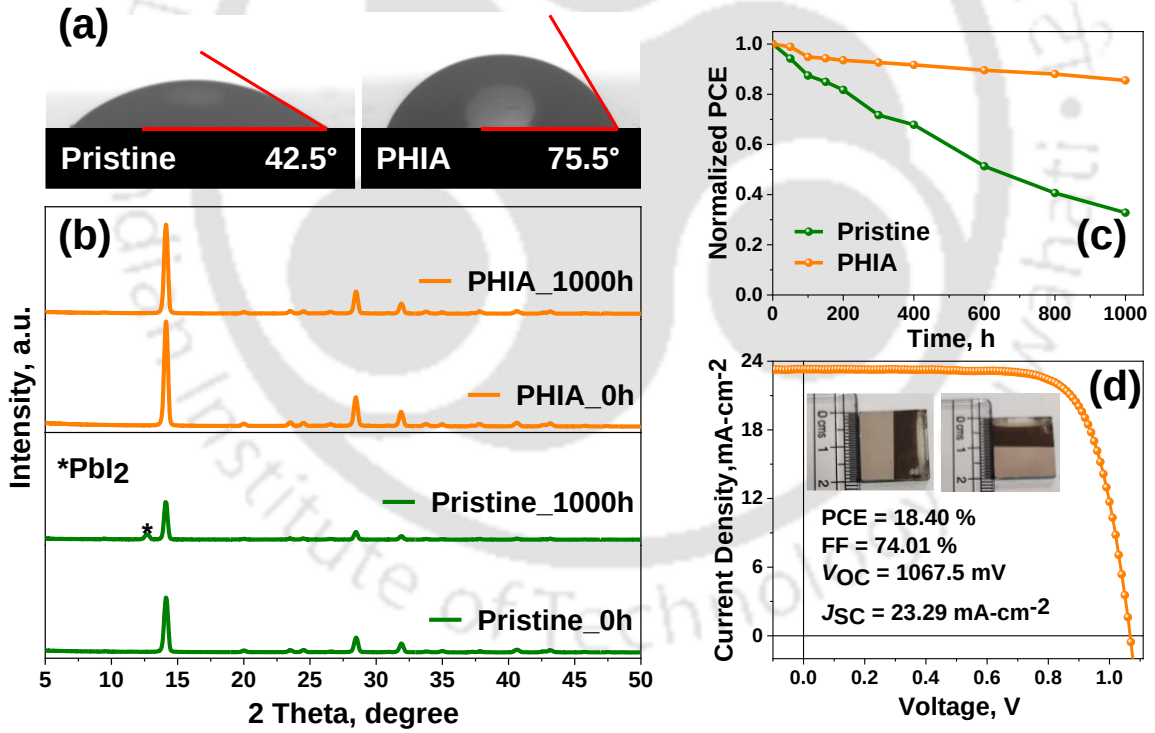

Figure 4.9 (a) Contact angle measurement of the pristine and PHIA passivated films, (b) XRD patterns of perovskite films aged in a relative humidity of 35–45%., (c) Normalized efficiency of pristine and PHIA modified devices aged at room temperature in a relative humidity of 35–45%., and (d) *J–V* curves of the PHIA modified 2 cm^2 large area device.

The CPE also distributes along the GBs, which enhances the hydrophobicity of the layer. This can be confirmed from the contact angle measurement performed with the pristine and passivated films (**Figure 4.9a**). In comparison to the pristine film, the contact angle

substantially improves for the passivated one. Hence, PHIA passivation endorses better hydrophobicity and prevents the penetration of moisture in perovskite film. This can be further evident through the XRD study of the films performed at room temperature in 35-45% relative humidity (**Figure 4.9b**). In the pristine film, the peak for the PbI_2 phase at 12.7° is observed which clearly specifies the degradation of the perovskite phase. In contrast, no peak for the PbI_2 phase is realized in the passivated film. After confirming the film stability, the device stability was also carried out at similar conditions (**Figure 4.9c**). PCE of the pristine device regularly declines over time and after 1000 hours degraded to 30% of its initial PCE. However, the passivated device remains almost 85% stable after 1000 hours. More importantly, large-area solar cell devices were fabricated, to prove the acceptability of this method of CPE passivation for future commercialization. Device with an active area of 2 cm^2 was fabricated with PHIA molecules and it exhibits a high PCE of 18.40% (**Figure 4.9d**).

4.3 Conclusions

In summary, an innovative trap passivation approach of perovskite with conjugated polyelectrolyte has been demonstrated for the first time here to the best of our knowledge. PHIA polymer effectively passivates the traps at surface and grain boundaries and offers better quality perovskite films with larger grain sizes. Consequently, the passivated device reveals lower recombination, minimum charge accumulation at the interface and lesser traps, facilitating better charge transport. As a result, passivated device discloses a high PCE of 20.17 % with a J_{SC} of 23.92 mA-cm^{-2}, FF of 78.4% and V_{OC} of 1076.2 mV. Additionally, the ambient stability of the device mainly improves after passivation signifying that PHIA can sufficiently restricts the moisture penetration in the perovskite. Large area devices fabricated with this approach results in a very high PCE of 18.40%. Therefore, this approach turns up to be a facile strategy in the direction of large-scale commercial fabrication of efficient and stable PSCs.

4.4 Experimental Section

Materials: FTO glass substrates (13 Ω sq^{-1}), PbI_2 (99.8%), DMSO (anhydrous, 99.8%), solvents DMF (anhydrous, 99.8%), Chlorobenzene, Toluene (anhydrous, 99.8%) were purchased from Sigma-Aldrich. MAI was procured from Dyesol. Nickel nitrate

hexahydrate ($Ni(NO_3)_2 \cdot 6H_2O$) was obtained from TCI. All other chemicals were used as received.

Synthesis of PPTE: The conjugated polymer PPBr was synthesised by previously established method.[26] PPBr (0.050 g, 0.14 mmol) and dimethyl-5-hydroxyisophthalate (0.298 g, 1.42 mmol) were dissolved in DMF (5 mL) in presence of K_2CO_3 (10 eq.), the reaction mixture was maintained at 80 °C and stirred for 24 h. Then it was cooled and poured into chloroform, and washed with dil. HCl followed by brine solution. The organic layer was dried over anhydrous magnesium sulfate and evaporated to obtain solid powder product PPTE (70 % yield). ^{1}H NMR (400MHz, $CDCl_3$): δ ppm, 8.08(b), 7.53(b), 7.09(b), 4.02(b), 3.80(b), 2.56(b).

Synthesis of PHIA: The final anionic conjugated polyelectrolyte was obtained through the alkali induced saponification method. PPTE (0.050 g) was dissolved in THF and a solution of sodium hydroxide (0.3 g) in 3 mL water was added. The reaction mixture was maintained at 50 °C and stirred for 12 h. After that, it was cooled to room temperature and THF was removed, and the mixture was dialyzed against water for 3 days using a membrane with a molecular weight cut-off of 3.5 kDa. The solution was then freeze-dried to get brown solid PHIA (76 % yield). ^{1}H NMR (400MHz, D_2O): δ ppm, 7.92(b), 7.40(b), 7.09(b), 3.89(b), 1.92(b).

Preparation of NiO_x Film: NiO_x precursor solution was prepared by dissolving 1M Nickel nitrate hexahydrate and 1M Ethylenediamine in 1mL Ethylene Glycol. Then the NiO_x layer was coated as hole transporting layer on the cleaned FTO substrate. The cleaning process was started with detergent and followed by deionized water, acetone, and isopropyl alcohol for 15 min for each solvent, then dried and treated with UV-ozone for 30 min. NiO_x precursor solution was spin coated onto the FTO substrates @3000 rpm for 40 sec. Later the substrates were post-annealed at 300 °C for 60 min in ambient air.

Device Fabrication: The $MAPbI_3$ precursor solution was prepared in a glovebox by dissolving MAI and PbI_2 (1:1 ratio) in a mixed solvent of γ-Butyrolactone and DMSO (7:3, v/v) where the concentration of Pb^{2+} was 1.26. The solution was heated overnight and filtered with 0.45 μm filter prior to spin coating. For the modified device, different concentrations of PHIA additive were added to the precursor solution. The filtered precursor solution was spin coated on the NiO_x coated FTO in a two-step spin coating process i.e. 750 rpm for 20 sec and 4000 rpm for 60 sec. In the second step 160 mL

anhydrous Toluene was dripped after 20 sec as antisolvent and after that the substrates were annealed @80° C for 10 min. Above the perovskite layer 12 mg/mL PCBM solution was coated @1200 rpm as ETL and again annealed @80 °C for 5 min. After that, a thin layer of Rhodamine 101 inner salt (0.5 mg/mL) was spin coated @4000 rpm. Finally, Ag was thermally deposited by using a shadow mask to yield an active area of 0.12 cm^2. The area for the large area device was 2 cm^2.

Device Characterization: The perovskite blend films were analysed by UV-vis absorption spectroscopy (Perkin Elmer Lamda-35), IR spectroscopy (LabRam HR). The XRD patterns of the samples were recorded using a Rigaku Micromax-007HF diffractometer equipped with Cu Kα1 irradiation (λ = 1.54184 Å). The morphology of the samples were investigated by scanning electron microscopy (SEM, Hitachi S-4800) and AFM(Oxford, Cypher).The current density−voltage (*J*−*V*) characteristic curves were measured using a Keithley 2400 source meter under argon atmosphere by illuminating the device with a solar simulator (AM 1.5G, 100 mW cm^{-2}, Oriel Sol 3A solar simulator, Newport). All light characteristic was done under the same solar simulator lamp. The incident external quantum efficiency (EQE) was obtained by using an Oriel IQE-200 instrument under ambient condition. Electrochemical measurements were performed with a CH Instruments 760D.

References

1. A. Kojima, K. Teshima, Y. Shirai and T. Miyasaka, *J. Am. Chem. Soc.*, 2009, **131**, 6050-6051.
2. W. Nie, H. Tsai, R. Asadpour, J.-C. Blancon, A. J. Neukirch, G. Gupta, J. J. Crochet, M. Chhowalla, S. Tretiak, M. A. Alam, H.-L. Wang and A. D. Mohite, *Science*, 2015, **347**, 522.
3. S. D. Stranks, G. E. Eperon, G. Grancini, C. Menelaou, M. J. P. Alcocer, T. Leijtens, L. M. Herz, A. Petrozza and H. J. Snaith, *Science*, 2013, **342**, 341.
4. National Renewable Energy Laboratory, Best research-cell efficiencies chart, https://www.nrel.gov/pv/assets/pdfs/best-research-cell-efficiencies.20200104.pdf, (accessed 16.02.2021).
5. C. C. Boyd, R. Cheacharoen, T. Leijtens and M. D. McGehee, *Chem. Rev.*, 2019, **119**, 3418-3451.
6. Y. Shao, Y. Fang, T. Li, Q. Wang, Q. Dong, Y. Deng, Y. Yuan, H. Wei, M. Wang, A. Gruverman, J. Shield and J. Huang, *Energy Environ. Sci.*, 2016, **9**, 1752-1759.
7. D. Bi, C. Yi, J. Luo, J.-D. Décoppet, F. Zhang, Shaik M. Zakeeruddin, X. Li, A. Hagfeldt and M. Grätzel, *Nat. Energy*, 2016, **1**, 16142.
8. B. Chen, P. N. Rudd, S. Yang, Y. Yuan and J. Huang, *Chem. Soc. Rev.*, 2019, **48**, 3842-3867.
9. L. Fu, H. Li, L. Wang, R. Yin, B. Li and L. Yin, *Energy Environ. Sci.*, 2020, **13**, 4017-4056.
10. A. Mahapatra, D. Prochowicz, M. M. Tavakoli, S. Trivedi, P. Kumar and P. Yadav, *J. Mater. Chem. A*, 2020, **8**, 27-54.
11. M. Adil Afroz, N. Ghimire, K. M. Reza, B. Bahrami, R. S. Bobba, A. Gurung, A. H. Chowdhury, P. K. Iyer and Q. Qiao, *ACS Appl. Energy Mater.*, 2020, **3**, 2432-2439.
12. R. Garai, M. A. Afroz, R. K. Gupta and P. K. Iyer, *Advanced Sustainable Systems*, 2020, **4**, 2000078.
13. X. Wu, L. Zhang, Z. Xu, S. Olthof, X. Ren, Y. Liu, D. Yang, F. Gao and S. Liu, *J. Mater. Chem. A*, 2020, **8**, 8313-8322.
14. X. Zheng, B. Chen, J. Dai, Y. Fang, Y. Bai, Y. Lin, H. Wei, Xiao C. Zeng and J. Huang, *Nat. Energy*, 2017, **2**, 17102.
15. X. Zheng, Y. Deng, B. Chen, H. Wei, X. Xiao, Y. Fang, Y. Lin, Z. Yu, Y. Liu, Q. Wang and J. Huang, *Adv. Mater.*, 2018, **30**, 1803428.
16. W. Chen, Y. Wang, G. Pang, C. W. Koh, A. B. Djurišić, Y. Wu, B. Tu, F.-z. Liu, R. Chen, H. Y. Woo, X. Guo and Z. He, *Adv. Funct. Mater.*, 2019, **29**, 1808855.
17. H. Li, C. Liang, Y. Liu, Y. Zhang, J. Tong, W. Zuo, S. Xu, G. Shao and S. Cao, *ACS Appl. Mater. Interfaces*, 2017, **9**, 6064-6071.
18. J. Jiang, Q. Wang, Z. Jin, X. Zhang, J. Lei, H. Bin, Z.-G. Zhang, Y. Li and S. Liu, *Adv. Energy Mater.*, 2018, **8**, 1701757.

19. P.-L. Qin, G. Yang, Z.-w. Ren, S. H. Cheung, S. K. So, L. Chen, J. Hao, J. Hou and G. Li, *Adv. Mater.*, 2018, **30**, 1706126.

20. M. Kim, S. G. Motti, R. Sorrentino and A. Petrozza, *Energy Environ. Sci.*, 2018, **11**, 2609-2619.

21. F. Wang, A. Shimazaki, F. Yang, K. Kanahashi, K. Matsuki, Y. Miyauchi, T. Takenobu, A. Wakamiya, Y. Murata and K. Matsuda, *J. Phys. Chem. C*, 2017, **121**, 1562-1568.

22. L. Zuo, H. Guo, D. W. deQuilettes, S. Jariwala, N. De Marco, S. Dong, R. DeBlock, D. S. Ginger, B. Dunn, M. Wang and Y. Yang, *Science Advances*, 2017, **3**, e1700106.

23. Z. Zhang, M. Sheri, Z. A. Page, T. Emrick, A. Saeki, Y. Liu and T. P. Russell, *ACS Appl. Mater. Interfaces*, 2020, **12**, 56068-56075.

24. S. Kim, J.-E. Jeong, J. Hong, K. Lee, M. J. Lee, H. Y. Woo and I. Hwang, *ACS Appl. Mater. Interfaces*, 2020, **12**, 12328-12336.

25. L. Zhang, X. Zhou, J. Xie, S. Chen, S. Bae, J. Kim and B. Xu, *J. Mater. Chem. A*, 2020, **8**, 8238-8243.

26. A. S. Tanwar and P. K. Iyer, *ACS Omega*, 2017, **2**, 4424-4430.

27. M. A. Afroz, R. K. Gupta, R. Garai, M. Hossain, S. P. Tripathi and P. K. Iyer, *Org. Electron.*, 2019, **74**, 172-178.

28. R. Azmi, N. Nurrosyid, S. H. Lee, M. Al Mubarok, W. Lee, S. B. Hwang, W. P. Yin, T. K. Ahn, T. W. Kim, D. Y. Ryu, Y. R. Do and S. Y. Jang, *ACS Energy Lett.*, 2020, **5**, 1396-1403.

29. Y. Zhang, P. Wang, X. Yu, J. Xie, X. Sun, H. Wang, J. Huang, L. Xu, C. Cui, M. Lei and D. Yang, *J. Mater. Chem. A*, 2016, **4**, 18509-18515.

30. R. K. Gupta, R. Garai, M. Hossain, A. Choudhury and P. K. Iyer, *ACS Sustainable Chemistry & Engineering*, 2021, **9**, 7993-8001.

31. V. D. Mihailetchi, J. Wildeman and P. W. M. Blom, *Phys. Rev. Lett.*, 2005, **94**, 126602.

32. X. Hou, S. Huang, W. Ou-Yang, L. Pan, Z. Sun and X. Chen, *ACS Appl. Mater. Interfaces*, 2017, **9**, 35200-35208.

33. V. D. Mihailetchi, L. J. A. Koster, J. C. Hummelen and P. W. M. Blom, *Phys. Rev. Lett.*, 2004, **93**, 216601.

34. W. Zhang, L. Wan, S. Fu, X. Li and J. Fang, *J. Mater. Chem. A*, 2020, **8**, 6546-6554.

35. Q. Wang, B. Chen, Y. Liu, Y. Deng, Y. Bai, Q. Dong and J. Huang, *Energy Environ. Sci.*, 2017, **10**, 516-522.

[This page was intentionally left blank]

CHAPTER 5

Triple Passivation Approach to Laminate Perovskite Layer for UV and Ambient Stable Photovoltaics

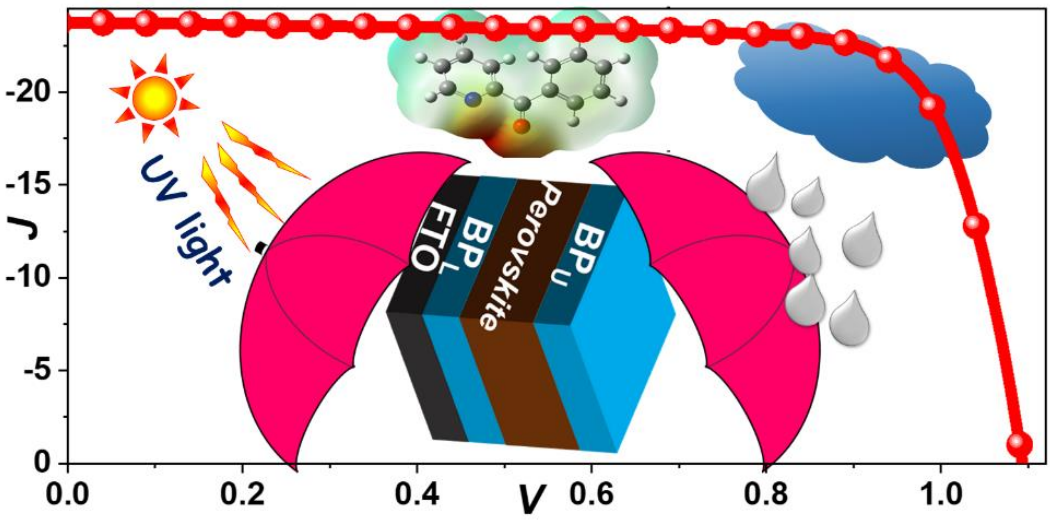

Manuscript: Rabindranath Garai, Ritesh Kant Gupta, Anwesha Choudhury, Parameswar Krishnan Iyer, "Triple Passivation Approach to Laminate Perovskite Layer for UV and Ambient Stable Photovoltaics". (Under review)

[This page was intentionally left blank]

Abstract

The instability of the perovskite solar cells (PSCs) towards ultraviolet (UV) irradiation and moisture is a restricting factor in terms of commercialization even after achieving excellent power conversion efficiencies (PCEs). Herein, an advanced triple passivation technique has been strategically designed and demonstrated utilizing UV absorbing 2-benzoylpyridine (BP) molecule as a passivation additive to laminate perovskite and improve PSC stability. Double layers of BP were coated on both the side perovskite layer, and the molecule was also incorporated in the precursor solution. This strategy significantly improved the perovskite crystallinity, film quality, lowered the recombination and enhanced the carrier transport in the PSC. The triple passivated device exhibited a high PCE of 20.46% with almost negligible hysteresis. Further, passivated large-area devices were also fabricated that demonstrated a PCE of 18.61%. Moreover, the triple passivation approach discloses impressive UV and ambient stability because it can effectively shield the perovskite layer from UV illumination and moisture.

5.1 Overview

Recently, perovskite solar cells (PSCs) have received massive research attention due to the extraordinary growth of power conversion efficiencies (PCEs) from 3.8% to >25%.[1, 2] This immense advancement is due to the remarkable properties of the perovskite materials e.g. bandgap tunability, strong absorption coefficient, superior transport of charge carriers, extended carrier diffusion lengths, etc.[3-6] Despite the impressive optoelectronic characteristics and high PCEs, PSCs suffer from substantial instability under ultraviolet (UV) irradiation and humid conditions which limit their practical application. Although extensive studies have been dedicated towards enhancing the durability of PSCs in ambient conditions,[7, 8] there have been meagre efforts to enhance the UV stability. Under high-energy photons of UV radiation, perovskite materials readily degrade into lead iodide (PbI_2), methylamine and hydrogen.[9-12] Methylamine and hydrogen being highly volatile release easily from the crystal lattice whereas, the PbI_2 will be left behind in the films. Additionally, the surface and grain boundary defect states of polycrystalline perovskite accelerate its degradation and drives towards lesser device efficacy. [12]

Modification of the transport layer by chemical doping is the most recognized strategy for UV stabilization of the perovskite layer.[13-19] One more efficient technique for increasing UV stability is utilizing certain materials with strong UV absorption.[20-23] Multifunctional organic molecules having absorption in the UV region can potentially enhance the durability of PSCs under UV irradiation.[22] Such molecules can simultaneously passivate the defect states, improve device efficiency as well as their long-term stability.[24-32] All these passivation molecules are generally utilized for interface passivation or bulk passivation (by adding in the precursor solution) of perovskite. In most of the reported literature, the surface passivation layer is either coated on top of perovskite or incorporated as a bottom layer. Recently, double-sided interfacial passivation where the passivating layer is coated on either side of the perovskite, has also gained research attention to improve device performance.[33, 34] However, there are no reports on the simultaneous use of double-sided passivation along with bulk passivation i.e. triple passivation, to the best of our knowledge.

Herein, a unique concept of triple passivation has been developed by utilizing 2-benzoylpyridine (BP) molecule as a passivation agent. As the BP molecule has strong absorption in the UV region, it can efficiently prevent the UV degradation of PSCs. Also, the hydrophobic aromatic rings provide moisture resistance when BP is coated on top of

perovskite. Further, the carbonyl group and pyridinium-N functionality facilitates decreased trap states of bulk perovskite. Initially, two layers of BP molecule were coated [one lower BP layer (BP_L) coated between the FTO and perovskite and one upper BP layer (BP_U) coated over the perovskite] for perovskite passivation to improve device performance. After this BP molecule was also added into the perovskite precursor solution along with this BP bilayer to attain optimum passivation. This triple passivation strategy surges all the device parameters, i.e., short-circuit current density (J_{SC}), open-circuit voltage (V_{OC}) as well as fill factor (FF) and effectively reduces the device hysteresis. The champion triple passivated device demonstrates a high PCE of 20.46% with negligible hysteresis. To validate the expediency of this approach for real application, large-area device has also been prepared. The modified device reveals lesser trap states, suppressed carrier recombination and better charge transport due to effective passivation. Furthermore, the triple passivation strategy led to significant UV stability and excellent ambient stability.

5.2 Results and Discussions

The initial strategy in this work was to investigate the effect of double BP layer passivation on the PSC devices. Hence, devices with the architecture of FTO/NiO/BP_L/Perovskite/BP_U/$PC_{61}BM$/ Rhodamine 101/Ag were fabricated where both the layers were optimized one after the other (**Figure 5.1a**). **Figure 5.1b** represents the devices with the sequential optimization of BP concentration in various layers while **Figure 5.1c** illustrates the box chart for 15 devices for all the PSCs. At first, BP_L was optimized by coating various concentrations over the NiO layer. The box chart reveals that the device fabricated with 1 mg-mL^{-1} BP (BPS1) exhibits higher device parameters along with narrower distribution as compared to BPS2 and pristine device. In synchronization with this optimization, the BP_U layer with various concentrations was introduced. BPD1 reveals improved device performance with better reproducibility where both the BP layers were coated with 1 mg-mL^{-1} solution. This device shows an average PCE of 17.28±0.41% which was still relatively low (**Table 5.1**). Subsequently, to further improve the device efficacy, BP molecules (in varying concentrations) were introduced into the perovskite precursor as a third passivation strategy. Triple passivated BPT device offered the highest device result (PCE-20.46%) and superior reproducibility among all the device types with an average PCE of 19.99±0.32%. This incredible improvement of device performance is due to the high-quality perovskite film formation obtained as a result of triple passivation strategy.

Table 5.1: Photovoltaic parameters of PSCs with different concentration of additives.

Device	J_{SC}, mA-cm^{-2}	V_{OC}, mV	FF, %	PCE, Best (Average), %
Pristine	21.14	1004.9	71.1	15.09 (13.72±0.63)
BPS1	22.34	1022.6	74.2	16.94 (16.11±0.50)
BPS2	20.23	1021.5	73.6	15.30 (14.42±0.42)
BPD1	22.56	1058.3	74.7	17.84 (17.28±0.41)
BPD2	21.81	1053.7	71.7	16.47 (15.74±0.55)
BPT1	23.74	1072.6	75.4	19.20 (18.50±0.43)
BPT	23.75	1093.4	78.8	20.46 (19.99±0.32)
BPT3	22.10	1083.7	74.8	19.72 (16.96±0.70)

[a]Average of 15 devices.

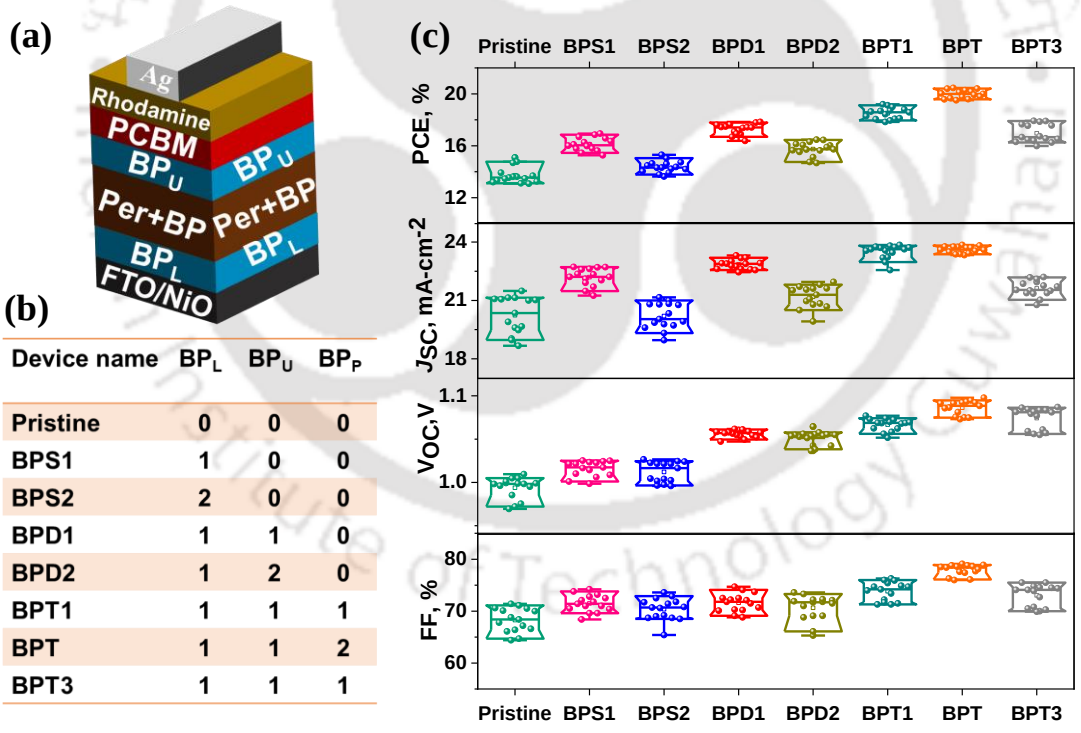

Figure 5.1 (a) Device architecture, (b) Name of the devices with varying BP concentration (in mg-mL^{-1}) in single, double and triple layer optimization (c) Box chart of device parameters.

To investigate the grain growth as well as the crystallization of perovskite, all films (single, double, and triple passivated) were characterized with field emission scanning electron microscopy (FESEM) and the average grain sizes were also calculated (**Figure 5.2a, b)**.

The pristine film reveals smaller grains with an average size of 232 nm. After single layer passivation, both BPS1 and BPS2 films exhibit larger grains as well as better surface coverage than the pristine. When the BP_U layer was coated for bilayer passivation, the grains combine with one another and the grain boundaries start to diminish. Both BPD1 and BPD2 films display improved surface coverage. Along with these features, average grain size increased on triple passivation up to a specific concentration of BP and later, it reduces due to overcrowding of additive. BPT illustrates superior quality film with maximum surface coverage and the largest average grain size of 515 nm. Additionally, all the films displayed polycrystalline X-ray diffraction (XRD) peak at 2θ value of 14.12, 28.46, and 31.86 corresponding to (110), (220), and (310) lattice planes, respectively (**Figure 5.2c)**. BPT film with maximum peak intensity exhibits the best crystallinity among all.

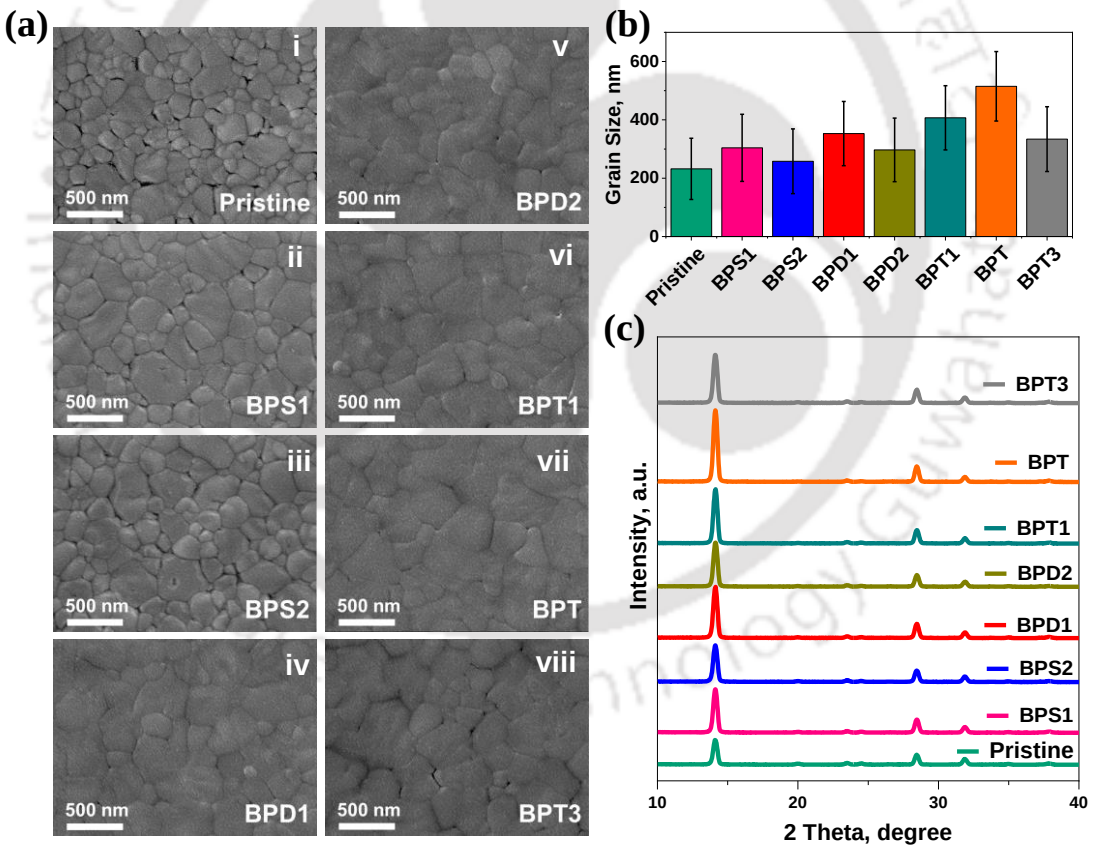

Figure 5.2 (a) Surface FESEM images of (i) Pristine, (ii) BPS1, (iii) BPS2, (iv) BPD1 (v) BPD2, (vi) BPT1, (vii) BPT, & (viii) BPT3 films, (b) Average grain size variation of all the films, and (c) XRD plots of all the films.

The BP molecule can also strongly interact with perovskite and efficiently passivate the trap states. The electrostatic potential (ESP) profile of the BP molecule, obtained from

density functional theory (DFT) studies, reveals a strong local electron density around the carbonyl group and pyridinyl-N functionality (**Figure 5.3a)**. These groups interact with the positively charged defects in perovskite lattice and diminish the trap states. Fourier transform infrared (FTIR) analyses were conducted in attenuated total reflectance (ATR) mode with the BP, pristine and BPT films to investigate the interaction of BP with $MAPbI_3$ (**Figure 5.3b)**. The pure BP film exhibits stretching vibration of the C=O and C=N bond at 1740 and 1666 cm^{-1} respectively which shifts to 1723 and 1645 cm^{-1} for the triple passivated BPT film. This result indicates significant interaction between $MAPbI_3$ and BP, especially with the carbonyl group as well as pyridinium-N functionality.

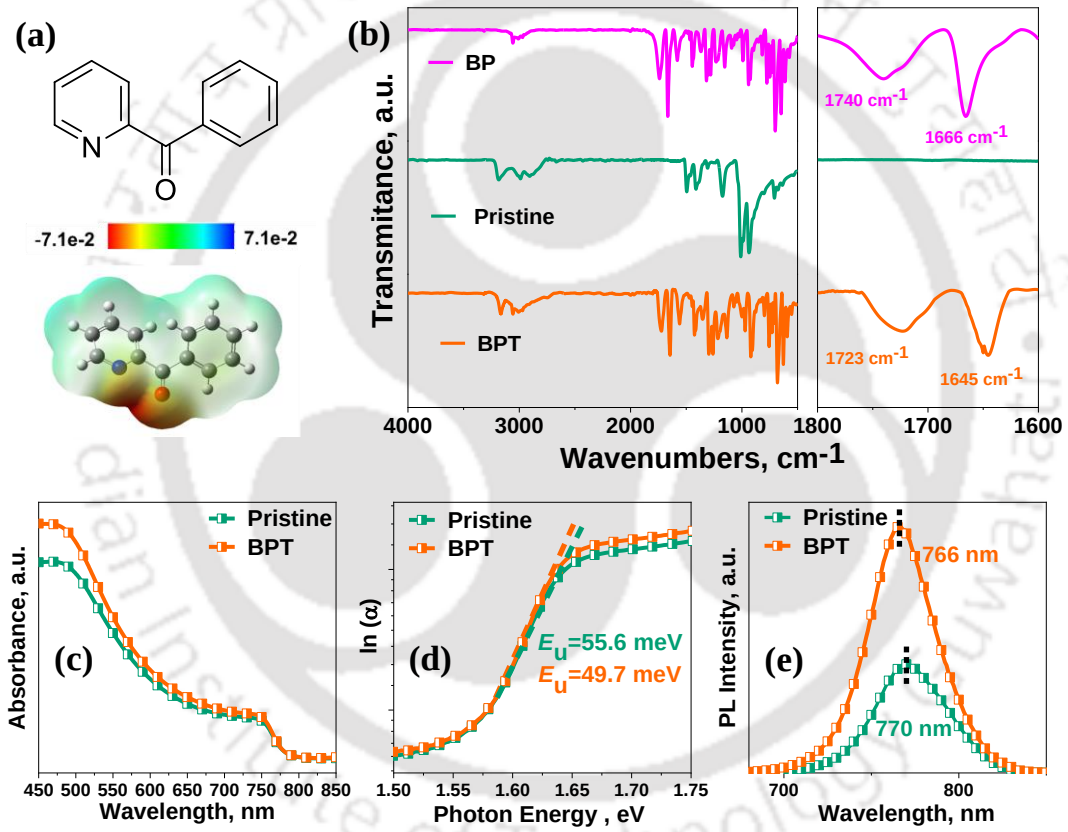

Figure 5.3 (a) ESP profile of BP molecule obtained from DFT study, (b) ATR-FTIR spectra of BP, Pristine and BPT film, (c) UV-vis absorption spectra of the pristine and BPT films, (d) Plot of ln(α) versus photon energy, and (e) Steady state PL spectra of perovskite films.

Additionally, the BPT film discloses a higher absorption in UV-vis spectra suggesting improved light-harvesting property (**Figure 5.3c**). Urbach energy (E_u) was also calculated from ln(α) versus photon energy plot of pristine and passivated film (**Figure 5.3d**).[35, 36] Pristine film exhibits E_u of 55.6 meV which reduces up to 49.7 meV after triple passivation signifying substantial interaction of BP with perovskite that results in less band edge disorder as well as mitigated defect density in the BPT film. To further confirm the trap

passivation, steady-state photoluminescence (PL) measurement of the perovskite films was performed (**Figure 5.3e**). The BPT film exhibited a blue-shifted PL peak than the pristine, suggesting effective trap passivation. Moreover, BPT film reveals a higher PL intensity as compared to the pristine one because of the lesser non-radiative recombination originating from reduced defect density.

Consequently, a high PCE of 20.46% is achieved for the BPT device with a J_{SC} of 23.75 mA-cm^{-2}, V_{OC} of 1093.4 mV and FF of 78.8%. The triple passivated BPT film offers high-quality perovskite film with better crystallinity leading to reduced ion migration and better charge transport to suppress hysteresis. To estimate the hysteresis index (HI), the *J–V* plot was recorded in both forward & reverse scans for the pristine and BPT devices (**Figure 5.4a, Table 5.2)**. The pristine device demonstrates a considerable hysteresis with a HI of 9.7% whereas, it becomes negligible for the BPT device with a HI of 1.6%. Furthermore, large-area BPT device (~2.5 cm^2) was also fabricated which reveals a high efficacy of 18.61% (**Figure 5.4b**). To confirm the *J-V* results, steady-state analysis was carried out at maximum power for the pristine and BPT devices (**Figure 5.4c)**. BPT passivated device reveals a constant J_{SC} along with a stable PCE of 19.91%, while the pristine device exhibits a gradual degradation. BPT device also exhibits higher external quantum efficiency (EQE) than pristine, signifying superior charge transport towards respective electrodes (**Figure 5.4d**). Integrated J_{SC} values obtained from the EQE spectra are in good agreement with *J-V* results.

Table 5.2: Hysteresis study of the pristine and BPT device.

Device	J_{SC}, mA-cm^{-2}	V_{OC}, mV	FF, %	PCE, %	HI, %
Pristine_Forward	21.14	1004.9	71.1	15.09	9.7
Pristine_Reverse	21.08	998.8	64.7	13.62	
BPT_Forward	23.75	1093.4	78.8	20.46	1.6
BPT_Reverse	23.77	1092.4	77.6	20.14	

To validate the V_{OC} improvement in the triple passivated device, built-in potential (V_{bi}) was estimated from the Mott−Schottky (MS) analysis (**Figure 5.4e**). The V_{bi} for the pristine and BPT devices are 0.99 V and 1.07 V, respectively and the higher V_{bi} results in enhanced V_{OC}

for the modified device.[31, 37] Furthermore, interfacial charge density (*N*) was determined from MS analysis which provides significant insight into the charge transport behaviour.[37] The estimated *N* values for the pristine and BPT devices are 2.70×10^{16} and 1.42×10^{16} cm^{-3}, respectively.[37, 38] The smaller *N* value of the BPT device specifies excellent charge extraction due to reduced interfacial charge accumulation. This can be further verified from the *J-V* analysis conducted in dark condition (**Figure 5.4f**). BPT device reveals a smaller leakage current and lower reverse saturation current than the pristine which leads to superior charge transport and mitigated carrier recombination.

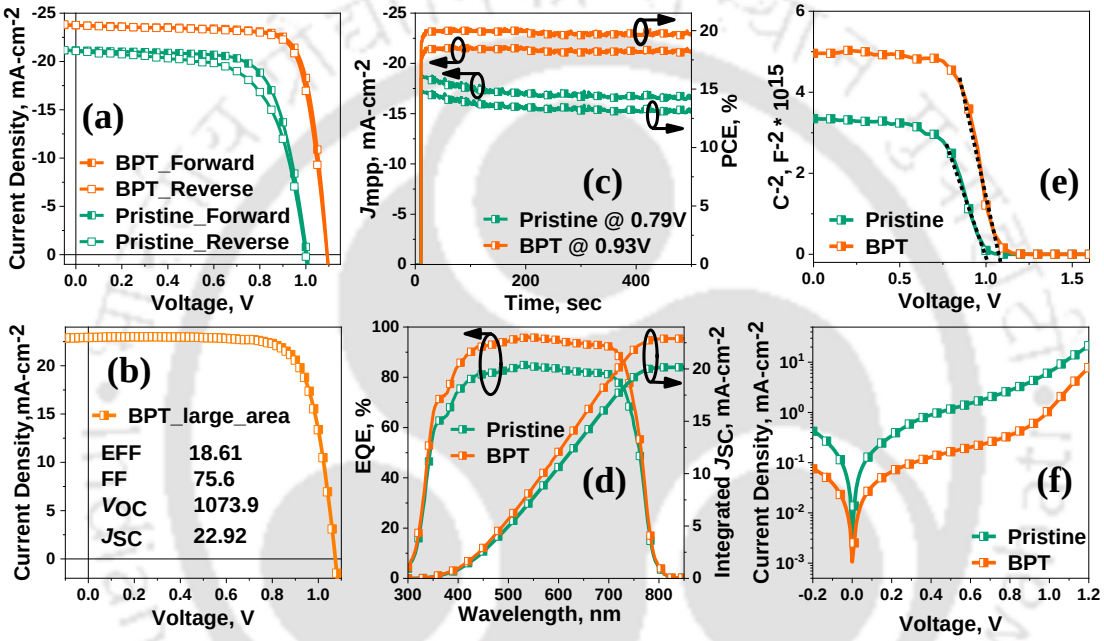

Figure 5.4 Hysteresis of (a) pristine device, & (b) BPT device, (c) Steady state analysis, (d) EQE curves of the pristine and BPT device, (e) Mott−Schottky plots, and (f) Dark J-V measurement.

To explore in-depth into the charge transport and carrier recombination process, light intensity versus J_{SC} and V_{OC} measurements were performed. BPT device reveals a slope closer to one compared to the pristine in J_{SC}-light intensity plot (**Figure 5.5a**). This suggests excellent transport of charge carriers due to reduced recombinational loss. The dependence of V_{OC} with respect to light intensity revealed a linear relation for both the devices (**Figure 5.5b**). The slope nK_BT/q can be computed from the linearly fitted semi-log curve where, n represents ideality factor, K_B is the Boltzmann constant, T signifies absolute temperature, and q is the elementary charge.[39, 40] A high n value indicates more defect-aided recombination at the interface. In contrast to pristine, BPT device displays a lower slope signifying better trap passivation and results in lower trap-assisted recombination. To further investigate the trap passivation and carrier recombination mechanism, impedance

spectroscopy (IS) analysis was performed. **Figure 5.5c** depicts the Nyquist plots for pristine and BPT device recorded at 0.80 V and the graph fitted with an equivalent circuit (Inset). In comparison to pristine, BPT device unveils a higher recombination resistance (R_{rec}) due to minimized recombination and offers better charge transport. Subsequently, trap density of states (*t*-DOS) was computed from the capacitance values acquired from the IS measurement at varying bias (**Figure 5.5d**).[24, 41] BPT device elucidates reduced *t*-DOS with a narrow distribution corresponding to the pristine one.

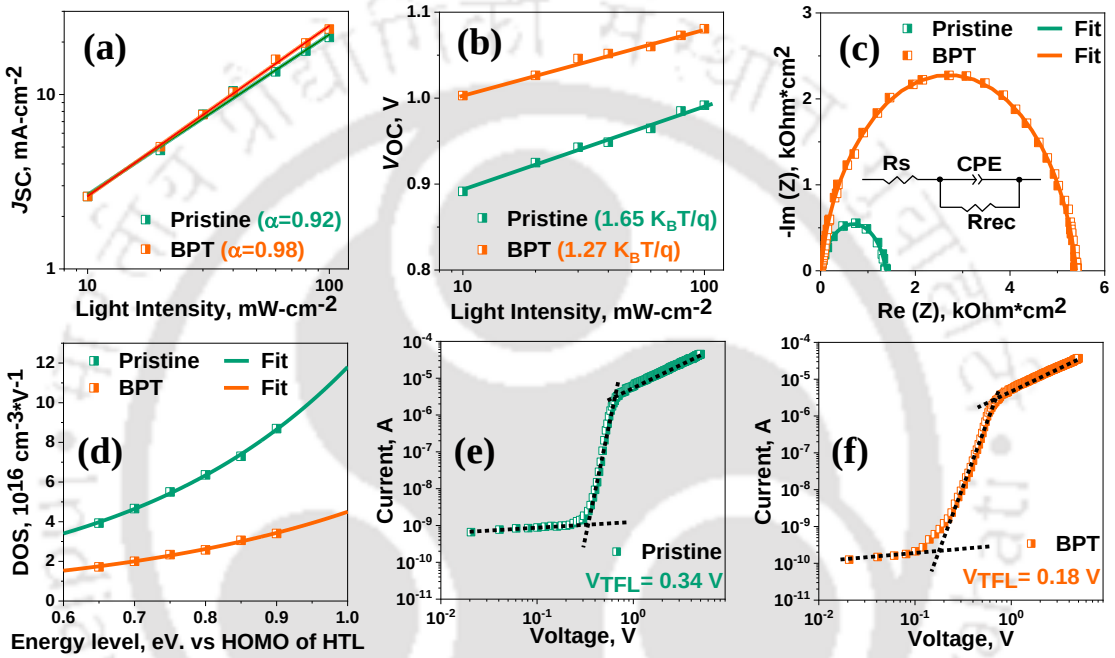

Figure 5.5 (a) J_{SC}-light intensity plot, (b) V_{OC}-light intensity plot, (c) Nyquist plots of the pristine and BPT device, (d) Trap density of states (*t*-DOS) analysis, and Dark *J*–*V* characteristics of hole-only devices (e) pristine & (f) BPT device.

In addition, to realize a proper assessment of trap states (N_t), dark *J*–*V* characteristics were measured for the hole-only devices before and after modification (**Figure 5.5e & f**). BPT device illustrates a smaller trap fill limited current (V_{TFL}) as well as lesser trap density than the pristine device. The estimated N_t for the pristine & BPT devices are 8.23×10^{15} and 4.36×10^{15} cm^{-3} respectively. Therefore, it can be concluded that tri layer additive engineering (BPT device) significantly passivates the trap states in perovskite, thus facilitating minimized carrier recombination with better charge transport and offering excellent device performance.

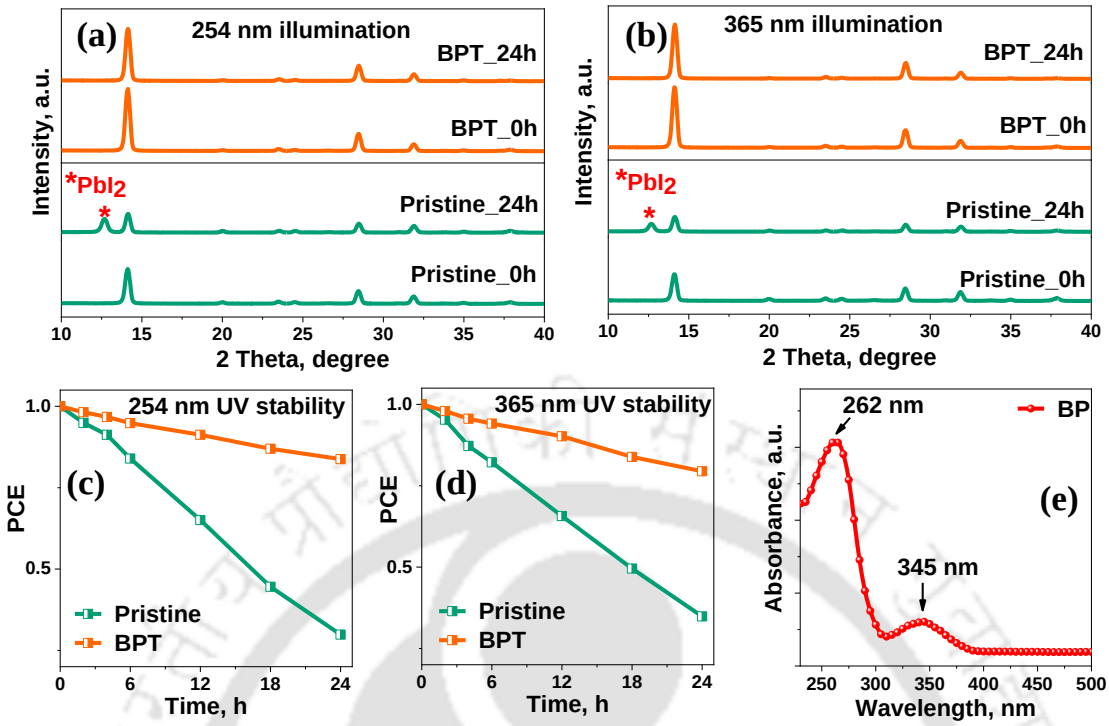

Figure 5.6 XRD stability study for the films with and without lower BP layer under (b) 254 nm & (c) 365 nm illumination, and UV stability study of the pristine and BPT devices (c) 254 nm & (d) 365 nm illumination.

This practical trap passivation not only improves the device efficiency but also enhances device stability notably. This triple passivation strategy utilizing BP molecule can remarkably improve the UV stability of the device. To verify this, XRD stability of the pristine and BPT film was performed under UV illumination. **Figure 5.6a** represents the XRD profiles before and after 254 nm UV light illumination. The pristine film reveals a strong degradation after 24 hours which can be confirmed from the sharp growth of PbI_2 phase at ~12.6°. The BPT film remains unchanged after 24 hours and no degradation peak of PbI_2 phase is observed. UV stability was also carried out under 365 nm illumination (**Figure 5.6b**). Similarly, in this case, an intense peak of PBI_2 is produced for the pristine film after 24 hours of illumination whereas, the BPT film exhibits no such degradation peak. Thus, the triple passivation strategy efficiently enhanced the UV stability of the perovskite layer. This can be further validated by the UV stability for the pristine and BPT device. Under 254 nm UV radiation, the pristine device holds only ~30% of the original

PCE after 24 hours, while the BPT device retains up to ~84% of the initial PCE (**Figure 5.6c**). The stability study for both the devices under 365 nm UV light was also carried out (**Figure 5.6d**). The BPT device persists ~80% of its initial efficiency after 24 hours of illumination whereas, the pristine device degraded up to ~35%. This incredible UV stability is due to the strategic triple passivation with UV absorbing BP molecule. As the BP molecule has strong absorption in the UV region with peaks at 262 and 345 nm, it can act as a UV filter to protect the perovskite layer (**Figure 5.6e**). Particularly, BP_L layer mitigates the defect states at NiO-perovskite interface by preventing any undesirable redox reactions and also act as shield for perovskite.[42] This acts as a buffer layer which helps suppress non-radiative recombination and consequently, the device stability are largely improved.

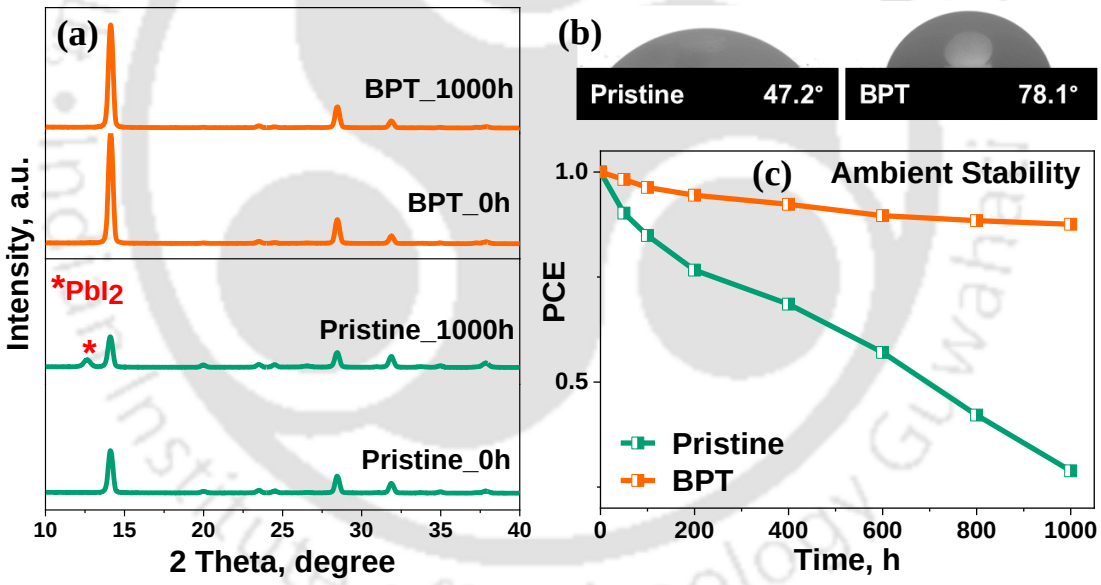

Figure 5.7 (a) XRD patterns of perovskite films stored in a relative humidity of 40–50%. (b) Water contact angle analysis of pristine and BPT films, and (c) Ambient stability of the pristine and BPT devices aged at a relative humidity of 40–50%.

Furthermore, the ambient stability of the films was analyzed via XRD (**Figure 5.7a**), at 40-50% relative humidity. It is observed that the pristine film demonstrates significant degradation after 1000 hours, whereas the BPT film showed no signs of degradation. This is due to the enhanced hydrophobicity of the BPT film that restricts the moisture penetration, confirming improved ambient stability (**Figure 5.7b**). Subsequently, long-term

ambient stability for both the devices was tracked under 40-50% relative humidity for 1000 hours (**Figure 5.7c**). The BPT device displays remarkable stability with only ~12% loss after 1000 hours while the pristine PSC deteriorates gradually. The apparent decline in efficiency for the pristine device is due to a consistent reduction of J_{SC} and FF though, the V_{OC} remains nearly constant over time. Hence, this triple passivation strategy is efficient in upgrading the UV and ambient device stability simultaneously.

5.3 Conclusions

In summary, an innovative triple passivation strategy has been revealed, to enhance both UV and long-term ambient stability of PSCs using 2-benzoylpyridine (BP). This strategy can laminate the perovskite layer for improved stability and efficiency. The triple passivated PSC device exhibits mitigated charge carrier recombination with improved carrier transport due to the suitable trap passivation. Thus, the triple passivated device demonstrates a PCE of 20.46% for the small area and 18.61% large-area device. Additionally, almost negligible hysteresis is achieved for the triple passivated device because of reduced ion migration and suitable trap passivation. Finally, it can be concluded that, this approach concurrently overcomes the UV and ambient stability problems while also enhancing the efficiency and providing impetus towards commercial fabrication of PSCs in large-scale.

5.4 Experimental Section

Materials: FTO glass substrates (13 Ω sq^{-1}), PbI_2(99.8%), 2-benzoylpyridine, all solvents like DMF (anhydrous, 99.8%), DMSO (anhydrous, 99.8%), Toluene (anhydrous, 99.8%), Chlorobenzene were, procured from Sigma-Aldrich. MAI was purchased from Dyesol. Nickel nitrate hexahydrate ($Ni(NO_3)_2 \cdot 6H_2O$) was obtained from TCI. All other chemicals were used as received.

Device Fabrication: NiO_x precursor solution was prepared by dissolving 1M Nickel nitrate hexahydrate and 1M Ethylenediamine in 1ml Ethylene Glycol. Then the NiO_x layer was coated as hole transporting layer on the cleaned FTO. The cleaning process was started with detergent and followed by deionized water, acetone, and isopropyl alcohol for 15 min for each solvent, then dried and treated with UV-ozone for half an hour. NiO_x precursor

solution was spin coated onto the FTO substrates @3000 rpm for 40 sec. Afterward the substrates were post annealed at 300 °C for 60 min in ambient air. The $MAPbI_3$ precursor solution was prepared in a glovebox by dissolving MAI and PbI_2 (1:1 ratio) in a mixed solvent of gamma-Butyrolactone and DMSO (7:3, v/v) where the concentration of Pb^{2+} was 1.26. The solution was heated overnight and filtered with the 0.45 μm filter prior to spin coating. The filtered precursor solution was spin coated on the NiO_x coated FTO in a two-step spin coating process i.e. 750 rpm for 20 sec and 4000 rpm for 60 sec. In the second step 160 ml anhydrous Toluene was dripped after 20 sec as antisolvent and after that the substrates were annealed @80° C for 10 min. After this, 12 mg/ml PCBM solution was coated @1200 rpm as ETL and again annealed @80° C for 5 min. After that a thin layer of Rhodamine 101 inner salt (0.5 mg/ml) was spin coated @4000 rpm. Finally, Ag was thermally deposited by using a shadow mask to yield an active area of 0.12 cm^2.

Optimization of tipple passivation: The lower BP was coated @4000 rpm over the NiO_x coated FTO substrate with varied concentration isopropanol solution of the BP molecule. Then treated films were dried prior to perovskite coating. In the second step BP upper layer was optimized. For upper layer also, various concentration of BP in isopropanol was coated @4000 rpm over the perovskite. In the third step of optimization, different concentration of BP molecule was added into the perovskite precursor solution 30 minute prior to spin coating.

Device Characterization: The perovskite blend films were characterized by UV-vis absorption spectroscopy (Perkin Elmer Lambda-35), IR spectroscopy (LabRam HR). The XRD patterns of the samples were recorded using a Rigaku Micromax-007HF diffractometer equipped with Cu Kα1 irradiation (λ = 1.54184 Å). The morphology of the samples was investigated by scanning electron microscopy (SEM, Hitachi S-4800) and AFM (Oxford, Cypher). The current density−voltage (*J*−*V*) characteristic curves were measured using a Keithley 2400 source meter under argon atmosphere by illuminating the device with a solar simulator (AM 1.5G, 100 mW cm^{-2}, Oriel Sol 3A solar simulator, Newport). The incident external quantum efficiency (EQE) was obtained by using an Oriel IQE-200 instrument under ambient condition. Electrochemical measurements were performed with a CH Instruments 760D.

References

1. A. Kojima, K. Teshima, Y. Shirai and T. Miyasaka, *J. Am. Chem. Soc.*, 2009, **131**, 6050-6051.
2. National Renewable Energy Laboratory, Best research-cell efficiencies chart, https://www.nrel.gov/pv/assets/pdfs/best-research-cell-efficiencies.20200104.pdf, (accessed 24.04.2021).
3. G. Xing, N. Mathews, S. Sun, S. S. Lim, Y. M. Lam, M. Grätzel, S. Mhaisalkar and T. C. Sum, *Science*, 2013, **342**, 344.
4. W. Nie, H. Tsai, R. Asadpour, J.-C. Blancon, A. J. Neukirch, G. Gupta, J. J. Crochet, M. Chhowalla, S. Tretiak, M. A. Alam, H.-L. Wang and A. D. Mohite, *Science*, 2015, **347**, 522.
5. M. Ahmadi, Y.-C. Hsiao, T. Wu, Q. Liu, W. Qin and B. Hu, *Adv. Energy Mater.*, 2017, **7**, 1601575.
6. M. A. Afroz, R. K. Gupta, R. Garai, M. Hossain, S. P. Tripathi and P. K. Iyer, *Org. Electron.*, 2019, **74**, 172-178.
7. Q. Fu, X. Tang, B. Huang, T. Hu, L. Tan, L. Chen and Y. Chen, *Adv. Sci.*, 2018, **5**, 1700387.
8. R. Wang, M. Mujahid, Y. Duan, Z.-K. Wang, J. Xue and Y. Yang, *Adv. Funct. Mater.*, 2019, **29**, 1808843.
9. N. H. Nickel, F. Lang, V. V. Brus, O. Shargaieva and J. Rappich, *Adv. Electron. Mater.*, 2017, **3**, 1700158.
10. S.-W. Lee, S. Kim, S. Bae, K. Cho, T. Chung, L. E. Mundt, S. Lee, S. Park, H. Park, M. C. Schubert, S. W. Glunz, Y. Ko, Y. Jun, Y. Kang, H.-S. Lee and D. Kim, *Sci. Rep.*, 2016, **6**, 38150.
11. Q.-M. Hong, R.-P. Xu, T.-Y. Jin, J.-X. Tang and Y.-Q. Li, *Org. Electron.*, 2019, **67**, 19-25.
12. Q. Chen, N. De Marco, Y. Yang, T.-B. Song, C.-C. Chen, H. Zhao, Z. Hong, H. Zhou and Y. Yang, *Nano Today*, 2015, **10**, 355-396.
13. P. Chen, Z. Wang, S. Wang, M. Lyu, M. Hao, M. Ghasemi, M. Xiao, J.-H. Yun, Y. Bai and L. Wang, *Nano Energy*, 2020, **69**, 104392.
14. Q. Guo, J. Wu, Y. Yang, X. Liu, W. Sun, Y. Wei, Z. Lan, J. Lin, M. Huang, H. Chen and Y. Huang, *Nano Energy*, 2020, **77**, 105183.
15. W. Hu, Z. Wen, X. Yu, P. Qian, W. Lian, X. Li, Y. Shang, X. Wu, T. Chen, Y. Lu, M. Wang and S. Yang, *Adv. Sci.*, 2021, **n/a**, 2004662.
16. J. Jin, H. Li, C. Chen, B. Zhang, W. Bi, Z. Song, L. Xu, B. Dong, H. Song and Q. Dai, *ACS Appl. Energy Mater.*, 2018, **1**, 2096-2102.
17. G. Liu, B. Yang, H. Chen, Y. Zhao, H. Xie, Y. Yuan, Y. Gao and C. Zhou, *Appl. Phys. Lett.*, 2019, **115**, 213501.
18. B. Roose, C. M. Johansen, K. Dupraz, T. Jaouen, P. Aebi, U. Steiner and A. Abate, *J. Mater. Chem. A*, 2018, **6**, 1850-1857.

19. F. Wan, X. Qiu, H. Chen, Y. Liu, H. Xie, J. Shi, H. Huang, Y. Yuan, Y. Gao and C. Zhou, *Org. Electron.*, 2018, **59**, 184-189.

20. N. U. Rahman, W. U. Khan, S. Khan, X. Chen, J. Khan, J. Zhao, Z. Yang, M. Wu and Z. Chi, *J. Mater. Chem. A*, 2019, **7**, 6467-6474.

21. F. Bella, G. Griffini, J.-P. Correa-Baena, G. Saracco, M. Grätzel, A. Hagfeldt, S. Turri and C. Gerbaldi, *Science*, 2016, **354**, 203.

22. Y. Wang, Z. Zhang, Y. Lan, Q. Song, M. Li and Y. Song, *Angew. Chem., Int. Ed.*, 2021, **60**, 8673-8677.

23. J. Zhang, H. Luo, W. Xie, X. Lin, X. Hou, J. Zhou, S. Huang, W. Ou-Yang, Z. Sun and X. Chen, *Nanoscale*, 2018, **10**, 5617-5625.

24. R. Garai, M. A. Afroz, R. K. Gupta and P. K. Iyer, *Adv. Sustainable Syst.*, 2020, **4**, 2000078.

25. J. Kim, A. Ho-Baillie and S. Huang, *Solar RRL*, 2019, **3**, 1800302.

26. M. Adil Afroz, N. Ghimire, K. M. Reza, B. Bahrami, R. S. Bobba, A. Gurung, A. H. Chowdhury, P. K. Iyer and Q. Qiao, *ACS Appl. Energy Mater.*, 2020, **3**, 2432-2439.

27. H. Zhang, M. K. Nazeeruddin and W. C. H. Choy, *Adv. Mater.*, 2019, **31**, 1805702.

28. A. R. b. Mohd Yusoff, M. Vasilopoulou, D. G. Georgiadou, L. C. Palilis, A. Abate and M. K. Nazeeruddin, *Energy Environ. Sci.*, 2021, DOI: 10.1039/D1EE00062D.

29. M. Hossain, R. Garai, R. K. Gupta, R. N. Arunagirinathan and P. K. Iyer, *J. Mater. Chem. C*, 2021, DOI: 10.1039/D1TC02335G.

30. R. Wang, J. Xue, L. Meng, J.-W. Lee, Z. Zhao, P. Sun, L. Cai, T. Huang, Z. Wang, Z.-K. Wang, Y. Duan, J. L. Yang, S. Tan, Y. Yuan, Y. Huang and Y. Yang, *Joule*, 2019, **3**, 1464-1477.

31. R. K. Gupta, R. Garai and P. K. Iyer, *ACS Appl. Energy Mater.*, 2021, **4**, 10025-10032.

32. M. Hossain, R. N. Arunagirinathan, R. Garai, R. K. Gupta and P. K. Iyer, *J. Mater. Chem. C*, 2021, DOI: 10.1039/D1TC03852D.

33. S. Zhang, X. Yan, Z. Liu, H. Zhu, Z. Yang, Y. Huang, S. Liu, D. Wu, M. Pan and W. Chen, *J. Energy Chem.*, 2021, **54**, 493-500.

34. L. Wang, M. Shahiduzzaman, E. Y. Muslih, M. Nakano, M. Karakawa, K. Takahashi, K. Tomita, J. M. Nunzi and T. Taima, *Nano Energy*, 2021, **86**, 106135.

35. R. K. Gupta, R. Garai, M. Hossain, A. Choudhury and P. K. Iyer, *ACS Sustainable Chem. Eng.*, 2021, **9**, 7993-8001.

36. M. A. Afroz, R. Garai, R. K. Gupta and P. K. Iyer, *ACS Appl. Energy Mater.*, 2021, DOI: 10.1021/acsaem.1c01205.

37. R. Garai, R. K. Gupta, A. S. Tanwar, M. Hossain and P. K. Iyer, *Chem. Mater.*, 2021, **33**, 5709-5717.

38. J. Xie, P. Hang, H. Wang, S. Zhao, G. Li, Y. Fang, F. Liu, X. Guo, H. Zhu, X. Lu, X. Yu, C. C. S. Chan, K. S. Wong, D. Yang, J. Xu and K. Yan, *Adv. Mater.*, 2019, **31**, 1902543.

39. R. K. Gupta, R. Garai, M. A. Afroz and P. K. Iyer, *J. Mater. Chem. C*, 2020, **8**, 8191-8198.

40. C. Xin, J. Zhang, X. Zhou, L. Ma, F. Hou, B. Shi, S. Pan, B. Chen, P. Wang, D. Zhang, X. Chen, Y. Zhao, A. A. Bakulin, Y. Li and X. Zhang, *ACS Appl. Energy Mater.*, 2020, **3**, 3318-3327.

41. L. Guan, N. Jiao and Y. Guo, *J. Phys. Chem. C*, 2019, **123**, 14223-14228.

42. C. C. Boyd, R. C. Shallcross, T. Moot, R. Kerner, L. Bertoluzzi, A. Onno, S. Kavadiya, C. Chosy, E. J. Wolf, J. Werner, J. A. Raiford, C. de Paula, A. F. Palmstrom, Z. J. Yu, J. J. Berry, S. F. Bent, Z. C. Holman, J. M. Luther, E. L. Ratcliff, N. R. Armstrong and M. D. McGehee, *Joule*, 2020, **4**, 1759-1775.

CHAPTER 6

Surface Recrystallized Stable 2D-3D Graded Perovskite Solar Cells for Efficiency Beyond 21%

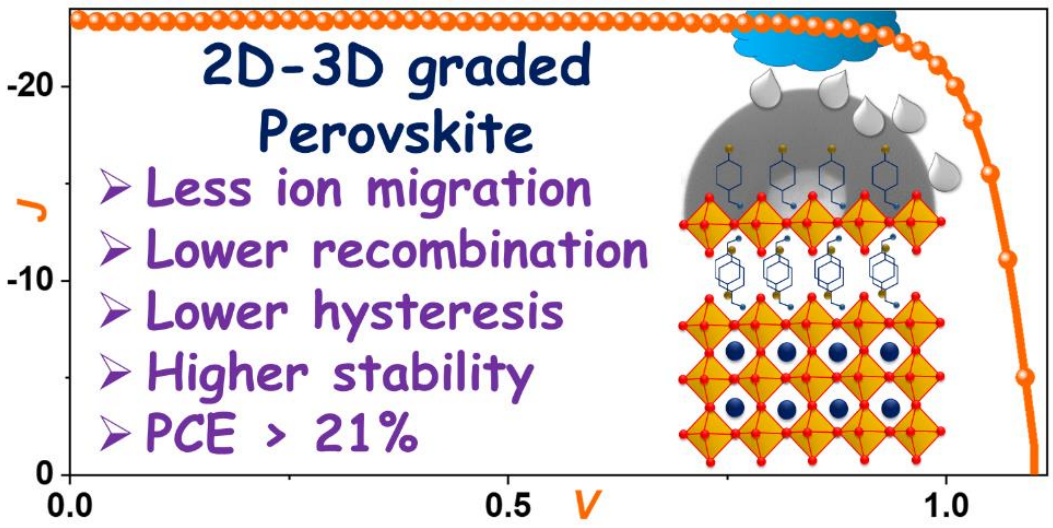

Manuscript: Rabindranath Garai, Ritesh Kant Gupta, Maimur Hossain, Parameswar Krishnan Iyer, "Surface recrystallized stable 2D-3D Graded perovskite solar cells for efficiency beyond 21%", *J. Mater. Chem. A*, 2021. (**doi.org/10.1039/D1TA06901B**)

[This page was intentionally left blank]

Abstract

Recently, organic-inorganic hybrid perovskite solar cells (PSCs) have experienced a rapid growth in terms of efficiency. However, the instability of hybrid perovskite materials towards ambient conditions restricts its commercialization. Formation of a thin layer of 2D perovskite over the 3D structure has now boosted the strategy to improve the perovskite stability. This 2D-3D heterostructure enables improved light harvesting property and enhanced carrier transport of 3D perovskite along with augmented ambient stability due to the capped 2D layer. Herein, we demonstrate the untapped potential of surface recrystallized 2D-3D graded perovskite fabricated with the surface treatment of strategically synthesized multifunctional 4-(aminomethyl)benzoic acid hydrogen bromide (ABHB) molecule. In particular, the bromide ions fill the halide vacancies in the perovskite lattice, while the amine groups and the carboxylic acid functionality significantly minimizes the defect states and reduces the ion migration. Consequently, ABHB treatment delivers outstanding efficiencies of 21.18% (small area device - 0.12 cm^2) and 18.81% (for large area device - 2 cm^2) as well as negligible hysteresis. Furthermore, the capped 2D layer restricts moisture penetration into the perovskite layer because of improved hydrophobicity and significantly enhances the ambient stability of PSCs.

6.1 Overview

Recently, organic-inorganic hybrid perovskites have gained incredible research attention due to their excellent optoelectronic behaviour such as high absorption coefficient, broad light absorption, bandgap tunability, ultralong carrier diffusion length and enhanced carrier mobility.[1-4] From its discovery in 2009, perovskite solar cells (PSCs) have witnessed a rapid growth in terms of power conversion efficiencies (PCEs) from 3.8% to >25% within a few years through constant innovation on material engineering and optimization of device architecture.[1, 5-9] Among all the approaches, surface passivation is one of the most convenient techniques to enhance the stability and efficiency of PSCs, where an ultrathin layer is precisely formed over the three-dimensional (3D) light harvesting perovskite materials that effectively reduces the charge recombination and enhances the carrier transport as well as stability.[7, 10-12] For surface passivation of perovskite, several class of materials have been utilized viz. small organic molecules,[13-16] polymers (conjugated and non-conjugated),[17-20] organic ammonium halide salts,[9, 21, 22] etc.

When the perovskite layer is treated with larger organic ammonium halide salt, a thin two-dimensional (2D) layer is formed over the 3D structure. However, the potential of this 2D-3D graded heterostructure has yet to be fully tapped despite that it has drawn tremendous research interest, since it integrates the advantages of high light absorption and enhanced charge transport of 3D perovskite with the improved stability of 2D capped perovskite. Along with the stability enhancement, a capping layer also passivates the defect states and heals the halide vacancies. Several structural optimizations of the organic ammonium halide salts, such as variation of organic part (n- and iso-butylammonium iodide, phenyl-ethyl-ammonium iodide, benzyl-ammonium iodide, and phenyl-ammonium iodide,),[23-26] variation of halide (benzyl-ammonium chloride, bromide and iodide),[27] incorporation of additional passivation group (5-Ammonium valeric acid iodide, 4-fluoro-phenyl-ethylammoniumiodide),[28, 29]etc. have been attempted to study the effect of 2D-3D graded perovskite. Among all these, the collective effect of incorporating additional passivation groups and halide engineering is almost not explored. However, it is very critical to find a suitable organic ammonium halide salt with appropriate passivation capability.

To address this challenge, 4-(aminomethyl)benzoic acid hydrogen bromide (ABHB) has been synthesized and applied as an organic ammonium halide salt for the fabrication of 2D-3D graded heterostructure. As ABHB molecule has an additional carboxylic passivation

group, it can very efficiently passivate the trap states. Additionally, the bromide ion can effectively heal the iodide vacancies and offers better quality film with improved stability. Consequently, ABHB treated device reveals a high efficiency of 21.18% with a short-circuit current density (J_{SC}) of 23.42 mA-cm^{-2}, an open-circuit voltage (V_{OC}) of 1104.5 mV, and fill factor (FF) of 81.9%. This high PCE is attributed to the high-quality perovskite film with lower trap states. Large area passivated PSCs was also fabricated to demonstrate the scalability of this approach for device commercialization. Further, this ABHB treatment also restricted moisture penetration in the perovskite layer thereby improving the moisture stability of the PSCs.

6.2 Results and Discussions

To investigate the significance of ABHB treatment on the $MAPBI_3$ layer, varied concentration of the molecule was deposited on top of the perovskite film (**Figure 6.1a**). **Figure 6.1b** depicts the deposition technique where varied concentrations of ABHB molecule were dissolved in isopropanol (IPA) and deposited over the perovskite through spin coating method. The X-ray diffraction (XRD) patterns of the as prepared films were analyzed to estimate the effect of ABHB treatment (**Figure 6.1c**). All the samples reveal three signature diffraction peaks at ~14.12°, 28.42°, and 31.12° for (110), (220), and (310) crystal planes, respectively. The diffraction pattern along (110) and (220) plane considerably enhances from pristine to the 2 mg-mL^{-1} ABHB treated perovskite film, signifying enhanced crystallinity concentration. Hence, optimum film crystallinity is obtained for 2 mg-mL^{-1} additive treatment. This treatment can form a thin 2D layer on the top surface of 3D perovskite after recrystallization.[21, 30]

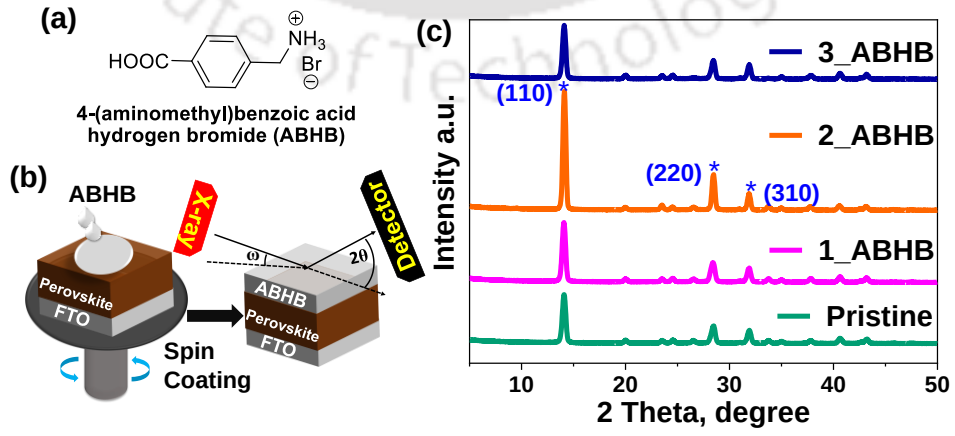

Figure 6.1 (a) Molecular structure of ABHB, (b) Schematic representation of ABHB treatment and depth profile XRD study, (c) XRD patterns of perovskite films with varied concentration of ABHB.

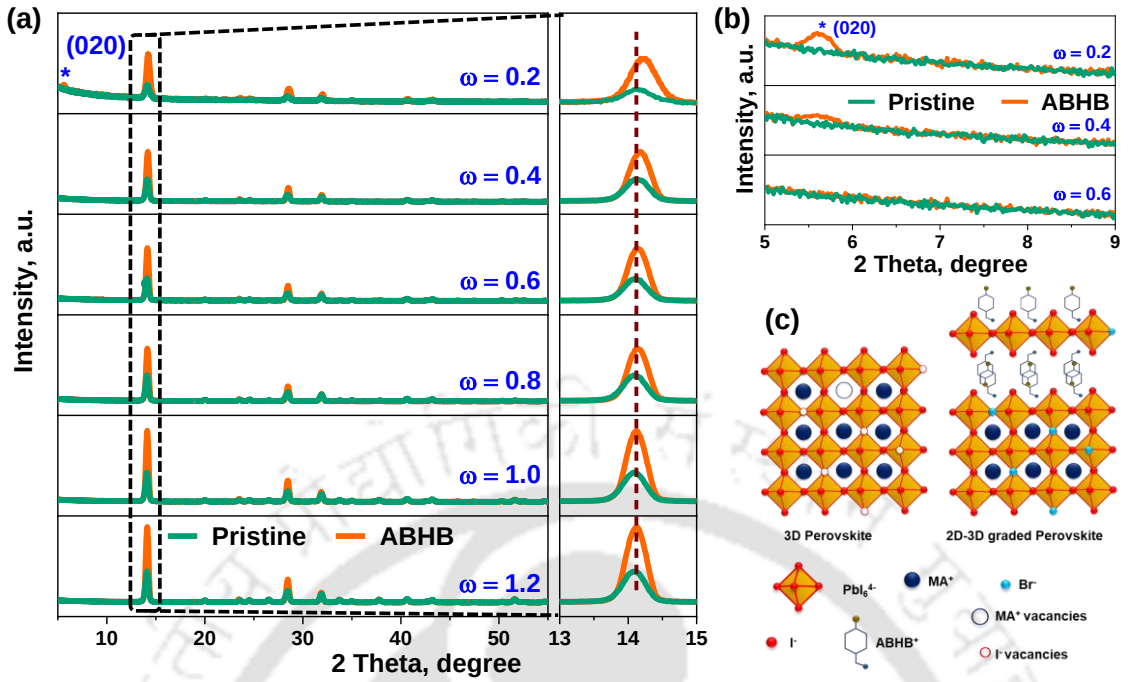

Figure 6.2 (a) XRD depth profile perovskite films at different incident angles, (b) XRD peak of 2D perovskite, and (c) Schematic illustration of traps in 3D perovskite & its passivation in 2D-3D graded heterostructure.

To confirm this, XRD depth profile analysis was performed for both pristine and 2 mg-mL^{-1} ABHB treated films at varying angle of incidence (ω) from 0.2° to 1.2° (**Figure 6.2a**). Perovskite top surface was analyzed at lower ω scan since at higher ω scan the X-ray beam will penetrate deep inside the films. At higher incident angle, the FTO peaks start to appear which suggests that the X-ray beam fully penetrated the films. For all the scans, ABHB treated films exhibit intense diffraction peaks for (110) and (220) planes in comparison to the unmodified film indicating better crystallinity. Again, the ABHB treated film illustrates a diffraction peak ~5.6° for (020) plane in the XRD scans at ω = 0.2° which reduces at ω = 0.4° and disappears at higher ω values (**Figure 6.2b**). This diffraction peak at (020) is for the formation of 2D phase specifying that a thin 2D perovskite layer is being formed over the 3D perovskite after ABHB treatment and resulting in a 2D-3D graded heterostructure. Furthermore, a prominent peak shifting is noticed in the (110) plane to higher 2θ value for the ABHB treated film, especially at lower ω. This is due to the incorporation of Br^- in the perovskite lattice. Usually, the shifting of these peaks to higher 2θ values are very well-known as well as are noticed in previous studies of bromide addition for controlling ion migration.[31] A schematic illustration of defect passivation as well as formation of 2D-3D graded heterostructure has been presented in **Figure 6.2c**. Herein, using appropriate

concentration of ABHB for perovskite treatment yielded the desired 2D layer over the 3D perovskite through surface recrystallization. The bromide ion efficiently fills the iodide vacancies in the treated film and reduces ion migration as well. The amine group facilitates the top 2D layer formation over the 3D perovskite through surface recrystallization. Additionally, the carboxylic acid group can interact with other defects in perovskite layer.[32, 33]

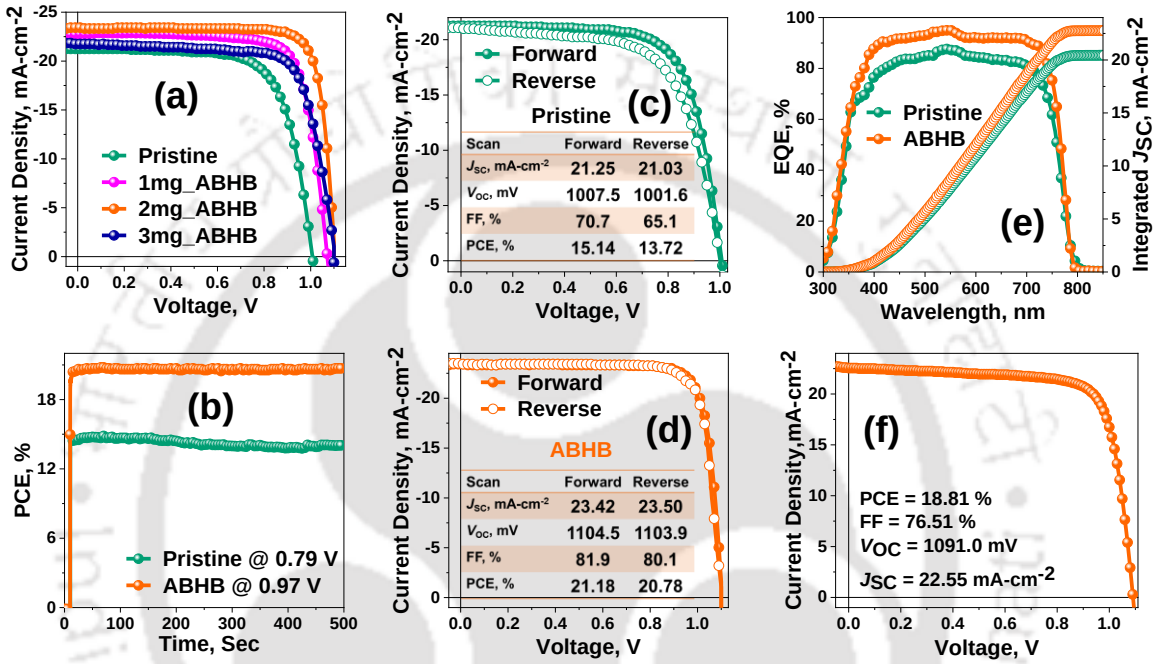

Figure 6.3 (a) *J–V* curves of the devices with various ABHB concentration, (b) Steady state current measured at mpp, (c) Hysteresis of the pristine device, (d) Hysteresis of the ABHB passivated device, (e) EQE curves, and (f) *J–V* curves of ABHB treated large area device.

To explore the effect of ABHB treatment, photovoltaic devices with an architecture of FTO/NiOx/Perovskite layer/$PC_{61}BM$/Rhodamine 101/Ag were fabricated. The current density versus voltage (*J–V*) curves for the champion devices are presented in **Figure 6.3a** and **Table 6.1**. The unmodified device offers a PCE of 15.14% with a FF of 70.7%, V_{OC} of 1007.5mV and J_{SC} of 21.25 mA-cm^{-2}. The PCE as well as all the device parameters are significantly improved with ABHB treatment and the optimum device performance is achieved at 2 mg-mL^{-1}. The champion device displays an improved efficiency of 21.18% with a FF of 81.9%, V_{OC} of 1104.5 mV and J_{SC} of 23.42 mA-cm^{-2}. The steady-state measurement of both pristine and ABHB treated devices carried out to study the illumination stability (**Figure 6.3b**) revealed a stable PCE of ~20.6% for 500 seconds, whereas, the untreated device degraded gradually over time. The pristine and ABHB

devices were measured at both forward (*F*) and reverse (*R*) scans (**Figure 6.3c & d**) to estimate hysteresis index (HI). ABHB device exhibits a negligible hysteresis with a HI of 1.9% as compared to 9.4% to the pristine. This is due to the better-quality perovskite films with lower trap density, reduced recombination and suppressed ion migration. External quantum efficiency (EQE) measurements were also performed where ABHB treated device illustrate better photo response than the pristine (**Figure 6.3e**). The integrated J_{SC} calculated from the EQE spectra is in well agreement with $J-V$ results. To address the challenge of commercialization using this 2D-3D heterostructure approach, large area PSCs devices (2 cm^2) have also been fabricated that revealed high PCE of 18.81% (**Figure 6.3f**) confirming the scalability utilizing this method.

Table 6.1: Photovoltaic parameters of PSCs with different concentration of additives.

Device	J_{SC}, mA-cm^{-2}	V_{OC}, mV	FF, %	PCE, Best (Average), %
Pristine	21.25	1007.5	70.7	15.14 (13.97±0.63)
1_ABHB	22.79	1071.4	76.8	18.75 (17.95±0.55)
2_ABHB	23.42	1104.9	81.9	21.18 (20.32±0.41)
3_ABHB	21.75	1106.4	74.5	17.93 (16.47±0.73)

[a]Average of 15 devices.

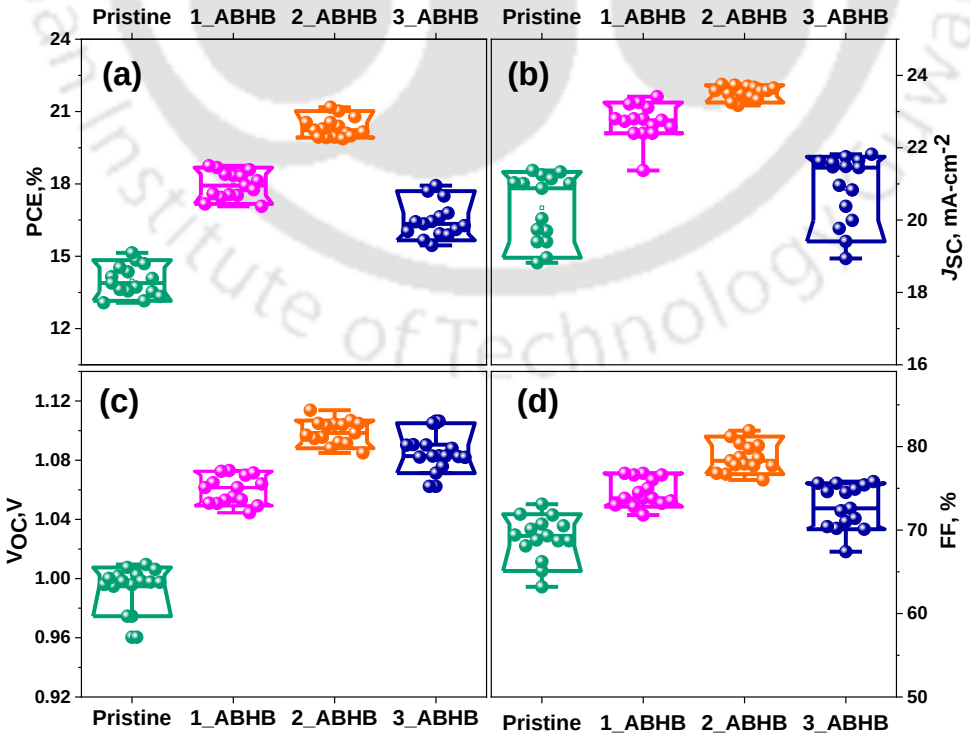

Figure 6.4 Box chart of pristine and different concentration of ABHB modified devices.

To check the repeatability of this process 15 individual cells were fabricated for varied concentration of ABHB treated device and all the device parameters were plotted in the form of box chart (**Figure 6.4**). The optimum concentration (2 mg-mL^{-1}) of ABHB treatment reveals a narrower distribution of device parameters suggesting high reproducibility.

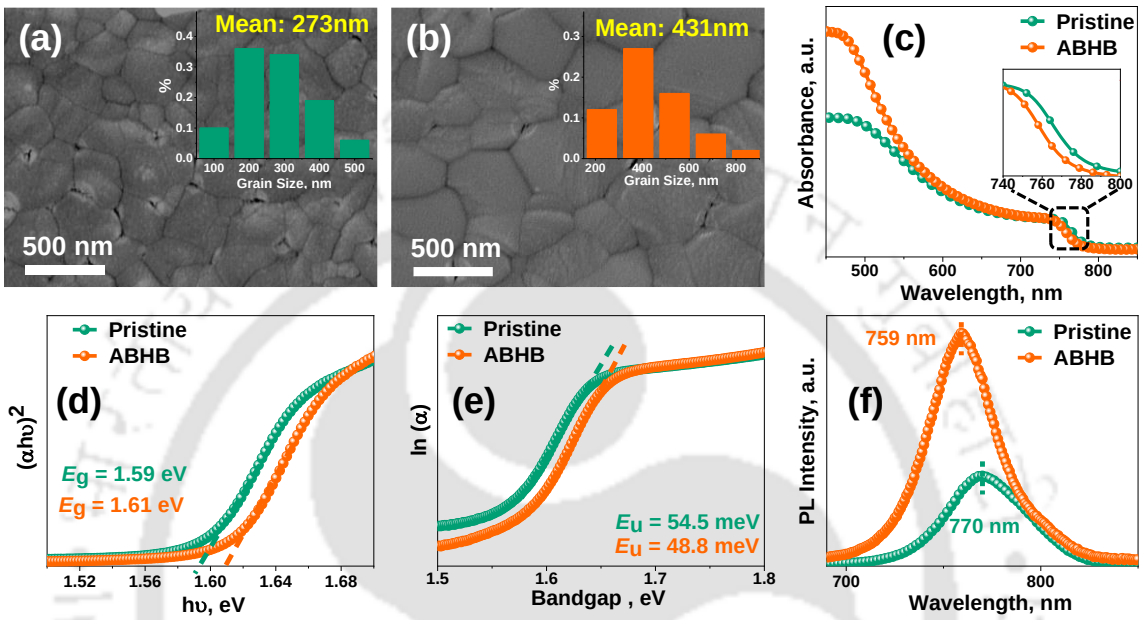

Figure 6.5 Surface FESEM images of (a) Pristine, (b) ABHB passivated films. (c) UV–vis absorption spectra, (d) Tauc plot, (e) Plot of ln(α) versus photon energy, and (f) Steady state PL spectra.

Field emission scanning electron microscope (FESEM) images of the films with and without ABHB treatment (**Figure 6.5a & b)** show that the pristine film exhibits an average grain size of 273 nm which increases up to 431 nm upon ABHB treatment. Compared to pristine, ABHB treatment leads to superior quality perovskite film with reduced grain boundary and better surface coverage which significantly enhances both the FF and absorption as shown in UV-vis spectra (**Figure 6.5c**). This is because of the improved film quality which boosts the light harvesting property and results in higher J_{SC}. However, ABHB treated film gives a blue-shifted absorption due to higher bandgap (E_g) which was confirmed from the Tauc plot (**Figure 6.5d**). This higher bandgap is due to the 2D-3D graded heterostructure as well as the incorporation of bromide ion in perovskite lattice leading to high V_{OC} of the ABHB treated device. For better understanding of the optoelectronic properties and to investigate the trap states Urbach energy (E_u) was estimated from ln(α) versus photon energy plot (**Figure 6.5e**). Pristine film exhibits E_u of 54.5 meV which decreases up to 48.8 meV after ABHB treatment signifying less defect

density as well as band edge disorder. To further confirm the trap passivation, steady-state photoluminescence (PL) of the films were recorded where ABHB treated film reveals higher PL intensity than the pristine film (**Figure 6.5f**). This indicates that the 2D-3D heterostructure can passivate the defect states and lower the nonradiative recombination.[34] PL peak of ABHB treated film experienced a blue shift because of the cumulative effect of trap passivation and bromide ion incorporation in the perovskite lattice.

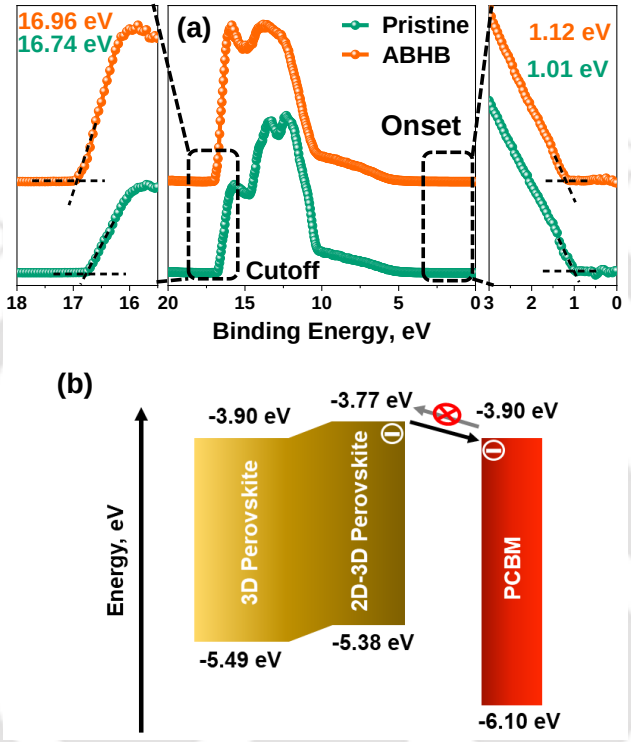

Figure 6.6 (a) UPS analysis of pristine and ABHB treated films. The cutoff (left) and Onset (right) regions of UPS, and (b) Schematic illustration of energy level alignment at the perovskite andPCBM interface.

Furthermore, ultraviolet photoelectron spectroscopy (UPS) was carried out to determine the energy level alignment of perovskite films with and without ABHB treatment (**Figure 6.6a**). The highest occupied molecular orbital (HOMO) & the lowest unoccupied molecular orbital (LUMO) energy levels and the Fermi energy (E_{Fermi}), of perovskite films is estimated from the equations of $E_{Fermi} = (E_{cutoff} - 21.22\ eV)$, $E_{HOMO} = (E_{Fermi} - E_{onset})$, and $E_{LUMO} = (E_{HOMO} + E_g)$. E_{cutoff} and E_{onset} is obtained from the UPS spectra while the E_g was estimated from the Tauc plot (**Figure 6.5d**). After ABHB treatment, all three energy levels reveal a slight upward shift. The obtained energy level diagram (**Figure 6.6b**) reveals the charge transport mechanism from 2D-3D interface to PCBM layer. The continuously uplifted LUMO level of the 2D-3D graded perovskite facilitates easy electron flow towards cathode. It simultaneously blocks the electron backflow from PCBM to perovskite and

mitigate carrier recombination due to increase in energy barrier. Therefore, the ABHB treated device reveals a high V_{OC}.

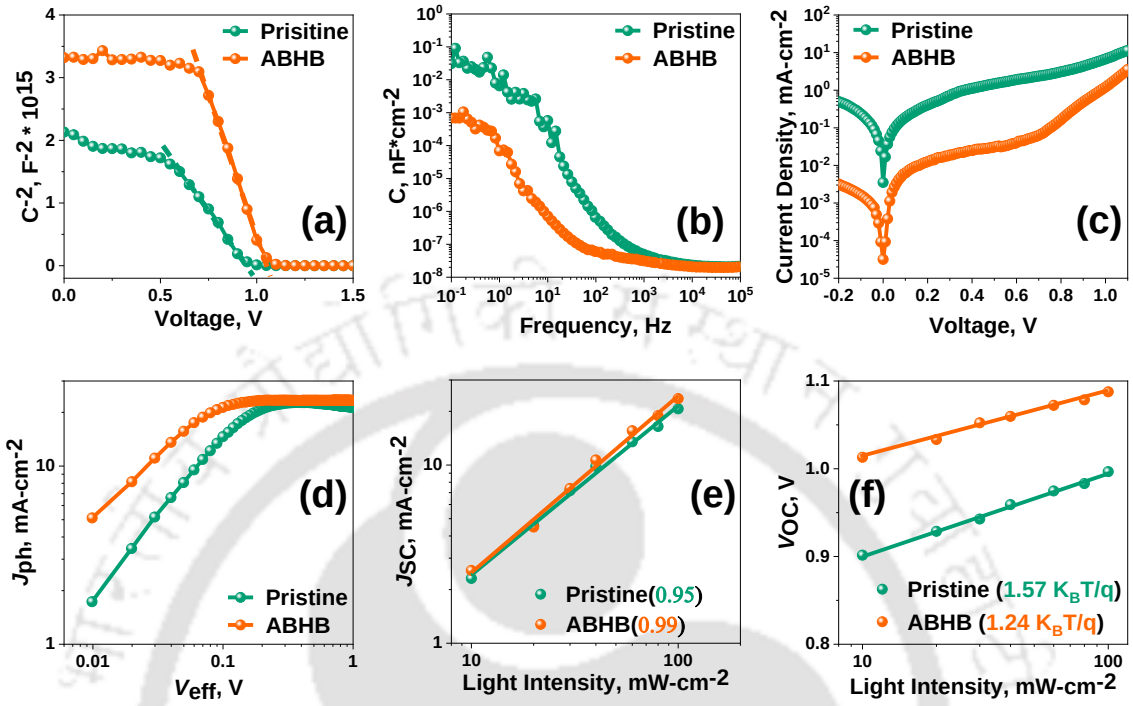

Figure 6.7 (a) Mott–Schottky plots, (b) Variation of C with frequency, (c) Dark *J*–*V* characteristics of the devices with and without ABHB treatment, (d) J_{ph} versus V_{eff} characteristics with double-logarithmic axis for pristine and passivated device, (e) J_{SC} versus light intensity plot, and (f) V_{OC} versus light intensity plot.

For more insight about the interfacial charge carrier dynamics, charge transport and defect passivation, the pristine and ABHB treated devices were characterized with few specific analyses. Carrier extraction at the device interface was studied with Mott–Schottky (MS) analysis, from which built-in potential (V_{bi}) and interfacial charge density (N) can be calculated (**Figure 6.7a**). ABHB treated devices reveal higher V_{bi} value of 1.06V than the pristine device (0.93V) which leads to better V_{OC}. The pristine device reveals an N value of 6.81×10^{16} cm^{-3} which decreases to 3.17×10^{16} cm^{-3} after ABHB treatment. A reduced N indicates lower accumulation of charges at the interface because of effective charge extraction.[35] The capacitance–frequency (C–*f*) analysis discloses that at low-frequency region, ABHB treated device exhibit a lesser electrode polarization which further signifies better interfacial charge transport (**Figure 6.7b**).[36] This leads to improved J_{SC} and reduced hysteresis of the ABHB treated device. Moreover, dark *J*-*V* measurements were performed to have better understanding about the charge transport behaviour (**Figure 6.7c**). ABHB treated device exhibits a lower leakage current along with a decreased reverse saturation current resulting in lesser charge recombination and enhanced carrier transport.

Figure 6.7d shows photocurrent density (J_{ph}) versus effective voltage (V_{eff}) plot, where J_{ph} is the current density variation between dark and light and V_{eff} is the variation between the applied voltage and the voltage at which J_{ph} = 0. At lower and higher (saturation region) V_{eff} region, J_{ph} is higher for the ABHB treated device which signifies enhanced generation rate and results in improved J_{SC}. **Figure 6.7e** represents J_{SC} measurements with respect to light intensity where the slope is near to unity for the ABHB treated device indicating better carrier transport due to lower recombinational loss. **Figure 6.7f** revealed V_{OC} versus light intensity plot and can provide important understanding about charge recombination mechanism.[37] The obtained slopes for the pristine and ABHB treated devices were 1.57K_BT/q and 1.24K_BT/q, respectively (where K_B, T, and q are Boltzmann constant, absolute temperature and elementary charge). ABHB treated device exhibits an ideality factor closer to one whereas the pristine device reveals a higher value. From this result it can be said that recombination is largely suppressed for the ABHB treated device.

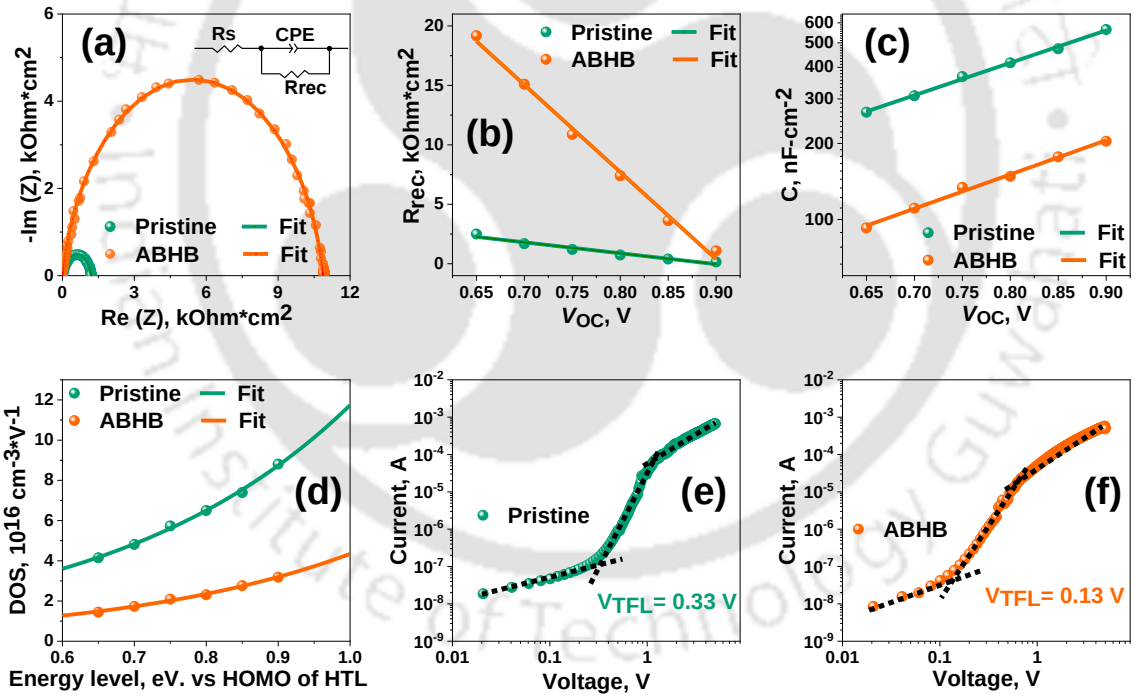

Figure 6.8 (a) Nyquist plots of the devices with and without ABHB. (b) Rrec variation with different bias, (c) Variation of C with variable bias, and (d) Trap density of states (DOS) versus electron energy level. (e,f) Dark *J*–*V* characteristics from hole-only devices of pristine and ABHB modified device respectively.

Impedance spectroscopy (IS) was performed to study about the charge recombination. Nyquist plots at various biases were taken for pristine and ABHB treated device. The curve obtained at 0.75 V reveals as a representative and all the curves were fitted with a corresponding circuit presented in the inset (**Figure 6.8a**). The changes of recombination

resistance (*R*rec) with applied bias, as revealed in **Figure 6.8b**, disclose that ABHB treated device exhibits a higher *R*rec than the pristine device. This signifies ABHB treatment can effectively suppress the charge recombination due to reduced defect states and better charge transfer ability. **Figure 6.8c** illustrates capacitance (C) versus applied bias plot where pristine device shows a higher capacitance than the modified device. Hence, probability of charge trapping is lesser for ABHB treated device. Further, trap density states (*t*-DOS) has been derived from the *C* versus applied bias plot (**Figure 6.8d**).[33] In contrast to pristine, modified device has lower *t*-DOS with narrower distribution which can be well co-related with the results attained from the E_u calculation. Further, to obtain an exact measure of trap states (N_t), hole-only devices were fabricated with and without ABHB treatment and corresponding dark *J*–*V* characteristics are represented (**Figure 6.8e & f**). The pristine device exhibits a higher N_t of 7.99×10^{15} cm^{-3} than ABHB treated device of 3.14×10^{15} cm^{-3}. Consequently, it is evident that the ABHB treated 2D-3D layer can significantly decrease the trap states in perovskite and enhance the PSC device performance.

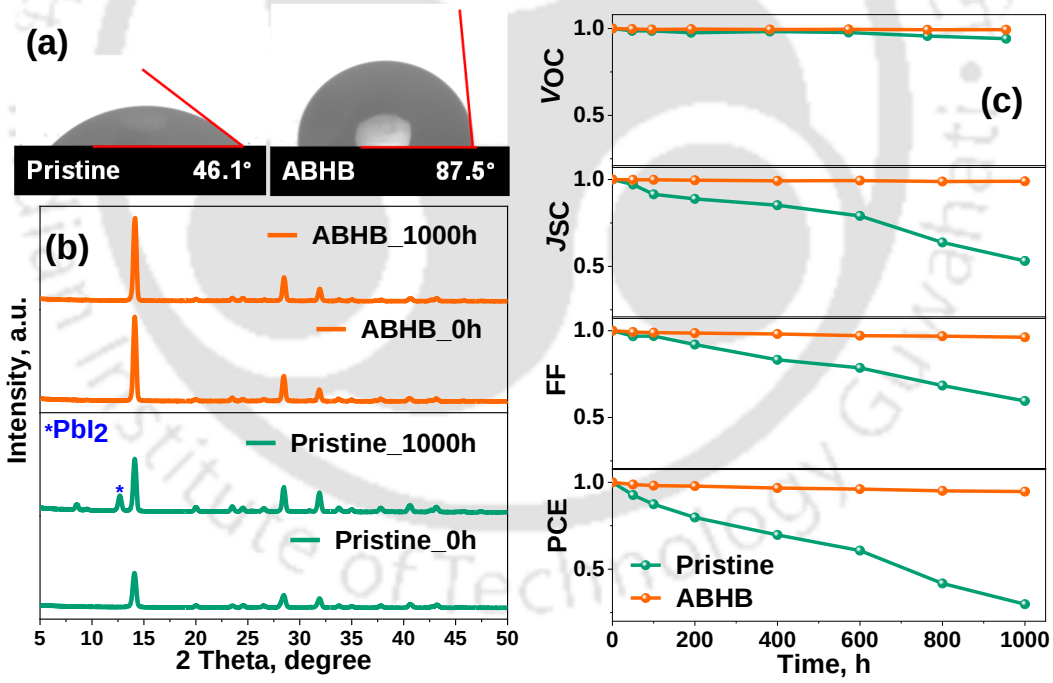

Figure 6.9 (a) Contact angle measurement of pristine and ABHB treated films, (b) XRD patterns of perovskite films aged in a relative humidity of 40–50%., and (c) Normalized V_{OC}, J_{SC}, FF and efficiency of pristine and ABHB modified devices aged at room temperature at a relative humidity of 40–50%.

Along with trap passivation and efficiency improvement, the upper 2D layer can efficiently restrict the moisture penetration into the lattice of perovskite. To verify this, contact angle measurement has been carried out where ABHB treated film reveals improved hydrophobicity with a higher contact angle of 87.5° than the pristine one with contact angle

of 46.1° (**Figure 6.9a**). The stability of the films was further analyzed with XRD measurement where the films were stored at 40-50% relative humidity for thousand hours (**Figure 6.9b**). After aging, the XRD pattern of the ABHB treated film remains unchanged whereas, a strong peak for PbI_2 phase (degraded phase) appears for the pristine film. To validate these results, device stability was measured in similar environment (**Figure 6.9c**). For ABHB treated device, all the device parameters (J_{SC}, V_{OC} and FF) exhibit almost negligible changes. Although, V_{OC} remains nearly constant for the pristine device, all other device parameters start to degrade rapidly over time. Consequently, ABHB treated device retains ~95% of its initial efficiency, on the contrary, pristine device retains only ~30%. This incredible enhancement of ambient stability upon ABHB treatment is due to the formation of the 2D layer over 3D perovskite.

6.3 Conclusions

In summary, a facile and highly effective dimensionality engineering strategy, has been established through which a 2D-3D graded heterostructure has been formed with improved surface morphology after precise treatment with ABHB. The amine and carboxylic acid groups effectively decrease the trap states while the bromide ions fill the halide vacancies by incorporating into the perovskite lattice. This 2D-3D perovskite efficiently minimizes carrier recombination, offers enhanced charge transport and higher generation rate. Consequently, the ABHB treated devices disclose outstanding efficiencies up to 21.18% (0.12 cm^2) and 18.81% (2 cm^2). Further, the devices with 2D layer on top showed improved stability in ambient conditions due to better hydrophobicity. This method thus provides deeper insights into the dimensionality engineering strategy to develop 2D-3D graded perovskite for achieving high performance and stable photovoltaic devices as well as it has the potential to address the challenge of economical scalability.

6.4 Experimental Section

Materials: FTO glass substrates (13 Ω sq^{-1}), PbI_2 (99.8%), all solvents like DMF (anhydrous, 99.8%), DMSO (anhydrous, 99.8%), Toluene (anhydrous, 99.8%), Chlorobenzene were procured from Sigma-Aldrich. MAI was purchased from Dyesol. Nickel nitrate hexahydrate ($Ni(NO_3)_2 \cdot 6H_2O$) was fobtained from TCI. All other chemicals were used as received.

Synthesis of ABHB: For the synthesis, 1 equivalent of 4-(aminomethyl)benzoic acid was dissolved in ethanol and placed it in ice bath. After that under vigorous stirring condition, hydrogen bromide (1.1 equivalent) was added slowly into the solution. To ensure completion of the reaction, the solution was stirred overnight. Then the solvent was removed from the reaction mixture by rotary evaporator and resulting solid was washed with diethyl ether several times. The white solid was further purified by recrystallization in mixed solvent of methanol and diethyl ether. Finally, the white crystalline solid was filtered and dried under vacuum (yield ~90%). The resulting compound is named as of 4-(aminomethyl)benzoic acid hydrogen bromide (ABHB).

Device Fabrication: NiO_x precursor solution was prepared by dissolving 1M Nickel nitrate hexahydrate and 1M Ethylenediamine in 1ml Ethylene Glycol. Then the NiO_x layer was coated as hole transporting layer on the cleaned FTO. The cleaning process was started with detergent and followed by deionized water, acetone, and isopropyl alcohol for 15 min for each solvent, then dried and treated with UV-ozone for half an hour. NiO_x precursor solution was spin coated onto the FTO substrates @3000 rpm for 40 sec. Afterward the substrates were post-annealed at 300 °C for 60 min in ambient air. The $MAPbI_3$ precursor solution was prepared in a glovebox by dissolving MAI and PbI_2 (1:1 ratio) in a mixed solvent of gamma-Butyrolactone and DMSO (7:3, v/v) where the concentration of Pb^{2+} was 1.26. The solution was heated overnight and filtered with the 0.45 μm filter prior to spin coating. The filtered precursor solution was spin coated on the NiO_x coated FTO in a two-step spin coating process i.e. 750 rpm for 20 sec and 4000 rpm for 60 sec. In the second step 160 ml anhydrous Toluene was dripped after 20 sec as antisolvent and after that the substrates were annealed @80° C for 10 min. Above the perovskite layer different concentration (1, 2 & 3 mg-mL^{-1}) of ABHB solution (in isopropanol solvent) was spin coated at 4000 rpm for 30 sec. Then the ABHB treated perovskite film was further annealed at 80° C for 5 min. After this, 12 mg/ml PCBM solution was coated @1200 rpm as ETL and again annealed @80° C for 5 min. After that a thin layer of Rhodamine 101 inner salt (0.5 mg/ml) was spin coated @4000 rpm. Finally, Ag was thermally deposited by using a shadow mask to yield an active area of 0.12 cm^2. The area for the large area device was 2 cm^2.

Device Characterization: The perovskite blend films were characterized by UV-vis absorption spectroscopy (Perkin Elmer Lambda-35), IR spectroscopy (LabRam HR). The XRD patterns of the samples were recorded using a Rigaku Micromax-007HF

diffractometer equipped with Cu Kα1 irradiation (λ = 1.54184 Å). The morphology of the samples was investigated by scanning electron microscopy (SEM, Hitachi S-4800) and AFM (Oxford, Cypher). The current density−voltage (*J*−*V*) characteristic curves were measured using a Keithley 2400 source meter under argon atmosphere by illuminating the device with a solar simulator (AM 1.5G, 100 mW cm^{-2}, Oriel Sol 3A solar simulator, Newport). The incident external quantum efficiency (EQE) was obtained by using an Oriel IQE-200 instrument under ambient condition. Electrochemical measurements were performed with a CH Instruments 760D. Ultraviolet photoemission spectroscopy (UPS) was measured using a Thermo Fisher Scientific UPS spectrometer (ESCALAB Xi^{+}.

References

1. B. Saparov and D. B. Mitzi, *Chem. Rev.*, 2016, **116**, 4558-4596.
2. Z. Xiao, C. Bi, Y. Shao, Q. Dong, Q. Wang, Y. Yuan, C. Wang, Y. Gao and J. Huang, *Energy Environ. Sci.*, 2014, **7**, 2619-2623.
3. G. Xing, N. Mathews, S. Sun, S. S. Lim, Y. M. Lam, M. Grätzel, S. Mhaisalkar and T. C. Sum, *Science*, 2013, **342**, 344.
4. W. Nie, H. Tsai, R. Asadpour, J.-C. Blancon, A. J. Neukirch, G. Gupta, J. J. Crochet, M. Chhowalla, S. Tretiak, M. A. Alam, H.-L. Wang and A. D. Mohite, *Science*, 2015, **347**, 522.
5. A. Kojima, K. Teshima, Y. Shirai and T. Miyasaka, *J. Am. Chem. Soc.*, 2009, **131**, 6050-6051.
6. National Renewable Energy Laboratory, Best research-cell efficiencies chart, https://www.nrel.gov/pv/assets/pdfs/best-research-cell-efficiencies.20200104.pdf, (accessed 24.04.2021).
7. E. H. Jung, N. J. Jeon, E. Y. Park, C. S. Moon, T. J. Shin, T.-Y. Yang, J. H. Noh and J. Seo, *Nature*, 2019, **567**, 511-515.
8. N. J. Jeon, J. H. Noh, W. S. Yang, Y. C. Kim, S. Ryu, J. Seo and S. I. Seok, *Nature*, 2015, **517**, 476-480.
9. Q. Jiang, Y. Zhao, X. Zhang, X. Yang, Y. Chen, Z. Chu, Q. Ye, X. Li, Z. Yin and J. You, *Nat. Photonics*, 2019, **13**, 460-466.
10. X. Feng, R. Chen, Z.-A. Nan, X. Lv, R. Meng, J. Cao and Y. Tang, *Adv. Sci.*, 2019, **6**, 1802040.
11. G. Grancini, C. Roldán-Carmona, I. Zimmermann, E. Mosconi, X. Lee, D. Martineau, S. Narbey, F. Oswald, F. De Angelis, M. Graetzel and M. K. Nazeeruddin, *Nat. Commun.*, 2017, **8**, 15684.
12. F. Tan, H. Tan, M. I. Saidaminov, M. Wei, M. Liu, A. Mei, P. Li, B. Zhang, C.-S. Tan, X. Gong, Y. Zhao, A. R. Kirmani, Z. Huang, J. Z. Fan, R. Quintero-Bermudez, J. Kim, Y. Zhao, O. Voznyy, Y. Gao, F. Zhang, L. J. Richter, Z.-H. Lu, W. Zhang and E. H. Sargent, *Adv. Mater.*, 2019, **31**, 1807435.
13. M. Abdi-Jalebi, M. Ibrahim Dar, S. P. Senanayak, A. Sadhanala, Z. Andaji-Garmaroudi, L. M. Pazos-Outón, J. M. Richter, A. J. Pearson, H. Sirringhaus, M. Grätzel and R. H. Friend, *Sci. Adv.*, 2019, **5**, eaav2012.
14. P. Guo, Q. Ye, X. Yang, J. Zhang, F. Xu, D. Shchukin, B. Wei and H. Wang, *J. Mater. Chem. A*, 2019, **7**, 2497-2506.
15. X. Wu, L. Zhang, Z. Xu, S. Olthof, X. Ren, Y. Liu, D. Yang, F. Gao and S. Liu, *J. Mater. Chem. A*, 2020, **8**, 8313-8322.
16. M. Hossain, R. Garai, R. K. Gupta, R. Narasimhan and P. K. Iyer, *J. Mater. Chem. C*, 2021, DOI: 10.1039/D1TC02335G.
17. X. Wen, J. Wu, M. Ye, D. Gao and C. Lin, *Chem. Commun.*, 2016, **52**, 11355-11358.
18. L.-B. Huang, P.-Y. Su, J.-M. Liu, J.-F. Huang, Y.-F. Chen, S. Qin, J. Guo, Y.-W. Xu and C.-Y. Su, *J. Power Sources*, 2018, **378**, 483-490.

19. M. Li, X. Yan, Z. Kang, Y. Huan, Y. Li, R. Zhang and Y. Zhang, *ACS Appl. Mater. Interfaces*, 2018, **10**, 18787-18795.

20. M. Kim, S. G. Motti, R. Sorrentino and A. Petrozza, *Energy Environ. Sci.*, 2018, **11**, 2609-2619.

21. Y. Lv, Y. Shi, X. Song, J. Liu, M. Wang, S. Wang, Y. Feng, S. Jin and C. Hao, *ACS Appl. Mater. Interfaces*, 2018, **10**, 31755-31764.

22. Q. He, M. Worku, L. Xu, C. Zhou, H. Lin, A. J. Robb, K. Hanson, Y. Xin and B. Ma, *ACS Appl. Mater. Interfaces*, 2020, **12**, 1159-1168.

23. D. Lin, T. Zhang, J. Wang, M. Long, F. Xie, J. Chen, B. Wu, T. Shi, K. Yan, W. Xie, P. Liu and J. Xu, *Nano Energy*, 2019, **59**, 619-625.

24. Y. Cho, A. M. Soufiani, J. S. Yun, J. Kim, D. S. Lee, J. Seidel, X. Deng, M. A. Green, S. Huang and A. W. Y. Ho-Baillie, *Adv. Energy Mater.*, 2018, **8**, 1703392.

25. P. Chen, Y. Bai, S. Wang, M. Lyu, J.-H. Yun and L. Wang, *Adv. Funct. Mater.*, 2018, **28**, 1706923.

26. F. S. Ghoreishi, V. Ahmadi, R. Poursalehi, M. SamadPour, M. B. Johansson, G. Boschloo and E. M. J. Johansson, *J. Power Sources*, 2020, **473**, 228492.

27. H.-C. Chen, J.-M. Lan, H.-L. Hsu, C.-W. Li, T.-S. Shieh, K.-T. Wong and C.-P. Chen, *Mater. Chem. Front.*, 2021, **5**, 3378-3387.

28. N. Wei, Y. Chen, Y. Miao, T. Zhang, X. Wang, H. Wei and Y. Zhao, *J. Phys. Chem. Lett.*, 2020, **11**, 8170-8176.

29. X. Jiang, S. Chen, Y. Li, L. Zhang, N. Shen, G. Zhang, J. Du, N. Fu and B. Xu, *ACS Appl. Mater. Interfaces*, 2021, **13**, 2558-2565.

30. L. Lin, J. T.-W. Wang, T. W. Jones, M. Grigore, A. Cook, D. W. deQuilettes, R. Brenes, B. C. Duck, K. F. Anderson, N. W. Duffy, B. Wenger, V. Bulović, J. Pu, J. Li, B. Chi, H. J. Snaith and G. J. Wilson, *J. Mater. Chem. A*, 2019, **7**, 25511-25520.

31. R. K. Gupta, R. Garai, M. Hossain, A. Choudhury and P. K. Iyer, *ACS Sustainable Chem. Eng.*, 2021, **9**, 7993-8001.

32. R. Garai, R. K. Gupta, A. S. Tanwar, M. Hossain and P. K. Iyer, *Chem. Mater.*, 2021, **33**, 5709–5717.

33. R. Garai, M. A. Afroz, R. K. Gupta and P. K. Iyer, *Adv. Sustainable Syst.*, 2020, **4**, 2000078.

34. J.-W. Lee, Z. Dai, T.-H. Han, C. Choi, S.-Y. Chang, S.-J. Lee, N. De Marco, H. Zhao, P. Sun, Y. Huang and Y. Yang, *Nat. Commun.*, 2018, **9**, 3021.

35. J. Xie, P. Hang, H. Wang, S. Zhao, G. Li, Y. Fang, F. Liu, X. Guo, H. Zhu, X. Lu, X. Yu, C. C. S. Chan, K. S. Wong, D. Yang, J. Xu and K. Yan, *Adv. Mater.*, 2019, **31**, 1902543.

36. O. Almora, C. Aranda, E. Mas-Marzá and G. Garcia-Belmonte, *Appl. Phys. Lett.*, 2016, **109**, 173903.

37. R. K. Gupta, R. Garai, M. A. Afroz and P. K. Iyer, *J. Mater. Chem. C*, 2020, **8**, 8191-8198.

CHAPTER 7

Summary and Prospects

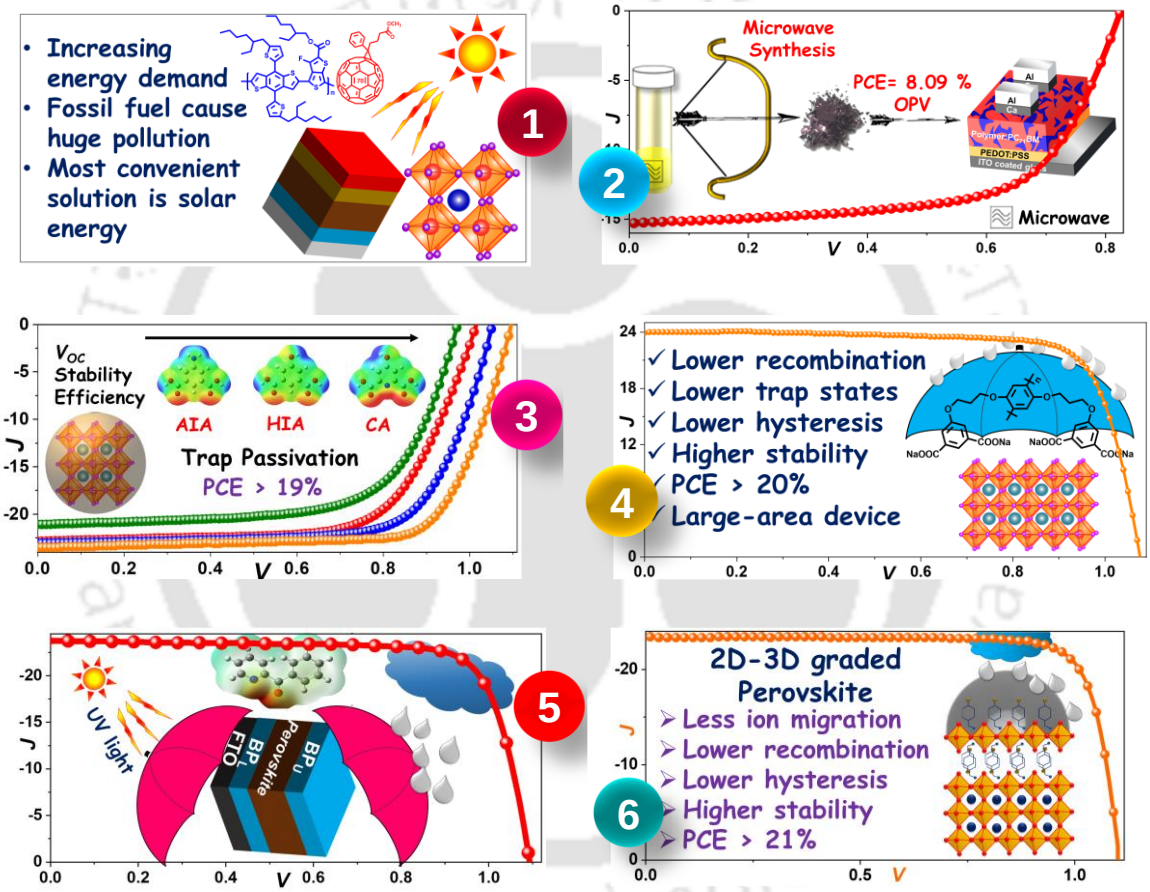

[This page was intentionally left blank]

7.1 Summary

The global energy need is rising exponentially day by day and also the conventional energy sources finishing rapidly. This has become a burning question for the modern world. Furthermore, the depletion of fossil fuels leads to global warming severe climate change. Therefore, it is very important to develop cost-effective, clean, and efficient alternate energy sources. Solar energy is the most promising competitor of fossil fuels to overcome the present energy needs. OSCs and PSCs have become one of the most important photovoltaic technologies in terms of efficiency and commercialization. This thesis was focused on the material engineering of OSCs and PSCs. The first part of the thesis revealed the development of a new technique to synthesize materials for OSCs. The second part of the thesis was demonstrated the effect of several multi-functional molecules as passivation additives for perovskite solar cells. The details investigation about crystallization process, grain growth of perovskite, trap states, ion migration as well as device stability was investigated thoroughly.

The first chapter of this thesis discussed about the increasing global energy need, requirement of solar energy, some important device parameters to measure the performance of any solar cell. Then a brief history of OSCs and PSCs development, their device architecture, different components, and working principle was explained. Finally, engineering OSCs and PSCs was presented.

In the second chapter, the microwave synthesis of a well-known conjugated polymer PTB7-Th with high molecular weight and low dispersity was performed. A detailed investigation of optoelectronic property and device performance was presented with respect to the structure property relationship of polymers.

The third Chapter demonstrated the effect of multifunctional molecules on the crystallization and grain growth of perovskite. The grain growth of perovskite, film morphology and trap passivation capacity were explored in details. Thermal and long-term ambient stability after passivation was also studied carefully.

The fourth Chapter revealed the effect of conjugated polyelectrolyte for perovskite passivation by comprehensive analysis of perovskite film and devices. The expediency of this approach for large scale commercialization was checked by fabrication large area device. Finally. the stability of the passivated device in varied conditions were investigated thoroughly.

In the fifth chapter, the effect of triple passivation technique was demonstrated on the perovskite passivation as well as UV and ambient stabilization. The function of each passivation layer was studied carefully for clear understanding. Lastly. the stability studies of the triple passivated device under UV irritation and ambient condition were examined systematically.

Finally, chapter six elucidated the fabrication of 2D-3D graded perovskite for improved device efficiency and stability. A detailed analysis of the film morphology, trap passivation, device stability in the 2D-3D graded heterostructure was investigated meticulously.

7.2 Prospects

In last few decades, several studies have been carried out on molecular engineering of donor and acceptor materials to solve many issues in terms of achieving high performance OSCs. Polymers with optimal Mw and lower Đ is required for highly efficient OSCs. The synthesis of these polymers is time consuming, and complicated. The quick microwave synthesis can be an inexpensive method to develop other highly efficient donor polymers of high quality in large scale. This technique can also be utilized for the large-scale synthesis of acceptor materials to fabricate highly efficient OSCs to further reduce the cost of the device.

PSCs have demonstrated a record PCE enhancement within a very quick time because of its outstanding optoelectronic properties. However, PSCs suffers from substantial instability under UV irradiation and humid condition which restricts its practical application. Utilization of proper passivation molecules with suitable functional groups can reduce the defect states in perovskite and offer high quality perovskite films. Conjugated polyelectrolytes have been rarely employed for the bulk passivation of perovskite. Thus, the trap passivation effect of these materials can also study for better insight into the stability and efficiency improvement of the devices. Moreover, a strategical multi-layer passivation can be utilized for the lamination of perovskite to stabilize the device from moisture and UV illumination. However, the ambient stability can be further improved by the use of large size cation to form fully 2D or 2D-3D graded perovskites. More insights are required to understand the interaction of these large cations in perovskite crystal to increase the stability. The charge-carrier kinetics of the low dimensional perovskites can be further studied to understand the role of these large cations in improving the device performance. This will allow simultaneous enhancement of PCE and operation stability of

the solar cell devices. Finally, investigation and development of other materials used in the fabrication of perovskites (including the transport layers) and for sealing/encapsulation should establish a significant step towards overall long-term stability.

Lead toxicity is one of the other threats in commercialization of the lead-based perovskite solar cells. Although, there is possibility to use tin-based perovskites, but their stability and efficiency is far behind the lead-based perovskites. Some additives (SnF_2, $SnCl_2$, organics small molecules, etc) are being utilized to improve the stability of tin-based perovskites, but the results are not promising enough to be considered for commercial application. Further device engineering for trap passivation of tin-based perovskites might improve the efficiency and stability of these Pb-free PSCs.

The commercialization of both OSCs and PSCs require the fabrication of large-area devices and modules. Thus, the device engineering developed through this thesis can be merged with the various printing techniques like inkjet printing or doctor-blading or spray coating to develop large-area solar cell devices/modules.

In summary, the work demonstrated in this thesis reveals the strategy to synthesis donor polymer for large scale commercialization in very quick time. It also illustrates various approaches to obtain high quality perovskite films with more surface coverage, less grain boundaries, large grains, and diminished trap states. These strategies were planned to improve the device performances as well as stability of solar cells. I firmly believe that the advances presented in this thesis will motivate the future researchers to contribute towards highly efficient and stable solar cells.

[This page was intentionally left blank]

Outcomes

Publications

1. **Rabindranath Garai**, Ritesh Kant Gupta, Maimur Hossain, Parameswar Krishnan Iyer, "Surface recrystallized stable 2D-3D Graded perovskite solar cells for efficiency beyond 21%", *J. Mater. Chem. A*, 2021, **9**, 26069-26076.
2. **Rabindranath Garai**, Ritesh Kant Gupta, Anwesha Choudhury, Parameswar Krishnan Iyer, "Triple Passivation Approach to Laminate Perovskite Layer for UV and Ambient Stable Photovoltaics". (Under revision)
3. **Rabindranath Garai**, Ritesh Kant Gupta, Arvin Sain Tanwar, Maimur Hossain, Parameswar Krishnan Iyer, "Conjugated Poly-electrolyte Passivated Stable Perovskite Solar Cells for Efficiency Beyond 20%." *Chem. Mater.*, 2021, **33**, 5709–5717
4. **Rabindranath Garai**, Mohammad Adil Afroz, Ritesh Kant Gupta, Parameswar Krishnan Iyer, "Efficient Trap Passivation of $MAPbI_3$ via Multifunctional Anchoring for High-Performance and Stable Perovskite Solar Cells." *Adv. Sustainable Syst.* 2020, **4**, 2000078.
5. **Rabindranath Garai**, Mohammad Adil Afroz, Ritesh Kant Gupta, Anwesha Choudhury, Parameswar Krishnan Iyer, "Quick and Energy Efficient Synthesis of PTB7-Th through Closed Microwave Reactor for High-performance Polymer Solar Cells." *ACS Omega*, 2020, **5**, 2747-2754.
6. Ritesh Kant Gupta, **Rabindranath Garai**, Parameswar Krishnan Iyer, "Dual-passivation Strategy for Improved Ambient Stability of Perovskite Solar Cells". *ACS Appl. Energy Mater.*, 2021, **4**, 10025-10032.
7. Ritesh Kant Gupta, **Rabindranath Garai**, Parameswar Krishnan Iyer, "Ambient Stable Perovskite Solar Cell through Trifluoro Acetic Acid-mediated Multifunctional Anchoring". *ACS Appl. Energy Mater.* 2022, 1571–1579.
8. Mohammad Adil Afroz, **Rabindranath Garai**, Ritesh Kant Gupta, Parameswar Krishnan Iyer, "Benzene Carboxylic Acid Derivative Assisted Passivation of Perovskites for Stable and High-Performance Inverted Perovskite Solar Cells". 2021, *ACS Appl. Energy Mater.* 2021, *4*, 10468–10476.
9. Maimur Hossain, **Rabindranath Garai**, Rahul Narasimhan Arunagirinathan, Mohammad Adil Afroz, Parameswar Krishnan Iyer, "Enhancement of efficacy and ambient stability via circumventing morphological disorder in polymer solar cells by

the incorporation of fluorinated phenyl derivatives." *ACS Appl. Polym. Mater.*, 2021, **3**, 10, 5216–5223.

10. Ritesh Kant Gupta, **Rabindranath Garai**, Maimur Hossain, Anwesha Choudhury, Parameswar Krishnan Iyer, "Halide Engineering for Mitigating Ion Migration and Defect-States in Hot-Cast Perovskite Solar Cells." *ACS Sustainable Chem. Eng.* 2021, **9**, 7993-8001.
11. Ritesh Kant Gupta, **Rabindranath Garai**, Maimur Hossain, Mohammad Adil Afroz, Dibashmani Kalita, Parameswar Krishnan Iyer, "Engineering Polymer Solar Cells: Advancement in Active Layer Thickness and Morphology." *J. Mater. Chem. C*. 2021, **9**, 8746-8775.
12. Maimur Hossain, **Rabindranath Garai**, Ritesh Kant Gupta, Rahul Narasimhan Arunagirinathan, Parameswar Krishnan Iyer, "Fluoroarene Derivative based Passivation of Perovskite Solar Cell Exhibiting Excellent Ambient and Thermo-Stability Achieving Efficiency > 20%." *J. Mater. Chem. C*, 2021, **9**, 10406-10413.
13. Ritesh Kant Gupta, **Rabindranath Garai**, Mohammad Adil Afroz, Parameswar Krishnan Iyer, "Regulating Active Layer Thickness and Morphology for High Performance Hot-casted Polymer Solar Cell." *J. Mater. Chem. C*, 2020, **8**, 8191-8198.
14. Anwesha Choudhury, Ritesh Kant Gupta, **Rabindranath Garai**, Parameswar Krishnan Iyer, "Tuning Polymer Semiconductor Morphology through Additive Engineering for Stable Phototransistor". *ACS Appl. Electron. Mater.* 2021, **3**, 5393–5401.
15. Maimur Hossain, Rahul Narasimhan Arunagirinathan, **Rabindranath Garai**, Ritesh Kant Gupta, Parameswar Krishnan Iyer, "Enhancing Efficiency and Ambient Stability of Perovskite Solar Cells via Multifunctional Trap Passivation Molecule*". J. Mater. Chem. C*, 2021, **9**, 14309-14317.
16. Arvin Sain Tanwar, Retwik Parui, **Rabindranath Garai**, Moirangthem Anita Chanu, Parameswar Krishnan Iyer, "Dual "Static and Dynamic" Fluorescence Quenching Mechanisms Based Detection of TNT via a Cationic Conjugated Polymer." *ACS Meas. Sci. Au* 2022, **2**, 23–30.
17. Anwesha Choudhury, Ritesh Kant Gupta, **Rabindranath Garai**, Parameswar Krishnan Iyer, "Tailoring trap density of states through Impedance analysis for flexible organic field-effect transistors." *Adv. Mater. Interfaces*, 2021, **8**, 2100574.
18. Maimur Hossain, Mohammad Adil Afroz, **Rabindranath Garai**, "Tuning the open circuit voltage by incorporating a diflurophenyl unit into a polymer backbone to

achieve high efficiency polymer solar cells." *Sustainable Energy Fuels*, 2021, **5**, 874-879.

19. Mohammad Adil Afroz, Ritesh Kant Gupta, **Rabindranath Garai**, Maimur Hossain, Suyashpati Tripathi, Parameswar Krishnan Iyer, "Crystallization and grain growth regulation through Lewis acid-base adduct formation in hot cast perovskite-based solar cells." *Org. Electron.*, 2019, **74**, 172-178.
20. Anwesha Choudhury, Priyanka Dogra, Biki Teron, Ritesh Kant Gupta**,** Anamika Dey, Ashish Singh, **Rabindranath Garai**, Parameswar Krishnan Iyer, "Morphology Control of Mixed Halide Perovskite for its Application in Low-cost Thin Film Transistor." *2nd IEEE International Conference on Power Electronics, Intelligent Control and Energy Systems (ICPEICES)*, 2018**,** 743-747.

Book Chapter

1. Ritesh Kant Gupta, Rahul Narasimhan Arunagirinathan, Mohammad Adil Afroz, **Rabindranath Garai**, Anwesha Choudhury, Maimur Hossain, Ramesh Babu Yathirajula, Parameswar Krishnan Iyer, "Functional materials for various organic electronic devices", 2021, *Chemical Solution Synthesis for Materials Design and Thin Film Device Applications, Elsevier,* 119-165.

Patents Filed

1. Parameswar Krishnan Iyer, **Rabindranath Garai**, Mohammad Adil Afroz, Ritesh Kant Gupta, "PTB7-Th donor polymer-based Donor- acceptor (D-A) conducting polymer (CPs) suitable for polymer solar cells (PSC) and devices thereof", Ref. No. 201931020744, Appl. No. TEMP/E-1/21812/2019-KOL.
2. Parameswar Krishnan Iyer, Ritesh Kant Gupta, Mohammad Adil Afroz, **Rabindranath Garai**, "A High Efficiency Polymer Solar Cell and a Process for Fabricating the same", Ref. No. 201931019186, Appl. No. TEMP/E-1/20133/2019-KOL.

Conferences and Workshops

1. International Conference on **Progress and Challenges in Modern Day Science** (**PCMDS-2021**) organized by B. Barooah College, Guwahati, Assam, India during 17-18 June, 2021 (**Oral Presentation**)
2. **30th Annual Meeting of MRS-J** held online and organized by The Materials Research Society of Japan during December 9-11, 2020. **(Oral Presentation)**
3. Participated in "**Department Lecture Series**" titled “Optoelectronic Properties of perovskite Semiconductor Nanocrystals” organised by Department of Chemistry, SRM University - AP, Andhra Pradesh held on 7th July 2020
4. **12th Japan-Korea Joint Symposium on Bio-micro sensing Technology (12th JKBT)** held at KIT Japan, December, 2019. **(Oral Presentation).**
5. **2nd Asian Symposium on Cutting-edge Biotechnology (ASBC)** held at KIT Japan, December, 2019. **(Poster Presentation)**
6. **6th International Conference on Advanced Nanomaterials and Nanotechnology (ICANN2019)** held at Indian Institute of Technology Guwahati, Assam, India during December 18-21, 2019. **(Poster Presentation)**
7. Participated in **5th National Workshop on MEMS/NEMS and Theranostic Devices (NWNTD2019)** organized by Centre for Nanotechnology, IIT Guwahati, Assam during February 21-23, 2019.
8. **National Conference on Advances in Spectroscopic Techniques and Materials (ASTM-2018)** held at IIT(ISM) Dhanbad, Dhanbad, Jharkhand, 14-16, 2018. **(Oral Presentation)**
9. **Research Conclave’16** held at IIT Guwahati, Guwahati, Assam, March, 2018. **(Poster Presentation)**
10. Participated in **4th National Workshop on MEMS/NEMS and Theranostic Devices (NWNTD2018)** organized by Centre for Nanotechnology, IIT Guwahati, Assam during February 26-28, 2018.
11. **International Conference on Advanced Nanomaterials and Nanotechnology (ICANN2017)**, held at Indian Institute of Technology Guwahati, Assam during December 18-21, 2017. **(Poster Presentation)**
12. Participated in **3rd National Workshop on MEMS/NEMS and Theranostic Devices (NWNTD2017)** organized by Centre for Nanotechnology, IIT Guwahati, Assam during February 21-23, 2017.